Cell Journal (Yakhteh)

Guide for Authors

Aims and Scope: The "Cell Journal (Yakhteh)" is a peer review and monthly English publication of Royan Institute of Iran. The aim of the journal is to disseminate information through publishing the most recent scientific research studies on exclusively Cellular, Molecular and other related topics. **Cell J**, has been certified by the Ministry of Culture and Islamic Guidance since 1999 and also accredited as a scientific and research journal by HBI (Health and Biomedical Information) Journal Accreditation Commission since 2000 which is an open access journal. **This journal holds the membership of the Committee on Publication Ethics (COPE).**

1. Types of articles

The articles in the field of Cellular and Molecular can be considered for publications in **Cell J.** These articles are as below:

A. Original articles

Original articles are scientific reports of the original research studies. The article consists of English Abstract (structured), Introduction, Materials and Methods, Results, Discussion, Conclusion, Acknowledgements, Author's Contributions, and References **(Up to 40).**

B. Review articles

Review articles are the articles written by well experienced authors and those who have excellence in the related fields. The corresponding author of the review article must be one of the authors of at least three published articles appearing in the references. The review article consists of English Abstract (unstructured), Introduction, Conclusion, Author's Contributions, and References **(Up to 70).**

C. Systematic Reviews

Systematic reviews are a type of literature review that collect and critically analyzes multiple research studies or papers. The Systematic reviews consist of English Abstract (unstructured), Introduction, Materials and Methods, Results, Discussion, Conclusion, Acknowledgements, Author's Contributions, and References **(Up to 70).**

D. Short communications

Short communications are articles containing new findings. Submissions should be brief reports of ongoing researches. The short communication consists of English Abstract (unstructured), the body of the manuscript (should not hold heading or subheading), Acknowledgements, Author's Contributions, and References **(Up to 30).**

E. Case reports

Case reports are short discussions of a case or case series with unique features not previously described which make an important teaching point or scientific observation. They may describe novel techniques or use equipment, or new information on diseases of importance. It consists of English Abstracts (Unstructured), Introduction, Case Report, Discussion, Acknowledgements, Author's Contributions, and References **(Up to 30).**

F. Editorial

Editorials are articles should be written in relevant and new data of journals' filed by either the editor in chief or the editorial board.

G. Imaging in biology

Images in biology should focus on a single case with an interesting illustration such as a photograph, histological specimen or investigation. Color images are welcomed. The text should be brief and informative.

H. Letter to the editors

Letter to the editors are in response to previously published **Cell J** articles, and may also include interesting cases that do not meet the requirement of being truly exceptional, as well as other brief technical or clinical notes of general interest.

I. Debate

Debates are articles which show a discussion of the positive and negative view of the author concerning all aspect of the issue relevant to scientific research.

2. Submission process

It is recommended to see the guidelines for reporting different kinds of manuscripts. This guide explains how to prepare the

manuscript for submission. Before submitting, we suggest authors to familiarize themselves with **Cell J** format and content by reading the journal via the website (www.celljournal.org). The corresponding author ensures that all authors are included in the author list and agree with its order, and they must be aware of the manuscript submission.

A. Author contributions statements

It is essential for authors to include a statement of responsibility in the manuscript that specifies the contribution of every one of them. This participation must include conception and design of the manuscript, data acquisition or data analysis and interpretation, drafting of the manuscript and/or revising it for critically important intellectual content, revision and final approval of the manuscript and statistical analysis, obtaining funding, administrative, technical, or material support, or supervision. Authors who do not meet the above criteria should be acknowledged in the **Acknowledgments section.**

B. Cover letter and copyright

Each manuscript should be accompanied by a cover letter, signed by all authors specifying the following statement: "The manuscript has been seen and approved by all authors and is not under active consideration for publication. It has neither been accepted for publication nor published in another journal fully or partially (except in abstract form). **Also, no manuscript would be accepted in case it has been pre-printed or submitted to other websites.** I hereby assign the copyright of the enclosed manuscript to **Cell J.**" Corresponding author must confirm the proof of the manuscript before online publishing. Also, it is needed to suggest three peer reviewers in the field of their manuscript.

C. Manuscript preparation

Authors whose first language is not English encouraged to consult a native English speaker in order to confirm his manuscripts to American or British (not a mixture) English usage and grammar. It is necessary to mention that we will check the plagiarism of your manuscript by iThenticate Software. The manuscript should be prepared in accordance with the "International Committee of Medical Journal Editors (ICMJE)". Please send your manuscript in two formats word and PDF (including: title, name of all the authors with their degree, abstract, full text, references, tables and figures) and also send tables and figures separately in the site. The abstract and text pages should have consecutive line numbers in the left margin beginning with the title page and continuing through the last page of the written text. Each abbreviation must be defined in the abstract and text when they are mentioned for the first time. Avoid using abbreviation in the title. Please use the international and standard abbreviations and symbols

It should be added that an essential step toward the integration and linking of scientific information reported in published literature is using standardized nomenclature in all fields of science and medicine. Species names must be italicized (*e.g., Homo sapiens*) and also the full genus and species written out in full, both in the title of the manuscript and at the first mention of an organism in a paper.

It is necessary to mention that genes, mutations, genotypes, and alleles must be indicated in italics. Please use the recommended name by consulting the appropriate genetic nomenclature database, e.g., HUGO for human genes. In another words; if it is a human gene, you must write all the letters in capital and italic (*e.g., OCT4, c-MYC*). If not, only write the first letter in capital and italic (*e.g., Oct4, c-Myc*). **In addition, protein designations are the same as the gene symbol but are not italicized.**

Of note, Cell J will only consider publishing genetic association study papers that are novel and statistically robust. Authors are advised to adhere to the recommendations outlined in the STREGA statement (http://www.strega-statement.org). The following criteria must be met for all submissions:

1. Hardy-Weinberg Equilibrium (HWE) calculations must be carried out and reported along with the P-values if applicable [see Namipashaki et al. 2015 (Cell J, Vol 17, N 2, Pages: 187-192) for a discussion].

2. Linkage disequilibrium (LD) structure between SNPs (if multiple SNPs are reported) must be presented.

3. Appropriate multiple testing correction (if multiple independent SNPs are reported) must be included.

Submissions that fail to meet the above criteria will be rejected before being sent out for review.

Each of the following manuscript components should begin in the following sequence:

Authors' names and order of them must be carefully considered (full name(s), highest awarded academic degree(s), email(s), and institutional affiliation(s) of all the authors in English. Also, you must send mobile number and full postal address of the corresponding author).

Changes to Authorship such as addition, deletion or rearrangement of author names must be made only before the manuscript has been accepted in the case of approving by the journal editor. In this case, the corresponding author must explain the reason of changing and confirm them (which has been signed by all authors of the manuscript). If the manuscript has already been published in an online issue, an erratum is needed.

Title is providing the full title of the research (do not use abbreviations in title).

Running title is providing a maximum of 7 words (no more than 50 characters).

Abstract must include Objective, Materials and Methods, Results, and Conclusion (no more than 300 words).

Keywords, three to five, must be supplied by the authors at the foot of the abstract chosen from the Medical Subject Heading (MeSH). Therefore; they must be specific and relevant to the paper.

The following components should be identified after the abstract:

Introduction: The Introduction should provide a brief background to the subject of the paper, explain the importance of the study, and state a precise study question or purpose.

Materials and Methods: It includes the exact methods or observations of experiments. If an apparatus is used, its manufacturer's name and address should be stipulated in parenthesis. If the method is established, give reference but if the method is new, give enough information so that another author can perform it. If a drug is used, its generic name, dose, and route of administration must be given. Standard units of measurements and chemical symbols of elements do not need to be defined.

Statistical analysis: Type of study and statistical methods should be mentioned and specified by any general computer program used.

Ethical considerations*:* Please state that informed consent was obtained from all human adult participants and from the parents or legal guardians of minors and include the name of the appropriate institutional review board that approved the project. It is necessary to indicate in the text that the maintenance and care of experimental animals complies with National Institutes of Health guidelines for the humane use of laboratory animals, or those of your Institute or agency.

Clinical trial registration: All of the Clinical Trials performing in Iran must be registered in Iranian Registry of Clinical Trials (www.irct.ir). The clinical trials performed abroad, could be considered for publication if they register in a registration site approved by WHO or www.clinicaltrials.gov. If you are reporting phase II or phase III randomized controlled trials, you must refer to the CONSORT Statement for recommendations to facilitate the complete and transparent reporting of trial findings. Reports that do not conform to the CONSORT guidelines may need to be revised before peer-reviewing.

Results: They must be presented in the form of text, tables, and figures. Take care that the text does not repeat data that are presented in tables and/or figures. Only emphasize and summarize the essential features of the main results. Tables and figures must be numbered consecutively as appeared in the text and should be organized in separate pages at the end of the manuscript while their location should be mentioned in the main text.

Tables and figures: If the result of your manuscript is too short, it is better to use the text instead of tables & figures. Tables should have a short descriptive heading above them and also any footnotes. Figure's caption should contain a brief title for the whole figure and continue with a short explanation of each part and also the symbols used (no more than 100 words). All figures must be prepared based on cell journal's guideline in color (no more than 6 Figures and Tables) and also in TIF format with 300 DPI resolution.

Of Note: Please put the tables & figures of the result in the results section not any other section of the manuscript.

Supplementary materials would be published on the online version of the journal. This material is important to the understanding and interpretation of the report and should not repeat material within the print article. The amount of supplementary material should be limited. Supplementary material should be original and not previously published and will undergo editorial and peer review with the main manuscript. Also, they must be cited in the manuscript text in parentheses, in a similar way as when citing a figure or a table. Provide a caption for each supplementary material submitted.

Discussion: It should emphasize the present findings and the variations or similarities with other researches done by other researchers. The detailed results should not be repeated in the discussion again. It must emphasize the new and important aspects of the study.

Conclusion: It emphasizes the new and important aspects of the study. All conclusions are justified by the results of the study.

Acknowledgements: This part includes a statement thanking those who contributed substantially with work relevant to the study but does not have authorship criteria. It includes those who provided technical help, writing assistance and name of departments that provided only general support. You must mention financial support in the study. Otherwise; write this sentence "There is no financial support in this study".

Conflict of interest: Any conflict of interest (financial or otherwise) and sources of financial support must be listed in the Acknowledgements. It includes providers of supplies and services from a commercial organization. Any commercial affiliation must be disclosed, regardless of providing the funding or not.

Of Note: If you have already any patent related to the subject of your manuscript, or you are going to apply for such a patent, it must be mentioned in this part.

References: The references must be written based on the Vancouver style. Thus the references are cited numerically in the text and listed in the bibliography by the order of their appearance. The titles of journals must be abbreviated according to the style used in the list of Journals Indexed in PubMed. Write surname and initials of all authors when there are six or less. In the case of seven or more authors, the names of the first six authors followed by "et al." must be listed. You can download Endnote file for Journal references style: endnote file

The reference of information must be based on the following order:

Article:

Surname(s) and first letter of name &middle name(s) of author(s) .Manuscript title. Journal title (abbr).publication date (year); Volume & Issue: Page number.

Example: Manicardi GC, Bianchi PG, Pantano S, Azzoni P, Bizzaro D, Bianchi U, et al. Presence of endogenous nicks in DNA of ejaculated human spermatozoa and its relationship to chromomycin A3 accessibility. Biol Reprod. 1995; 52(4): 864-867.

Book:

Surname(s) and first letter of name & middle name(s) of author(s).Book title. Edition. Publication place: publisher name; publication date (year); Page number.

Example: Edelman CL, Mandle CL. Health promotion throughout the lifespan. 2nd ed. ST Louis: Mosby; 1998; 145-163.

Chapter of book:

Surname(s) and first letter of name & middle name(s) of author(s).Chapter title. In: Surname(s) and first letter of name & middle name(s) of editor(s), editors. Book title. Edition. Publication place: publisher name; publication date (year); Page number.

Example: Phillips SJ, Whisnant JP. Hypertension and stroke. In: Laragh JH, Brenner BM, editors. Hypertension: pathophysiology, diagnosis, and management. 2nd ed. New York: Raven Press; 1995; 465-478.

Abstract book:

Example: Amini rad O.The antioxidant effect of pomegranate juice on sperm parameters and fertility potential in mice. Cell J. 2008;10 Suppl 1:38.

Thesis:

Name of author. Thesis title. Degree. City name. University. Publication date (year).

Example: Eftekhari Yazdi P. Comparison of fragment removal and co-culture with Vero cell monolayers on development of human fragmented embryos. Presented for the Ph.D., Tehran. Tarbiyat Modarres University. 2004.

Internet references

Article:

Example: Jahanshahi A, Mirnajafi-Zadeh J, Javan M, Mohammad-Zadeh M, Rohani M. Effect of low-frequency stimulation on adenosineA1 and A2A receptors gene expression in dentate gyrus of perforant path kindled rats. Cell J. 2008; 10 (2): 87-92. Available from: http://www.celljournal.org. (20 Oct 2008).

Book:

Example: Anderson SC, Poulsen KB. Anderson's electronic atlas of hematology.[CD-ROM]. Philadelphia: Lippincott Williams & Wilkins; 2002.

D. Proofs are sent by email as PDF files and should be checked and returned within 72 hours of receipt. It is the authors' responsibility to check that all the text and data as contained in the page proofs are correct and suitable for publication. **We are requested to pay particular attention to author's names and affiliations as it is essential that these details be accurate when the article is published.**

E. Pay for publication: Publishing an article in **Cell J** requires Article Processing Charges (APC) that will be billed to the submitting author following the acceptance of an article for publication. For more information please see www.celljournal.org.

F. Ethics of scientific publication: Manuscripts that have been published elsewhere with the same intellectual material will refer to duplicate publication. If authors have used their own previously published work or work that is currently under review, as the basis for a submitted manuscript, they are required to cite the previous work and indicate how their submitted manuscript offers novel contributions beyond those of the previous work. Research and publication misconduct is considered a serious breach of ethics.

The Journal systematically employs iThenticate, plagiarism detection and prevention software designed to ensure the originality of written work before publication. Plagiarism of text from a previously published manuscript by the same or another author is a serious publication offence. Some parts of text may be used, only where the source of the quoted material is clearly acknowledged.

3. General information

A. You can send your manuscript via online submission system which is available on our website. If the manuscript is not prepared according to the format of **Cell J**, it will be returned to authors.

B. The order of article appearance in the Journal is not demonstrating the scientific characters of the authors.

C. Cell J has authority to accept or reject the manuscript.

D. The received manuscript will be evaluated by associate editor. **Cell J** uses a single-blind peer review system and if the manuscript suits the journal criteria, we select the reviewers. If three reviewers pass their judgments on the manuscript, it will be presented to the editorial board of **Cell J.** If the editorial board has a positive judgment about the manuscript, reviewers' comments will be presented to the corresponding author (the identification of the reviewers will not be revealed). The executive member of journal will contact the corresponding author directly within 3-4 weeks by email. If authors do not receive any reply from journal office after the specified time, they can contact journal office. Finally, executive manager will respond promptly to authors' request.

The Final Checklist

The authors must ensure that before submitting the manuscript for publication, they have to consider the following parts:

1. The first page of manuscript should contain title, name of the author/coauthors, their academic qualifications, designation & institutions they are affiliated with, mailing address for future correspondence, email address, phone, and fax number.

2. Text of manuscript and References prepared as stated in the "guide for authors" section.

3. Tables should be on a separate page. Figures must be sent in color and also in JPEG (Jpg) format.

4. Cover Letter should be uploaded with the signature of all authors.

5. An ethical committee letter should be inserted at the end of the cover letter.

The Editor-in-Chief: Ahmad Hosseini, Ph.D.

Cell Journal *(Yakhteh)*

P.O. Box: 16635-148, Iran

Tel/Fax: + 98-21-22510895

Emails: Celljournal@royaninstitute.org

info@celljournal.org

IN THE NAME OF GOD

Dr. Saeed Kazemi Ashtiani

Gone But not Forgotten

In the memory of the late Director of Royan Institute, Founder of Stem Cells Research in Iran and Chairman of ***Cell Journal*** *(Yakhteh)*. May he rest in peace.

PUBLISHED & SPONSORED BY:
Publication of Royan Institute (ACECR)

Indexed in:
1. Thomson Reuters (ISI)
2. PubMed
3. PubMed Central (PMC)
4. National Library Medicine (NLM)
5. Biosis Preview
6. Index Medicus for the Eastern Mediterranean Region (IMEMR)
7. Regional Information Center for Sciences and Technology (RICeST)
8. Index Copernicus International
9. Cambridge Scientific Abstract (CSA)
10. EMBASE
11. Scopus
12. Cinahl Database
13. Google Scholar
14. Chemical Abstract Service (CAS)
15. Proquest
16. Directory of Open Access Journals (DOAJ)
17. Open Academic Journals Index (OAJI)
18. Directory of Research Journals Indexing (DRJI)
19. Scientific Information Database (SID)
20. Iranmedex
21. Islamic World Science Citation Center (ISC)
22. Magiran
23. Science Library Index
24. Biological Abstracts
25. Essential Science Indicators
26. EuroPub

Editorial Office Address (Dr. Ahmad Hosseini):
Royan Institute, P.O.Box: 16635-148,
Tehran, Iran
Tel & Fax: (+9821)22510895
Website: www.celljournal.org
Emails: info@celljournal.org
celljournal@royaninstitute.org

Printing Company:
Naghshe e Johar Co.
No. 103, Fajr alley, Tehranpars Street,
Tehran, Iran.

CELL JOURNAL

(Yakhteh)

Vol 24, No 9, September 2022, Serial Number: 104

Pages: 491-554

ISSN: 2228-5806

eISSN: 2228-5814

www.celljournal.org

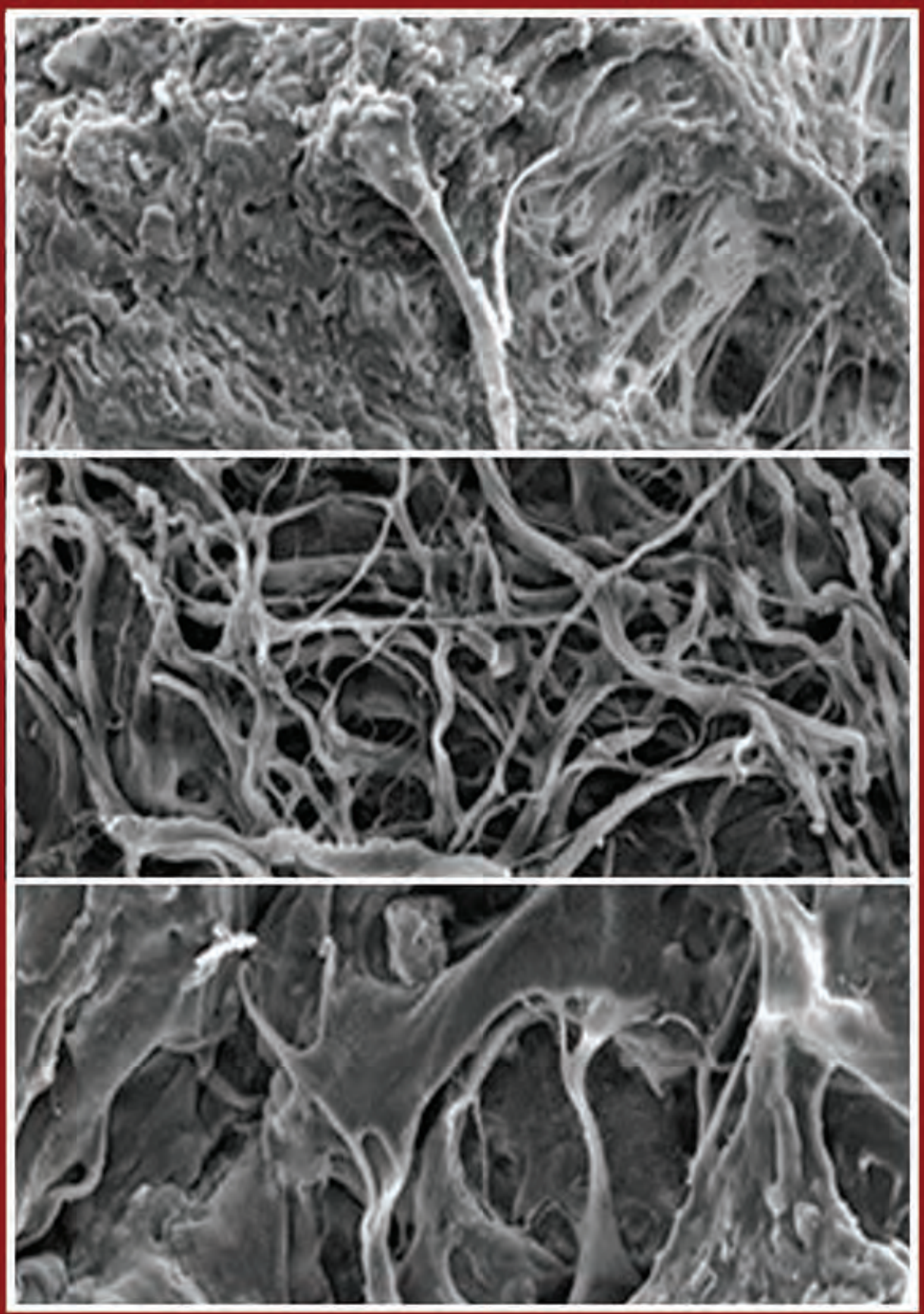

A monthly publication of the Royan Institute

پژوهشگاه رویان

Cell Journal(Yakhteh), Vol 24, No 9, September 2022, Serial Number: 104, Pages: 491-554

CONTENTS

Original Articles

Short Communications

Original Article

Comparative Study of The Effects of Confounding Factors on Improving Rat Pancreatic Islet Isolation Yield and Quality

Maedeh Moazenchi, M.Sc.[1, 2#], Anavasadat Sadr Hashemi Nejad, M.Sc.[1, 2#], Mahmoud Izadi, M.Sc.[1, 2#], Maedeh Khalaj, M.Sc.[1], Zakieh Samsonchi, M.Sc.[1], Pouya Tavakol Rad, H.S.D.[1], Payam Amini, Ph.D.[3], Yaser Tahamtani, Ph.D.[1, 3], Ensiyeh Hajizadeh-Saffar, M.D., Ph.D.[2, 3, 4*]

1. Department of Stem Cells and Developmental Biology, Cell Science Research Center, Royan Institute for Stem Cell Biology and Technology, ACECR, Tehran, Iran
2. Advanced Therapy Medicinal Product Technology Development Center (ATMP-TDC), Cell Science Research Center, Royan Institute for Stem Cell Biology and Technology, ACECR, Tehran, Iran
3. Reproductive Epidemiology Research Center, Royan Institute for Reproductive Biomedicine, ACECR, Tehran, Iran
4. Department of Regenerative Medicine, Cell Science Research Center, Royan Institute for Stem Cell Biology and Technology, ACECR, Tehran, Iran

Corresponding Address: P.O.Box: 16635-148, Department of Regenerative Medicine, Cell Science Research Center, Royan Institute for Stem Cell Biology and Technology, ACECR, Tehran, Iran
Email: en.hajizadeh@royan-rc.ac.ir

#These authors contributed equally to this work.

Received: 30/June/2021, Accepted: 04/December/2021

Abstract

Objective: Isolated pancreatic islets are valuable resources for a wide range of research, including cell replacement studies and cell-based platforms for diabetes drug discovery and disease modeling. Islet isolation is a complex and stepwise procedure aiming to obtain pure, viable, and functional islets for *in vitro* and *in vivo* studies. It should be noted that differences in rodent strains, gender, weight, and density gradients may affect the isolated islet's properties. We evaluated the variables affecting the rat islet isolation procedure to reach the maximum islet yield and functionality, which would be critical for further studies on islet regenerative biology.

Materials and Methods: The present experimental study compared the yield and purity of isolated islets from non-diabetic rats of two different strains. Next, islet particle number (IPN) and islet equivalent (IEQ) were compared between males and females, and the weight range that yields the highest number of islets was investigated. Moreover, the influence of three different density gradients, namely Histopaque, Pancoll, and Lymphodex, on final isolated islets purity and yield were assessed. Finally, the viability and functionality of isolated islets were measured.

Results: The IEQ, IPN, and purity of isolated islets in 15 Lister hooded rats (LHRs) were significantly (P≤0.05) higher than those of the other strains. Male LHRs resulted in significantly higher IEQ compared to females (P≤0.05). Moreover, IPN and IEQ did not significantly vary among different weight groups. Also, the utilization of Histopaque and Pancoll leads to higher yield and purity. *In vivo* assessments of the isolated islets presented significantly reduced blood glucose percentage in the transplanted group on days 2-5 following transplantation.

Conclusion: Based on these results, an optimal protocol for isolating high-quality rat islets with a constant yield, purity, and function has been established as an essential platform for developing diabetes research.

Keywords: Insulin Secreting Cells, *In Vitro* Techniques, Pancreatic Islets, Rodent, Type-1 Diabetes

Cell Journal(Yakhteh), Vol 24, No 9, September 2022, Pages: 491-499

Citation: Moazenchi M, Sadr Hashemi Nejad A, Izadi M, Khalaj M, Samsonchi Z, Tavakol Rad P, Amini P, Tahamtani Y, Hajizadeh-Saffar E. Comparative study of the effects of confounding factors on improving rat pancreatic islet isolation yield and quality. Cell J. 2022; 24(9): 491-499. doi: 10.22074/cellj.2022.8123.

Introduction

According to the International Diabetes Federation Diabetes Atlas, the number of worldwide diabetic patients has been estimated to be 536.6 as of 2021, and it has been projected to be increased to 783.2 million by 2045, making this condition a significant threat to human health (1).

Insulin therapy is recommended for patients with type-1 diabetes and even some with type-2 diabetes, although it is not considered a cure. Insulin injections can cause weight gain, edema, refractive changes, fat atrophy, and other long-term side effects (2). Also, it may cause diabetes-induced life-threatening complications such as severe hypoglycemic events following exogenous insulin administration (2, 3). Recently various studies showed that pancreas and islet transplantation (including live cell transplantation) are potentially ideal therapies for patients diagnosed with type-1 diabetes. Pancreas transplantation is relatively a mature treatment method; however, main issues such as major surgery complications and lifelong usage of immune-suppressive drugs remain to be addressed. Nevertheless, islet transplantation through minor surgery, limited immune suppressive regimens, and the possibility of using immunoisolation strategies have fewer complications (2, 4-7). Due to the minor

side effects associated with islet transplantation, it is considered a promising therapy for type-I diabetes (8).

Therefore, researchers worldwide have focused on pancreatic islet and beta-cell transplantation since late 1900. Also, many studies were conducted on islets of Langerhans as a key platform for developing various diabetes research (2, 9, 10). Although animal model-based studies are not entirely predictive of human responses, isolated islets from animal models provide more opportunities to study the mechanisms of diabetes, potential drug discovery, and genetic-based research (9, 10). Based on the previous reports, the quantity and quality of isolated islets play an essential role in successful islet transplantation in experimental studies (2). In an effort to develop a standard and effective method, researchers have modified and improved the initial isolation and purification methods, such as the Edmonton protocol (8, 11).

Although animal studies are not considered a replacement for human trials, they can mimic human diseases and provide a neat way to study similar pathways in human and animal models (12). Also, preclinical studies are important in the safety assessment of different therapeutic products and methods. From understanding the function of the pancreas and the discovery of insulin to new concepts such as stem cell therapy, islet isolation, and transplantation, animal studies have played a significant role in diabetes research. The primary function of islets is insulin production, which is pretty similar between humans and animals, and the restoration of normoglycemia can be achieved by transplantation of mouse/rat islets in diabetic mice/rats (13).

Rodents have many advantages, including high reproductive capacity, pure strains, accessibility, repeatability, short experiment times, and low cost, enabling them to be widely used in various research projects (8). Thus, we have established Royan Institute Rodent Pancreatic Islet Processing Facility (RI-RPIPF) to promote research projects toward improving islet transplantation outcomes and facilitate studies focused on different aspects of islet nature and transplant. This study described our improved rat pancreatic islet isolation method in RI-RPIPF. Moreover, two rat strains, Lister hooded rats (LHR) and Wistar albino rats (WAR), were compared in terms of islet equivalent (IEQ) and islet particle number (IPN). Then, the best strain was used to compare gender, weights, and different density gradients. The optimal procedure for rat pancreatic islet isolation was set up in view of islets yield, purity, and functionality.

Materials and Methods

The materials and methods used in this experimental study are as follows:

Animals

Following the Royan Institute Ethics Committee approval (IR.ACECR.ROYAN.REC.1396.29 and IR.ACECR.ROYAN.REC.1397.227), LHRs and WARs, weighing 250-450 g, were bought from Animal Core Facility, Reproductive Biomedicine Research Center, Royan Institute for Biotechnology. Rats were housed in cages in a room with controlled temperature (24°C), humidity, and 12 hours/12 hours light and dark cycle. Also they were given ad libitum access to food and water. All protocols conformed with Guide Laboratory Animals for The Care and Use (eighth edition). The total number of rats used in this study was 95 LHRs and 15 WARs. Strains were selected based on the previous rat islet isolation studies and in-house protocols. The number of rats used in each experiment is mentioned; however, it should be noted that the sum of rats in different sections is more than the number provided above since islets isolated from some rats were used for more than one experiment.

Rat islet isolation procedure

Pancreas isolation

The pancreas isolation method used in this study is based on in-house protocols and what was previously described (14). In brief, the digestion solution was prepared using Hanks' Balanced Salt Solution (HBSS) 1x without calcium and magnesium (Gibco-14170) with 1 mg/ml collagenase type V (Sigma-Aldrich, Germany, C9263, ≥1 FALGPA units/mg solid, >125 CDU/mg solid). Then, 20 mg of collagenase was completely dissolved in 20 ml HBSS to isolate islets per rat pancreas; next, the enzyme solution w filtered through a 0.22 μm filter (TPP, Switzerland, 99722). The collagenase solution should be prepared freshly and placed on ice to achieve optimal enzyme activity.

Healthy, non-diabetic rats were anesthetized and sacrificed in a CO_2 chamber. Following abdominal skin sterilization, the abdomen was cut with a V-incision. The duodenal papilla was horizontally clamped with a surgical hemostat to block the bile pathway toward the intestine. The 10 mL cold collagenase solution was injected into the Common Bile Duct (CBD). The whole pancreas was bulged from head to tail due to digestion solution flow in all regions. The pancreas was rapidly removed, and fat and connective tissues were trimmed and subsequently transferred into a 50 ml conical tube containing a 5 ml cold collagenase solution.

Pancreas digestion

Pancreas digestion is also performed using in-house protocols and methods described previously (14). In brief, the conical tube was placed in a 37°C water bath for 5 minutes, and the mixture of pancreas and collagenase was transferred to a culture dish to cut the tissue into small pieces. An extra 5 ml pre-warmed (at room temperature) collagenase solution was added to the culture dish, and the mixture returned into a conical tube placed in a 37°C water bath. After 15

minutes, samples were taken each 2 minutes, and the number of free islets that appeared spherical, and golden-brown from acinar tissue was estimated. When over 50% of islets became free of exocrine cells, the suspension volume was immediately doubled using the stop buffer to terminate the digestion process. Stop buffer and culture media containing Roswell Park Memorial Institute (RPMI) 1640 (Corning, USA, 17-105-CV) with 10% fetal bovine serum (FBS, Gibco, Brazil, 10270), 1% L-glutamine (L-GLU, Gibco, Scotland, 25030024), and 1% Penicillin-Streptomycin (Pen-Strep, Sigma-Aldrich, Germany, P4333). The suspension was centrifuged at 900 RPM for 2 minutes at 4°C, and the supernatant was decanted into a waste container. The pellet was washed with 10 ml washing buffer containing RPMI 1640 with 5% FBS and 1% L-GLU and 1% Pen-Strep and centrifuged at 900 RPM for 2 minutes at 4°C (repeated two times).

Islet purification

In this study, three different density gradients, including Histopaque, Pancoll, and Lymphodex, were used for purification to determine the most efficient density gradient to be used in the rat islet isolation process, without islet hand-picking or filtration.

The pellet was purified by discontinuous density gradient centrifugation immediately after discarding the supernatant. First, the pellet was suspended in 10 ml density gradients Histopaque-1077 (Sigma-Aldrich, Germany, 10771) or Pancoll 1.077(PAN-Biotech, Germany, P04-601000) or Lymphodex 1.070 (Inno-train, Germany, 002041600), and subsequently, 10 ml washing buffer was slowly added. The two-layer suspension was centrifuged at 2000 RPM for 18 minutes at 4°C. Islet cells were retrieved from the interphase between density gradient and washing solution.

Purified islets were washed with a washing buffer and centrifuged at 1000 RPM for 2 minutes at 4°C (repeated two times). The supernatant was discarded and replaced with 10 mL of culture media.

Islet culture

The suspension was transferred to a sterile petri dish in a laminar airflow cabinet using a stereomicroscope; then, the dish containing islets was placed at 37°C in a 5% CO_2 incubator. Figure 1 (created by Adobe InDesign version 6) demonstrates a brief schematic presentation of the stepwise rat pancreatic islet isolation procedure.

Islet quality control tests

Light microscopy and islet purity evaluations

Following the isolation procedure, pancreatic islets were observed and assessed using light microscopy regarding morphology, integrity, and capsule intactness. The purity of isolated islets was reported as the percentage of free islets obtained from the acinar tissues, estimated by two independent investigators after observation under a light microscope.

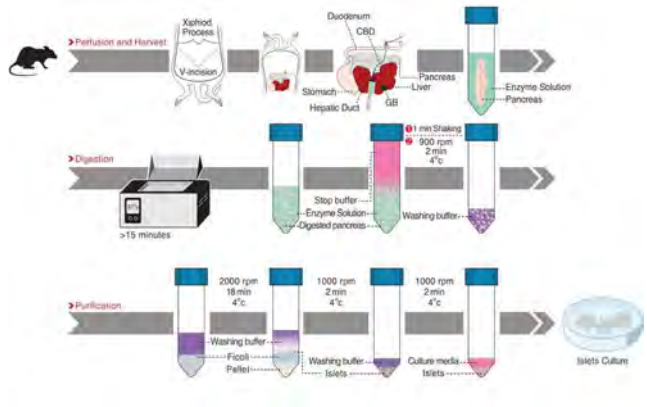

Fig.1: A schematic representation of rat pancreatic islet isolation procedure. The rat pancreatic islet isolation procedure consists of three major steps. First, using surgical techniques, the common bile duct is approached, and the collagenase solution is injected to bulge the pancreas. The pancreas is then extracted from the rat body and transferred to a conical tube with the rest of the enzyme solution. The digestion step starts when the enzyme solution reaches 37°C to remove islets from the exocrine tissue and stops by adding a stop buffer and washing steps to prevent over digestion of islets which could degrade islet capsules. Finally, islets are purified using density gradients and several washing steps to separate islets from non-islet tissue and cultured to maintain cell viability.

Islet yield

Islet yield is defined as the number of islets isolated from one pancreas (14). During the process, islets are isolated with other cells, such as acinar cells, making it hard to detect them under the microscope. So, there should be a specific stain to ease the detection of islets among other cells. Dithizone (1,5-diphenylthiocarbazone, DTZ, Sigma-Aldrich, Germany, D5130) binds with zinc in insulin granules in beta cells of pancreatic islets, causing the islets to stain with a red color while the rest of the cells remain unstained. To identify the islets and determine their quantity and purity, DTZ staining was performed as previously described (15). In brief, 1 mg DTZ was dissolved in 200 µL dimethyl sulfoxide (DMSO, Sigma-Aldrich, Germany, D2650) and then diluted in 800 µL Dulbecco's Phosphate-Buffered Saline (DPBS, Gibco, USA, LS14190250), and filtered through a 0.45 µm nylon filter (TPP, Switzerland, 99745). In a 6 cm Petri plate, 30 µL of DTZ solution was added to islet samples (100 µL), incubated at room temperature for 1-2 minutes, filled up with DPBS to half of the plate height, and visualized under the microscope, using a 10X eyepiece and a 4X objective to magnify 40X. The number of islets in the sample was counted, and the total IPN was estimated after calculation of dilution factor using the following equation according to Table 1.

Dilution Factor = Total volume of preparation that sample taken from (mL)×1000/Volume of sample taken (µL)

Based on the number of isolated islets in each diameter range (IPN, second column in Table 1), the IEQ (last

column in Table 1) was calculated, following mathematical correction for islet diameter (IEQ conversion factor), as shown in Table 1.

Table 1: Equations for total IPN and total IEQ

Islet diameter range (µm)	IPN	IEQ conversion factor	IEQ per range
50-100		×0.167	
101-150		×0.648	
151-200		×1.685	
201-250		×3.500	
251-300		×6.315	
301-350		×10.352	
>350		×15.833	
Σ IPN		Σ IEQ	
Dilution factor [(mL total volume/µL sample volume)×1000]			
Total IPN=Σ IPN×dilution factor			
Total IEQ = Σ IEQ×dilution factor			

IPN; Islet particle number and IEQ; Islet equivalent.

Islet viability and functionality

Fluorescein diacetate/Propidium iodide staining

In the fluorescence staining method for assessment of islet viability, fluorescein diacetate (FDA) and propidium iodide (PI) are used simultaneously to determine cell viability by distinguishing viable and nonviable cells, as previously described (16). In brief, 1.99 mg FDA (Sigma-Aldrich, USA, F7378) was dissolved in 200 mL acetone (Merck, Germany, 100014) in a glass bottle, fully covered by an aluminum foil, and subsequently aliquoted in 10 mL tubes and stored at -20°C. Also, 12.5 mg of PI (Sigma-Aldrich, USA, P4170) was dissolved in 25 mL of DPBS (Gibco, USA, LS14190250), covered by an aluminum foil, and subsequently aliquoted in 5 mL tubes and stored at 2-8°C. Four hundred sixty µL DPBS was added to a new culture dish to adjust the final concentrations of FDA, and PI to 0.46 and 14.34 µM, respectively. Islet suspension was mixed well, and a 100 µL sample was taken and transferred into an empty tube. From the bottom of the tube, 43 µL of settled islets were transferred to 460 µL of DPBS in the culture dish. The islet suspension was then treated with 10 µL of PI followed by 10 µL of FDA. The suspension was assessed by fluorescent microscopy, in which viable cells were considered as those with bright green fluorescence produced by FDA and dead cells as those with red fluorescence emitted by PI. The percentage of viable cells versus total cells was estimated after complete assessment.

Glucose-stimulated insulin secretion test

Glucose-stimulated insulin secretion (GSIS) test is a functional assay that measures the potency of insulin secretion from the islets when different glucose concentrations are applied, as described previously (17). Briefly, after 24-48 hours of islet culture at 37°C, three replicates of 100 IEQ/100 µL culture media were taken from islet suspension. Rat islets were incubated with a low glucose media (2.8 mM), and supernatant samples were taken at time zero and after one hour of incubation at 37°C. Then, another incubation was conducted with the same islets in higher glucose concentrations (28 mM), and supernatant samples were taken at time zero and one hour after the incubation at 37°C. Using a Rat/Mouse Insulin ELISA kit (Millipore, USA, EZRMI-13K), the amount of insulin released was measured in both supernatant samples. The stimulation index (SI) was calculated using the following formula, where insulin concentration from higher glucose concentration is in the numerator, and measurement result from lower glucose concentration is in the denominator. This index measures the ability of purified pancreatic islets to produce insulin in response to increased glucose concentrations.

Stimulation index (SI)=Insulin concentration after stimulation with 28 mM glucose concentration/Insulin concentration after stimulation with 2.8 mM glucose concentration

Islet transplantation*: in vivo* functional test

As we previously described, isolated islets were transplanted in the diabetic mice omentum to evaluate their functionality (18). In brief, male NMRI mice 8-10 weeks old were injected with 90 mg/kg alloxan (Sigma-Aldrich, USA, A7413) via the tail vein to induce diabetes. Two consecutive fasting blood glucose readings of more than 250 mg/dL confirmed diabetes induction. Mice were anesthetized using 90 mg/kg Ketamine 10% (Alfasan, Netherlands) and 4.5 mg/kg Xylazine 2% (Alfasan, Netherlands). Following a median abdominal incision, the greater omentum was spread out onto wet sterile gauze, and a minimum amount of islets (350 IEQ) was transplanted between two omentum layers. Next, the muscular layer was closed by a 5-0 Vicryl suture (VICRYL, Belgium, V2910H), and the skin was sutured with a 3-0 silk suture (MERSILK, W328). For six days following transplantation, non-fasting blood glucose levels were monitored in recipients to measure xenograft function.

Data analysis

SPSS version 20 was used for statistical analysis (SPSS Inc. Chicago, IL). The descriptive statistics of the continuous variables are shown as mean ± standard deviation. Kolmogorov-Smirnov test was utilized to assure the normality of data distribution. Student's t test and one-way analysis of variance (ANOVA) were used to assess the mean difference of continuous variables between two and more than two categories, respectively. Moreover, multiple comparisons were made by the least significant difference (LSD). A two-tailed P value less than 0.05 was determined statistically significant.

Results

Higher islet yield obtained from LHR strain, compared to WARs

Royan Institute Animal Core Facility provided thirty male LHR and WAR strains (15 each). As the first step of the primary endpoint, pancreatic islet yield was assessed in terms of IPN and IEQ and compared between the mentioned strains. As shown in Figure 2, IPN and IEQ for isolated islets from LHR were significantly (P≤0.05) higher than those of the other strains (Fig.2A, B, respectively). The percentage of islet purity, estimated by qualitative analysis, was significantly higher in LHR (61% vs. 75%, Fig.2C).

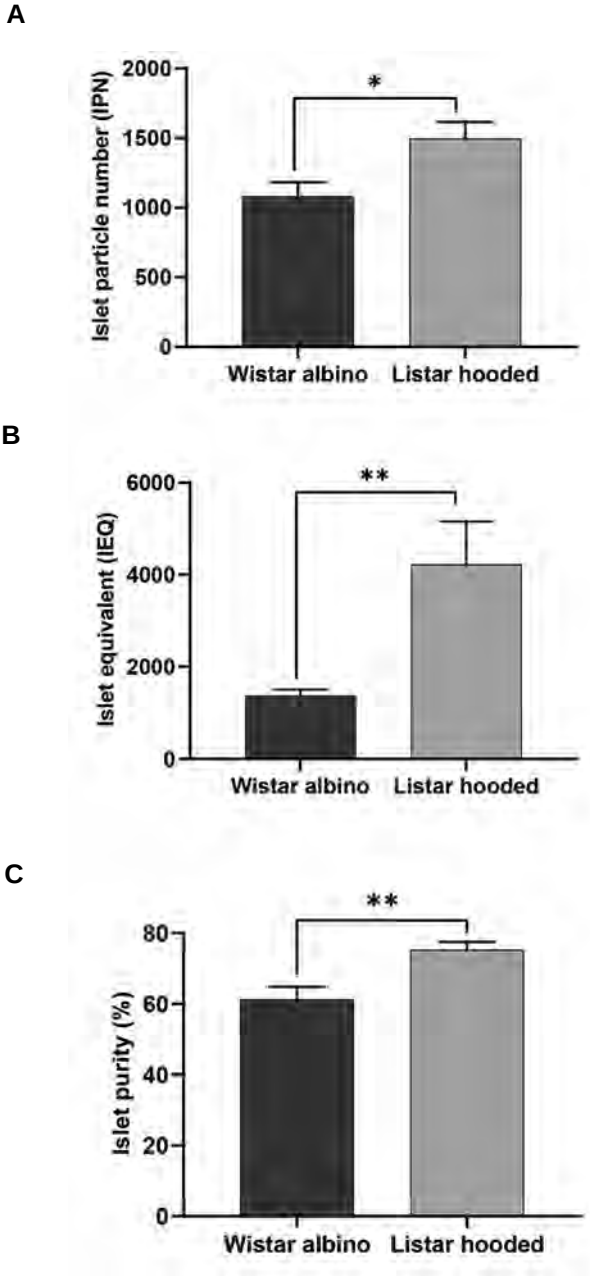

Fig.2: Comparison of IPN, IEQ values, and purity percentages between the two rat strains (n=15 each). **A.** The calculated IPN values were significantly higher in the LHR strain (P=0.013). **B.** The differences in resulted IEQ values in LHR strains were significant (P=0.005). **C.** The purity percentages were significantly higher in the LHR strain (P=0.002). LHR; Lister hooded rats, *; P≤0.05, and **; P≤0.01.

Male LHR yielded higher IEQ

According to the significantly higher yield and purity of LHRs, this strain was selected for further experiments in this study. In the next step, the effects of gender on IPN and IEQ were studied in LHRs (Fig.3A, B). Male and female rats were not significantly different regarding IPN (Fig.3A). However, islets isolated from male LHRs yielded significantly higher IEQ than females (P=0.009, Fig.3B).

No relationship between rat body weight and islet yield

Male LHRs were divided in four weight groups based on their body weights as follows: 250-300 g (n=22), 300-350 g (n=15), 350-400 g (n=13), and 400-450 g (n=9). Here, IPN or IEQ in different weight groups were studied. As shown in Figure 3C, D, there was no significant relationship between body weights and the resulted IPN or IEQ.

Histopaque and Pancoll resulted in high pure islets

Histopaque, Pancoll, and Lymphodex were used as density gradient reagents in the purification step. Comparing these gradient reagents showed no significant difference between Histopaque and Pancoll in IPN, IEQ, and purity. However, results obtained after applying Histopaque and Pancoll significantly differed from Lymphodex (P<0.05). The results demonstrated that the utilization of Lymphodex leads to lower IPN, IEQ, and purity (Figs.4, 5A-C, Table S1, See Supplementary Online Information at celljournal.org) (IPN; Lymphodex vs. two other gradients: both at P≤0.001, IEQ; Lymphodex vs. Histopaque (P=0.003) and Pancoll (P=0.013), Purity; Lymphodex vs. Histopaque (P≤0.001) and Pancoll (P≤0.001).

Isolated islets were viable and functional *in vitro*

The viability and functionality of isolated islets were assessed using FDA/PI staining and GSIS assay, respectively. Purified isolated islets were stained with DTZ (Fig.5D) to differentiate the islets from exocrine tissue and calculate IPN and IEQ. FDA/PI staining was done on purified islets to determine the live/dead ratio, visualized under the fluorescent microscope (Fig.5E). GSIS was performed after a 24 and 48-hour culture of isolated islets. SI was calculated using insulin secretion from islets in response to high versus low glucose concentrations, and results showed no significant differences between 24 and 48-hour islet cultures (Fig.5F).

Isolated islets were able to secrete insulin after transplantation

The *in vivo* function of implanted rat islets into the omentum of alloxan-induced diabetic mice was assessed by their potential to return normoglycemia. During six days post-transplantation, blood glucose level monitoring indicated a significant reduction in the percentages of blood glucose on days 2 (P=0.037), 3 (P=0.021), 4 (P=0.023), and 5 (P=0.044), in comparison with the non-transplanted diabetic mice used as a control group (Fig.5G).

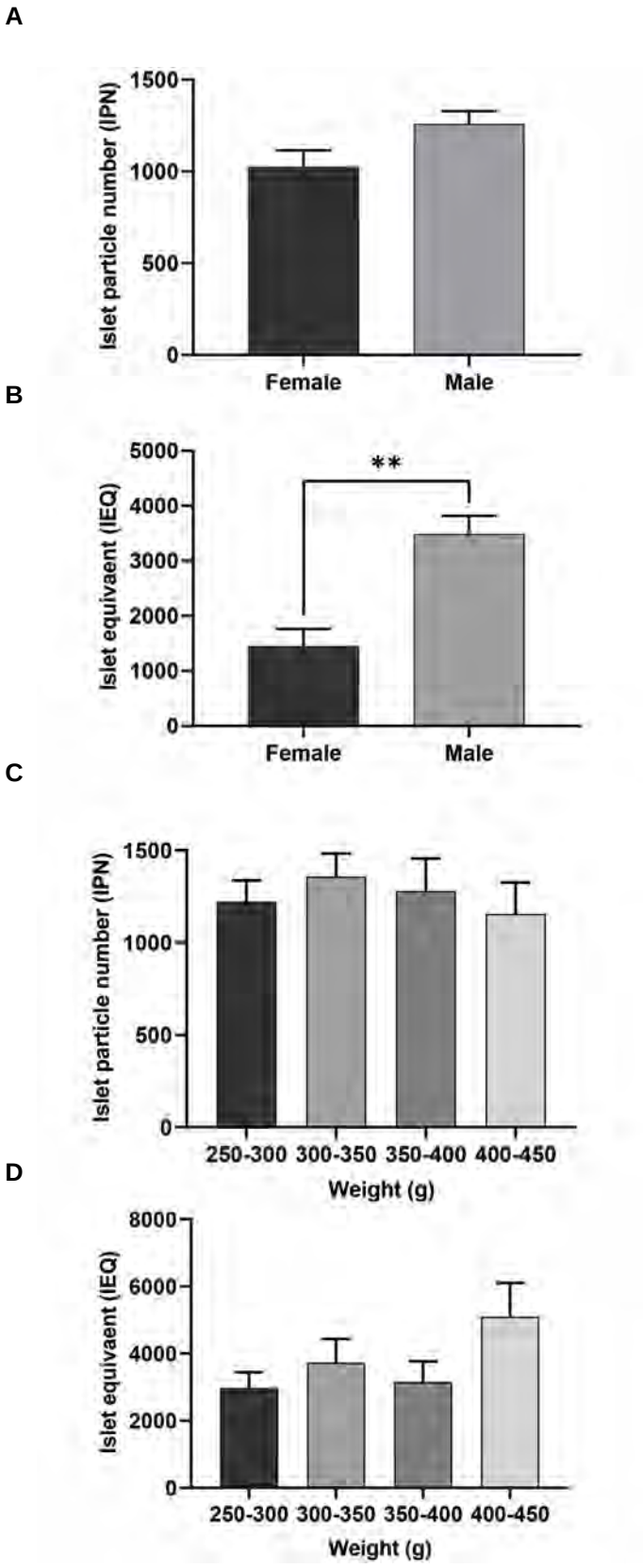

Fig.3: The effects of gender and weight on IPN and IEQ in Lister hooded strain. **A.** The IPN did not significantly vary between male (n=59) and female (n=12) LHRs (P=0.149). **B.** Male LHRs (n=59) had significantly higher IEQ compared to female ones (n=12) (P=0.009). **C.** The IPN did not significantly vary between four male LHR weight groups (P=0.816). **D.** No significant differences were observed among the four weight groups in terms of IEQ (P=0.177). LHR; Lister hooded rats and **; P≤0.01.

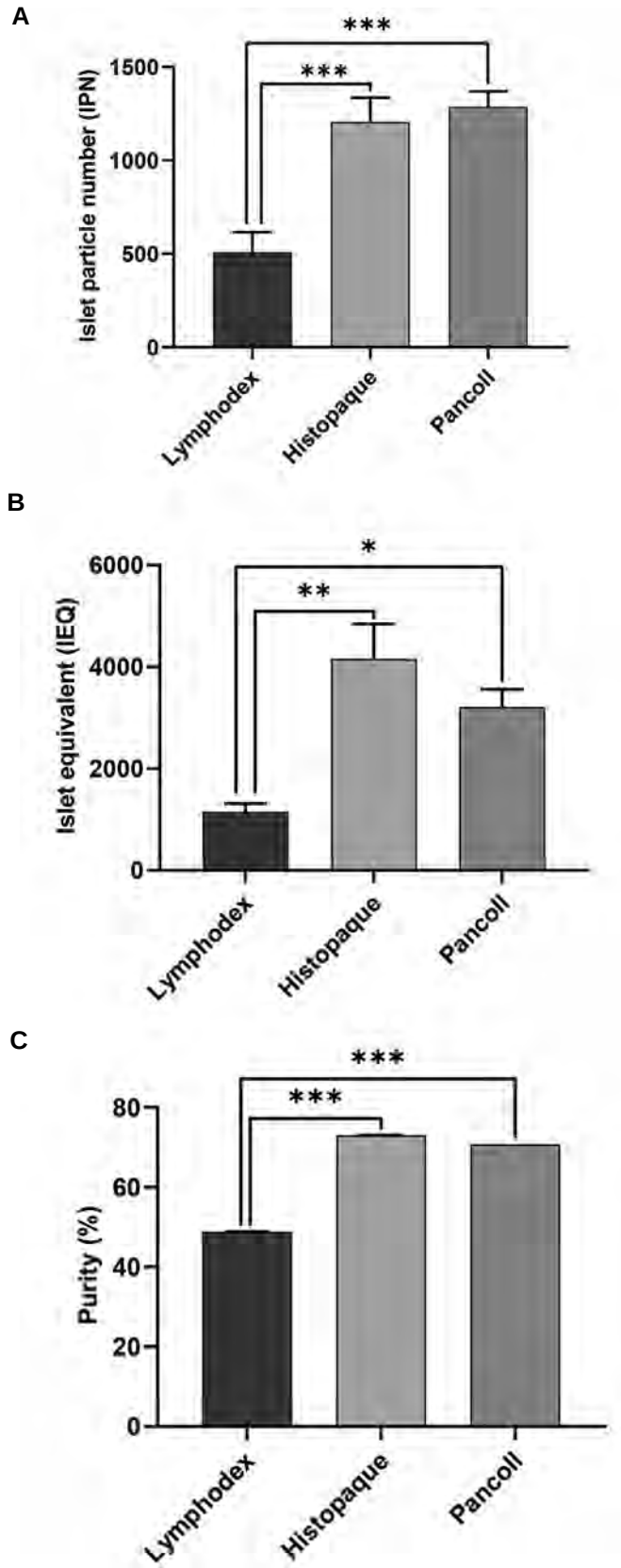

Fig.4: Comparison of different density gradients used in the purification step. **A.** Significant differences were found in IPN between Lymphodex (n=9) and two other gradients (both at P≤0.001). **B.** As compared to Histopaque (n=20) and Pancoll (n=39), the application of Lymphodex led to significantly lower IEQ (P=0.003 and P=0.013, respectively). **C.** Significantly higher purity was achieved when Histopaque (P≤0.001) and Pancoll (P≤0.001) were used as density gradients compared to Lymphodex. *; P≤0.05, **; P≤ 0.01, and ***; P≤0.001.

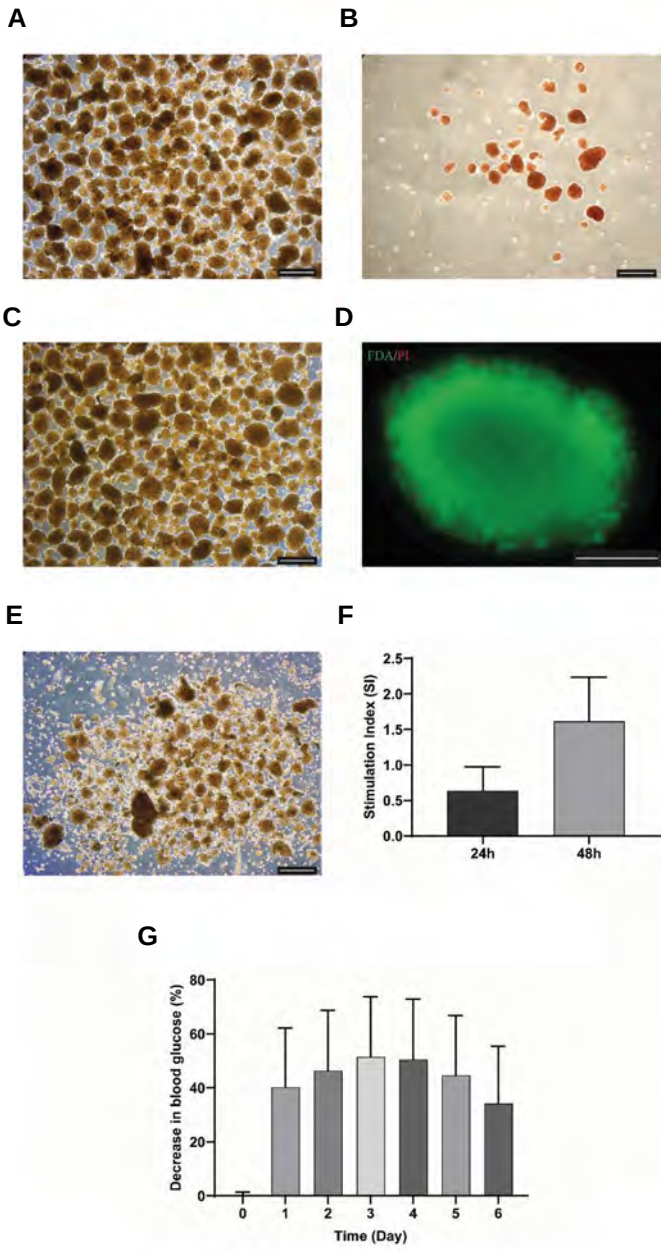

Fig.5: Purity, viability, and functionality assays on isolated islets from male Lister hooded rats. The purity of islets isolated using **A.** Histopaque, **B.** Pancoll, and **C.** Lymphodex (scale bar: 500 µm). **D.** Dithizone (DTZ) staining of isolated islets (scale bar: 500 µm). **E.** Viability estimation in isolated islets stained with Fluorescein diacetate (FDA)/propidium iodide (PI) using fluorescent microscopy (scale bar: 100 µm). **F.** Glucose-stimulated insulin secretion (GSIS). Stimulation index (SI) for 24 and 48-hour cultured isolated islets showed the functionality of isolated islets. SI resulting from a 48-hour culture presented considerable but not significant insulin secretion than 24-hour culture (P=0.074). **G.** Significant reduction in percentages of blood glucose on days 2 (P=0.037), 3 (P=0.021), 4 (P=0.023), and 5 (P=0.044) post islet transplantation (n=5) compared to the control group (n=4). h; hour.

Discussion

Having precise preclinical studies is necessary to start successful clinical trials and elucidate the new signaling pathways in basic research (19, 20). Islet transplantation is now regarded as a promising treatment option for type 1 diabetes; meanwhile, professional isolation of pancreatic islets plays a critical role in this treatment's efficiency (21). Different research groups worldwide have modified the islet isolation process to develop a functional and economical technique in recent decades. The islet isolation process includes digestion, purification, and islet culture steps that have been optimized to produce higher islet yield and purity in order to improve functional results. However, some challenges remain (5, 8, 20, 22, 23).

Nowadays, many researchers focus on improving these steps to achieve highly pure and functional islets. Overcoming isolation-associated obstacles lead to introducing islet transplantation as an efficient, widespread treatment (24). Yet, the shortage of pancreas donors and the high cost of human pancreatic islet isolation limited its availability for research purposes, resulting in a demand for the isolation of islets from animals, especially rodents, which is cost-effective, accessible, and easier (13).

In this study, we showed that variables such as rat strain and gender could affect islet yield and purity. Besides, the effects of rat body weight on IPN and IEQ were evaluated. Then, islet yield and purity were compared after administering different density gradients. Finally, *in vitro* and *in vivo* assays were performed to assess the viability and functionality of isolated islets. Here, we presented a straightforward and transparent protocol for efficient rat islet isolation.

Previous studies reported the dependence of islet isolation yield, purity, and functionality on factors such as strain and gender (11, 21, 25). de Groot et al. (21) showed that islet yield, purity, and function depend on donor rat strain. In comparison to Wistar albino (WA), Lewis, and Sprague Dawley (SD) rat strains, they obtained double amounts of islets from Albino Oxford (AO) rats. The islet purity was also shown to vary among the rat strains, so highly purified islets were isolated from all but SD rats. Moreover, de Haan et al. (26) compared islets isolated from AO, WA, and Lewis rats based on their quantity, size, and function and showed that the size and quantity of the isolated islet from AO rats were significantly larger than those from WA and Lewis. In contrast, Lewis rats had the highest glucose-induced insulin response. They suggested that isolated islets' yield and function were strain-dependent, and interestingly, GSIR does not necessarily increase with islet yield.

Our study compared islet isolation parameters between LHR and WAR strains. Islet yield parameters, IPN and IEQ, were significantly different between LHRs and WARs. Islet isolations using LHRs resulted in higher islet yield compared to WARs. Purity was qualitatively estimated and was significantly higher in LHRs. Although there were no significant differences in IPN between male and female rats, IEQ was significantly higher in islets obtained from male rats than in females. According to the strain and gender comparison, where IEQ showed a greater difference than IPN, the results indicated that volume per islet (IEQ/IPN) in LHRs is higher than in WARs. Also, in LHRs, islets isolated from male rats have higher volumes than female islets. Therefore, the difference in diameters and consequently in size of isolated islets led to statistically significant differences in IEQ. Considering

these findings, we used Lister male rats for the rest of this study.

In human islet isolation studies, body mass index (BMI) and weight of pancreas donors could reflect islet isolation outcomes which have been shown that higher donor weight and BMI led to higher isolated islet yield (5, 26-28). Tze and Tai (29) claimed that increased rat body weight could increase IPN. Therefore, in this study, we decided to examine possible correlations between rat body weight and isolated islets' IPN and IEQ. According to our results, the IPN for islets obtained from rats of 400-450 g was not significantly lower than IPN values measured for other weight ranges. Nonetheless, non-significant low IPN and non-significant high IEQ levels measured for 400-450 g rats compared to different weight ranges indicated that rats' body weight might slightly correlate with isolated islets' diameter and size. Altogether, it was concluded that rat bodyweights could not significantly affect islet yields. Likewise, Saliba and Fares (30) evaluated islet yields between mice of different ages (different ages correlates with different weight) and species and concluded that the yields were similar.

Another challenging factor in islet isolation protocols is the density gradient reagent's effect on islet yield and purity. There are different ways for islet separation and purification, including gradient separation, filtration, sedimentation, magnetic separation, and manually hand-picking (30, 31). Several studies focusing on islet isolation protocol development discussed the effects of different density gradients on outcome parameters. Several density gradients, including Ficoll, Histopaque, Dextran, and Iodixanol, have previously been studied for islet isolation that compared their recovery, viability, purity, *in vitro* functionality, IPN, and IEQ and showed that there were no differences in IPN and IEQ among groups. However, regarding purity and viability, Ficoll or Histopaque resulted in the purest and highest number of viable islets compared to Dextran and Iodixanol (11). Another study used Histopaque and Ficoll as gradient density solutions, resulting in no differences between those two, and concluded that both were acceptable and generally usable (14). Therefore, this study examined three density gradients, Histopaque, Pancoll, and Lymphodex, for their effects on islet yield parameters (IPN and IEQ) and purity. There were no significant differences in IPN, IEQ, and purity between Histopaque and Pancoll. Still, utilization of Lymphodex led to significantly lower islet purity and yield (lower IPN and IEQ values). The analysis showed that Lymphodex was not efficient for rat islet isolation, while Histopaque and Pancoll were sufficiently effective in the process. In addition, regarding cost-effectiveness, the prices of 10 ml of Histopaque or Pancoll required for each islet isolation procedure (~ 4.18 $ and 0.95 $, respectively) showed the usage of Pancoll is more cost-effective compared to Histopaque. Notably, in this study, isolated islets utilizing Histopaque and Pancoll were pure enough without the time-consuming procedure of hand-picking and filtration.

As previously reported, FDA/PI and GSIS assays were used after the islet isolation process to determine the viability and functionality of isolated islets, respectively (14). The viable and dead cells in the islets were indicated by green and red fluorescence caused by FDA and PI, respectively. Glucose-stimulated insulin secretion was used to assess isolated islets' functionality, evaluating the insulin-release ability of 24 and 48-hour cultured islets in response to glucose concentrations. While the data showed no significant differences between 24 and 48-hour SI, 48-hour cultured islets showed considerable insulin secretion.

Previously published studies presented transplanted human and mouse islets' functionality to reduce blood glucose levels in diabetic patients and diabetic mice, respectively (32-35). In this study, *in vivo* functional assessments showed a significantly higher reduction in non-fasting blood glucose percentages in transplanted mice than in non-transplanted diabetic one (control group) on days 2 to 5.

To prevent sacrificing more animals for this study, we used rat islets isolated for other diabetes research projects running simultaneously (18, 36, 37).

Conclusion

Given the importance of islet-based studies in developing novel diabetes therapies and drug discovery, a validated, replicable, and enhanced protocol for islet isolation with minimal variation is required. The optimized rat islet isolation protocol using male LHR and a Histopaque/Pancoll density gradient, yielded acceptable results, leading to a standard protocol for isolating high-quality rat islets with constant yield, purity, and functionality, which could meet global criteria to promote diabetes treatment research.

Acknowledgments

We are grateful to all Beta Cell Group members at Royan Institute for their thoughtful discussions and consultations during this project. This project was supported by the Department of Stem Cells and Developmental Biology, Cell Science Research Center, Royan Institute for Stem Cell Biology and Technology, and Lotus Charity Investment Foundation (Grant Numbers 95000148, 96000144). The authors declared no potential conflicts of interest concerning this article's research, authorship, and publication.

Authors' Contributions

M.M., A.S.H.N., M.I., E.H.-S.; Contributed to study design, conceptualization, methodology, formal analysis, investigation, and interpretation of the data. M.M., A.S.H.N.; Wrote the original manuscript. E.H.-S., Y.T.; Supervised the project, reviewed writing the draft, and provided financial support. M.Kh., Z.S., P.T.R.; Assisted

with methodology and investigation. P.A.; Contributed to statistical analysis and validation. All authors read and approved the final manuscript.

References

1. Sun H, Saeedi P, Karuranga S, Pinkepank M, Ogurtsova K, Duncan BB, et al. IDF diabetes atlas: global, regional and country-level diabetes prevalence estimates for 2021 and projections for 2045. Diabetes Res Clin Pract. 2022; 183: 109119.
2. Pang X, Xue W, Feng X, Tian X, Teng Y, Ding X, et al. Experimental studies on islets isolation, purification and function in rats. Int J Clin Exp Med. 2015; 8(11): 20932-20938.
3. Mazzi S, Ravasio R, Forlani G, Veronese G, Fabbri A, Marchesini G. Estimating the risk of severe hypoglycemic event related to glucose-lowering treatment among Italian patients with diabetes: the HYPOTHESIS database. Clinicoecon Outcomes Res. 2017; 9: 711-720.
4. Baharvand H, Jafary H, Massumi M, Ashtiani SK. Generation of insulin-secreting cells from human embryonic stem cells. Dev Growth Differ. 2006; 48(5): 323-332.
5. Khosravi-Maharlooei M, Hajizadeh-Saffar E, Tahamtani Y, Basiri M, Montazeri L, Khalooghi K, et al. Therapy of endocrine disease: islet transplantation for type 1 diabetes: so close and yet so far away. Eur J Endocrinol. 2015; 173(5): R165-R183.
6. Saberzadeh-Ardestani B, Karamzadeh R, Basiri M, Hajizadeh-Saffar E, Farhadi A, Shapiro AMJ, et al. Type 1 diabetes mellitus: cellular and molecular pathophysiology at a glance. Cell J. 2018; 20(3): 294-301.
7. Tavakoli A, Liong S. Pancreatic transplant in diabetes. Adv Exp Med Biol. 2012; 771: 420-437.
8. Zongyi Y, Funian Z, Hao L, Ying C, Jialin Z, Baifeng L. A rapid, efficient, and economic device and method for the isolation and purification of mouse islet cells. PLoS One. 2017; 12(2): e0171618.
9. Bevacqua RJ, Dai X, Lam JY, Gu X, Friedlander MSH, Tellez K, et al. CRISPR-based genome editing in primary human pancreatic islet cells. Nat Commun. 2021; 12(1): 2397.
10. Li Z, Sun H, Zhang J, Zhang H, Meng F, Cui Z. Development of in vitro 3D TissueFlex(R) islet model for diabetic drug efficacy testing. PLoS One. 2013; 8(8): e72612.
11. McCall MD, Maciver AH, Pawlick R, Edgar R, Shapiro AM. Histopaque provides optimal mouse islet purification kinetics: comparison study with Ficoll, iodixanol and dextran. Islets. 2011; 3(4): 144-149.
12. Barre-Sinoussi F, Montagutelli X. Animal models are essential to biological research: issues and perspectives. Future Sci OA. 2015; 1(4): FSO63.
13. Kottaisamy CPD, Raj DS, Prasanth Kumar V, Sankaran U. Experimental animal models for diabetes and its related complications-a review. Lab Anim Res. 2021; 37(1): 23.
14. Carter JD, Dula SB, Corbin KL, Wu R, Nunemaker CS. A practical guide to rodent islet isolation and assessment. Biol Proced Online. 2009; 11: 3-31.
15. NIH CIT Consortium Chemistry Manufacturing Controls Monitoring Committee; NIH CIT Consortium. Purified human pancreatic islet: qualitative and quantitative assessment of islets using dithizone (DTZ): standard operating procedure of the NIH clinical islet transplantation consortium. CellR4 Repair Replace Regen Reprogram. 2015; 3(1): e1369.
16. NIH CIT Consortium Chemistry Manufacturing Controls Monitoring Committee; NIH CIT Consortium. Purified human pancreatic islet - viability estimation of islet using fluorescent dyes (FDA/PI): standard operating procedure of the NIH clinical islet transplantation consortium. CellR4 Repair Replace Regen Reprogram. 2015; 3(1): e1378.
17. NIH CIT Consortium Chemistry Manufacturing Controls Monitoring Committee; NIH CIT Consortium. Functional assessment of purified human pancreatic islets: glucose stimulated insulin release by ELISA: a standard operating procedure of the NIH clinical islet transplantation consortium. CellR4 Repair Replace Regen Reprogram. 2014; 2(2): e900.
18. Izadi Z, Hajizadeh-Saffar E, Hadjati J, Habibi-Anbouhi M, Ghanian MH, Sadeghi-Abandansari H, et al. Tolerance induction by surface immobilization of Jagged-1 for immunoprotection of pancreatic islets. Biomaterials. 2018; 182: 191-201.
19. Cantarelli E, Citro A, Marzorati S, Melzi R, Scavini M, Piemonti L. Murine animal models for preclinical islet transplantation: No model fits all (research purposes). Islets. 2013; 5(2): 79-86.
20. Saliba Y, Bakhos JJ, Itani T, Fares N. An optimized protocol for purification of functional islets of Langerhans. Lab Invest. 2017; 97(1): 70-83.
21. de Groot M, de Haan BJ, Keizer PP, Schuurs TA, van Schilfgaarde R, Leuvenink HG. Rat islet isolation yield and function are donor strain dependent. Lab Anim. 2004; 38(2): 200-206.
22. Farney AC, Sutherland DE, Opara EC. Evolution of islet transplantation for the last 30 years. Pancreas. 2016; 45(1): 8-20.
23. Moskalewski S. Isolation and culture of the islets of langerhans of the guinea pig. Gen Comp Endocrinol. 1965; 5: 342-353.
24. Chhabra P, Sutherland D, Brayman KL. Overcoming barriers in clinical islet transplantation: current limitations and future prospects. Curr Probl Surg. 2014; 51(2): 49-86.
25. Strandell E, Sandler S. In vitro response to interleukin-1 beta and streptozotocin in pancreatic islets isolated from male and female nonobese diabetic mice. J Endocrinol. 1997; 153(1): 81-86.
26. de Haan BJ, Faas MM, Spijker H, van Willigen JW, de Haan A, de Vos P. Factors influencing isolation of functional pancreatic rat islets. Pancreas. 2004; 29(1): e15-22.
27. Al-Adra DP, Gill RS, Imes S, O'Gorman D, Kin T, Axford SJ, et al. Single-donor islet transplantation and long-term insulin independence in select patients with type 1 diabetes mellitus. Transplantation. 2014; 98(9): 1007-1012.
28. Matsumoto S, Noguchi H, Naziruddin B, Onaca N, Jackson A, Nobuyo H, et al. Improvement of pancreatic islet cell isolation for transplantation. Proc (Bayl Univ Med Cent). 2007; 20(4): 357-362.
29. Tze WJ, Tai J. Effect of body weight on islet isolation in rats. Transplantation. 1982; 34(1): 68.
30. Saliba Y, Fares N. Isolation, purification, and culture of mouse pancreatic islets of langerhans. Methods Mol Biol. 2019; 1940: 255-265.
31. O'Dowd JF, Stocker CJ. Isolation and purification of rodent pancreatic islets of langerhans. Methods Mol Biol. 2020; 2076: 179-184.
32. Loganathan G, Graham ML, Radosevich DM, Soltani SM, Tiwari M, Anazawa T, et al. Factors affecting transplant outcomes in diabetic nude mice receiving human, porcine, and nonhuman primate islets: analysis of 335 transplantations. Transplantation. 2013; 95(12): 1439-1447.
33. Ryan EA, Lakey JR, Rajotte RV, Korbutt GS, Kin T, Imes S, et al. Clinical outcomes and insulin secretion after islet transplantation with the Edmonton protocol. Diabetes. 2001; 50(4): 710-719.
34. Shapiro AM, Lakey JR, Ryan EA, Korbutt GS, Toth E, Warnock GL, et al. Islet transplantation in seven patients with type 1 diabetes mellitus using a glucocorticoid-free immunosuppressive regimen. N Engl J Med. 2000; 343(4): 230-238.
35. Song S, Yeung R, Park J, Posselt AM, Desai TA, Tang Q, et al. Glucose-stimulated insulin response of silicon nanopore-immunoprotected islets under convective transport. ACS Biomater Sci Eng. 2017; 3(6): 1051-1061.
36. Hajizadeh-Saffar E, Tahamtani Y, Aghdami N, Azadmanesh K, Habibi-Anbouhi M, Heremans Y, et al. Inducible VEGF expression by human embryonic stem cell-derived mesenchymal stromal cells reduces the minimal islet mass required to reverse diabetes. Sci Rep. 2015; 5: 9322.
37. Montazeri L, Hojjati-Emami S, Bonakdar S, Tahamtani Y, Hajizadeh-Saffar E, Noori-Keshtkar M, et al. Improvement of islet engrafts by enhanced angiogenesis and microparticle-mediated oxygenation. Biomaterials. 2016; 89: 157-16.

Original Article

Microarray Profile of Circular RNAs Identifies hsa_circ_0001583 as A New Circular RNA Biomarker for Breast Cancer: A Retrospective Study

Min Zheng, M.M.[1], Wei-Hua Cai, B.M.[2], Mou-Feng Wang, B.M.[1], Yu-Jie Deng, M.M.[1], Ling-Ling Huang, M.M.[1], Yong-Jin Cao, M.M.[2]*

1. Department of Oncology, Fujian Key Laboratory of Precision Medicine for Cancer, The First Affiliated Hospital of Fujian Medical University, Fujian, Fuzhou, P. R. China
2. Department of Thyroid and Breast Surgery, The First Affiliated Hospital of Fujian Hospital of Fujian Medical University, Fujian, Fuzhou, P. R. China

Corresponding Address: Department of Thyroid and Breast Surgery, The First Affiliated Hospital of Fujian Medical University, Fujian, Fuzhou, P. R. China
Email: cyj9803209@fjmu.edu.cn

Received: 22/August/2021, Accepted: 27/April/2022

Abstract

Objective: Breast cancer (BC) is the most common cancer, which is currently the leading cause of cancer death. Circular RNAs (circRNAs) play important roles in cancer, however, circRNAs serving as vital index in BC for guiding treatment have not yet been identified. The aim of our study is to explore a novel kind of potential biomarker for BC.

Materials and Methods: In this retrospective study, the samples used for assays were two groups of breast tumor tissue obtained from four BC patients, including four pairs of tumor tissues and adjacent nontumor samples. The circRNA expression profiles were detected via microarray and validated by real-time quantitative polymerase chain reaction (PCR).

Results: The differentially expressed circRNAs in tested samples were screened and analyzed by using human circRNA microarray. After analysis, considering a fold gene expression change of ≥2.0 and P<0.05, results suggested that 256 circRNAs were significantly up-regulated and 277 circRNAs were significantly down-regulated. Besides, the results of the real-time quantitative PCR assay showed that the expression of hsa_circ_0001583 was significantly up-regulated in BC groups (P<0.05) by real-time quantitative PCR. Therefore, we thought hsa_circ_0001583 might serve as a novel kind of biomarker for BC.

Conclusion: Hsa_circ_0001583 showed significant up-regulation in BC patients with paired adjacent tissues. Many cancer immune pathways were related to has_circ_0001583, including autoimmune thyroid disease, chemokine and T-cell receptor signaling pathways.

Keywords: Breast Cancer, circRNA, hsa_circ_0001583

Cell Journal(Yakhteh), Vol 24, No 9, September 2022, Pages: 500-505

Citation: **Zheng M, Cai WH, Wang MF, Deng YJ, Huang LL, Cao YJ. Microarray profile of circular RNAs identifies hsa_circ_0001583 as a new circular RNA biomarker for breast cancer: a retrospective study. Cell J. 2022; 24(9): 500-505. doi: 10.22074/cellj.2022.8200.**

Introduction

As one of the most common cancers in women, breast cancer (BC) is the primary cause of death from cancer at present. In 2020, the number of newly diagnosed cases of BC was more than 279 thousand and the number of new deaths was about 42 thousand, with 276,480 and 42,170 of them being in women, respectively (1). BC patients in early stages can be cured by local and systemic treatment (2). At present, surgery, adjuvant chemotherapy, endocrine therapy and target-directed therapy were used in the treatment of BC, however, the prognosis of BC was poorly understood because of regional advanced recurrence or distant metastasis. Therefore, to better understand the progression of breast cancer, finding novel molecules as potential biomarkers for BC is essential.

Circular RNAs (circRNAs) were initially found as a kind of covalently closed looped RNAs in viruses (3). Particularly, unlike typical splicing of linear RNA, circRNAs are formed by backward splicing at the 3' and 5' ends of covalent connections (4, 5). Considering the high stability, high specificity and high abundance of circRNAs, previous reports suggested that circRNAs played vital roles in cancers, such as BC, hepatocellular, gastric and colorectal cancer (6-9). CircRNAs usually act as "sponges" of miRNAs which target the 3' UTR region of protein coding RNAs and inhibit target gene expression (4, 10). For example, circBMPR2 can regulate the expression of USP2 via binding to miR-553 as an miRNA sponge (11).

However, circRNAs in BC that can guide treatment have not yet been identified. In this study, a new circRNA, hsa_circ_0001583 which was screened by circRNA microarray attracted our attention. Hsa_circ_0001583 is also associated with many immune response pathways in KEGG analysis. Their roles in BC are still unknown, so it needs to be further explored. And it might act as a novel kind of biomarker for BC.

Material and Methods

CircRNA microarray assay

In this retrospective study, for circRNAs expression screening, we obtained four pairs of tumorous and paracancerous tissues from four triple negative BC patients and extracted total RNA for circRNA microarray assay. In detail, four pairs of BC tissues and paracancerous tissues were sectioned from clinical patients. TRIzol reagent was used for RNA extraction fromtissues, and NanoDrop-1000 and agarose gel electrophoresis were used for RNA concentration and integrity detecting, respectively. According to standard microarray hybridization instructions, the RNA was first purified, and then reverse transcribed to cDNA, cDNA was further transcribed into cy3-fluorescent cRNA, and finally cRNA was hybridized with Human circRNA Arrays (Arraystar). The hybridized microarray was washed with Gene Expression Wash Buffer (Agilent p/n 5188-5325) and the images were scanned by Agilent Scanner G2505C software.

Data analysis by circular microarray

Agilent Feature Extraction software (V11.0.1.1, Agilent santa clara, CA, USA) was used to collect the raw data, then normalized through the quantile method. circRNA expression levels were analyzed by GeneSpring GX V12.1. The circRNAs presenting differential expression between tumors and adjacent tissues with fold gene expression change $\geq$2.0 and $P<0.05$ were identified via statistical analysis. Hierarchical clustering and volcano plotting were constructed for global overview of the significant differentially expressed circRNAs.

Clinical specimens

There are a total of 4 pairs of triple negative BC tissues and paraconcerous normal tissues were sectioned from four clinical patients. This research proposal was approved by The First Affiliated Hospital of Fujian Medical University in 2018.

Total RNA extraction and real-time quantitative polymerase chain reaction

TRIzol reagent (Sigma, USA) was used for total RNA extraction from BC tissues and normal tissues, followed by reverse transcription to cDNA using SuperScript™ III Reverse Transcriptase Kit (Invitrogen, USA) according to the manufacturer's protocol. Real-time quantitative polymerase chain reaction (PCR) assay was performed with QuantStudio™ 5 System (Thermo Fisher Scientific, USA) using 2X PCR master mix (Arraystar, AS-MR-006-25). The relative circRNAs expression level was normalized to internal control gene *ACTB*. Primer sequences are listed in Table S1 (See Supplementary Online Information at www.celljournal.org).

Prediction for BC-related circRNA-miRNA-target gene axis

Targetscan and miRDB (http://www.targetscan.org; http://www.mirdb.org) were used for predicting the miRNAs combined with circRNAs together with the target genes of miRNAs. For analyzing the potential function of circRNAs, the GO enrichment analysis (www.geneontol-ogy.org/) and KEGG pathway analysis (www.genome.jp/kegg/) were performed by DAVID (https://david.ncifcrf.gov/tools.jsp) online software.

Ethical statement

The clinical samples were obtained from The First Affiliated Hospital of Fujian Medical University. This study was approved by the Ethics Committee of The First Affiliated Hospital of Fujian Medical University (Fuzhou, China, project number [2016]073), and written consent was obtained from all patients involved.

Data availability

The circRNA expression profile data are available in the GEO database (accession number GSE165884).

Statistical analysis

All statistical data plotting was performed with Graphpad Prism V8.0 (GraphPad Software Inc., San Diego, CA, USA). Every experiment was conducted in three replicate. Significant differences between data was analyzing by Student's t test ($P<0.05$) and the significance of gene function enrichment was determined by Fisher's Exact Test.

Results

The circRNAs presenting differential expression were identified in BC

Four pairs of BC patient samples and paracancerous tissues were used to screen the potential involvement of circRNAs in BC via the high-throughput circRNA microarray assays. The results shown in Figure 1A and Figure 1B were the quantile normalization and total detected circRNA types. The scatter plot suggested that 360 circRNAs were up-regulated, while 344 circRNAs were discovered with down-regulation (Fig.1C). Additionally, by comparing the case group with the control group, a volcano plot revealed that a total of 533 circRNAs presented differential expression. In detail, 256 circRNAs were found to be significantly up-regulated and 277 circRNAs were significantly differentially down-regulated based on fold expression change $\geq$2.0 and $P<0.05$ (Fig.1D). Figure 1E indicates the distinct disparity from BC tissue to their adjacent samples. The results in Figure 1F showed the number and distribution of these circRNAs on the different human chromosomes.

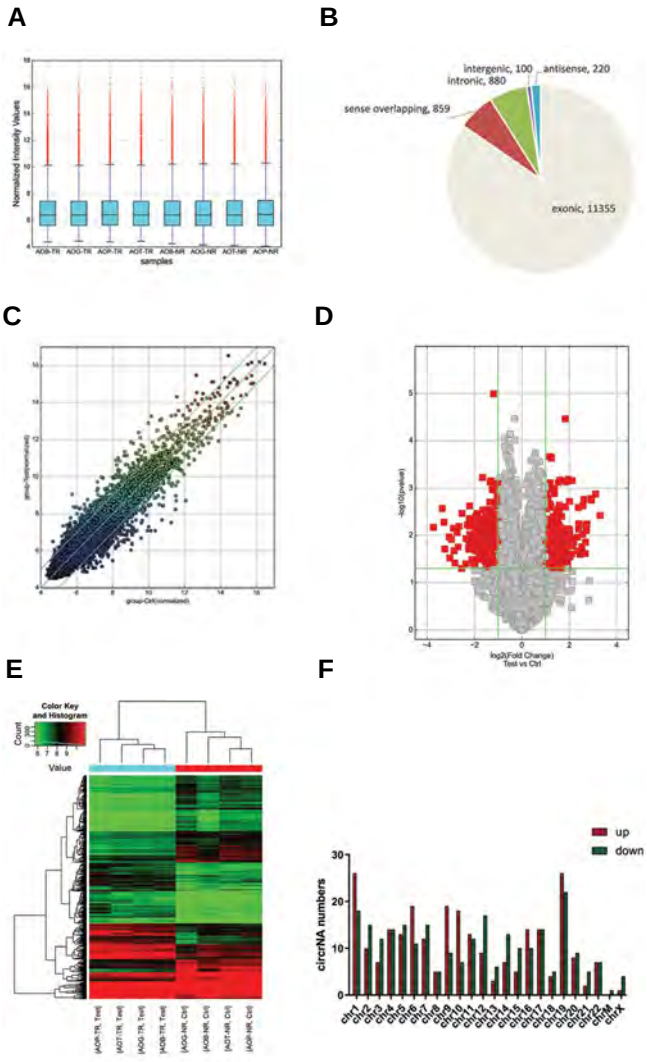

Fig.1: circRNA expression profile and differentially regulated circRNAs in BC. **A.** The quantile normalization results of Arraystar circRNA microarray for 8 samples. **B.** Different types in all circRNA expression profile. **C.** Scatter plot for assessing the variation in circRNA expression. **D.** Volcano plot indicated the differentially expressed circRNAs in BC samples and adjacent tissues based on fold expression change ≥2 and P<0.05. **E.** Hierarchical clustering heatmap for differentially expressed circRNAs. **F.** The distribution of differentially expressed circRNAs on human chromosomes. circRNA; Circular RNAs (circRNAs) and BC; Breast cancer.

Potential functional analysis of differentially expressed circRNAs

To evaluate the functions of differentiated expressed circRNAs, we perfomed GO and pathway enrichment analysis using the circRNA target genes. As the results show in Figure 2A, by biological process analysis, these circRNAs might act in negative transcriptional regulation associated with the RNA polymerase II promoter, protein ubiquitination modification in ubiquitin-dependent protein catabolism, cell shape, regulation of cellular signal transduction mediated by small GTPase, GTPase activity regulation, protein nuclear export, protein folding in the endoplasmic reticulum, actin cytoskeleton organization, protein polyubiquitination, and cell-cell adhesion. Cellular component enrichment results showed that the host genes can be part of the cytosol, focal adhesion, cytoplasm, membrane, stress fibers, extracellular exosomes, the actin cytoskeleton, the mitotic spindle, the extracellular matrix, and cell-cell adherens junctions (Fig.2B). Molecular function results of the differentially expressed circRNAs are shown in Figure 2C.

In addition, KEGG pathway analysis showed that differentially expressed circRNAs could be involved in focal adhesion, actin cytoskeleton regulation, bacterial invasion of epithelial cells, ubiquitin mediated proteolysis, proteoglycans in cancer, ribosome, and amoebiasis (Fig.2D).

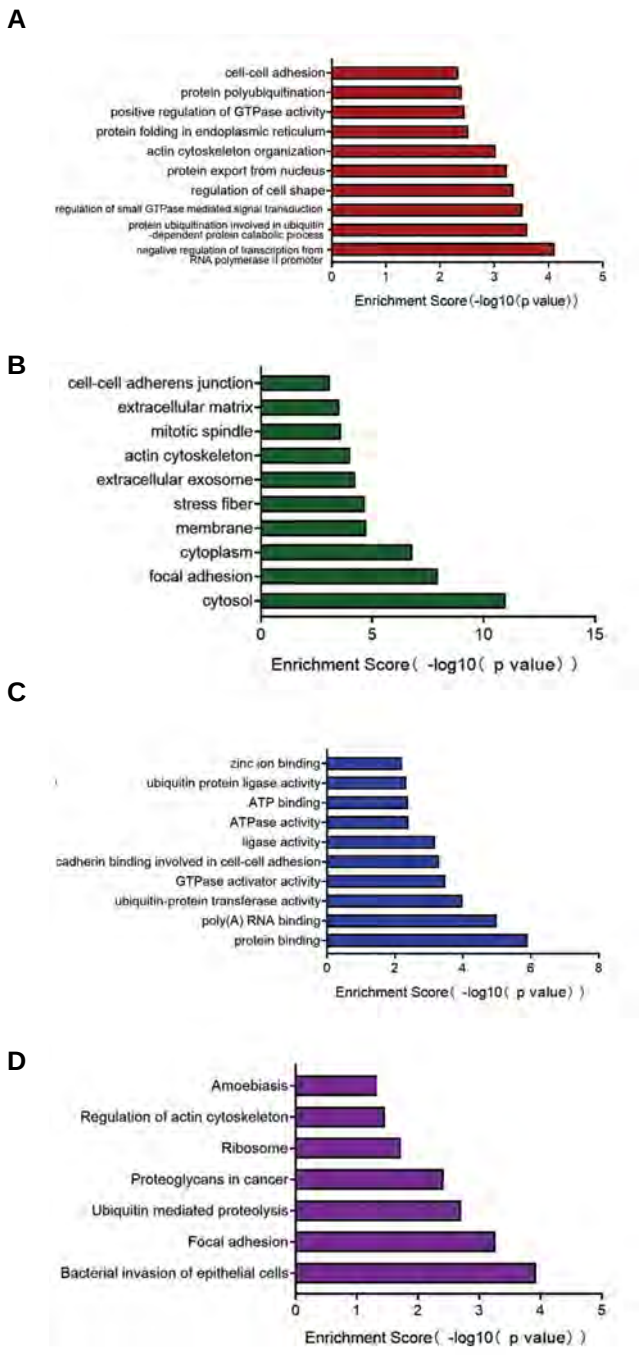

Fig.2: Predicting the functions of differentially expressed circRNA host genes. **A.** Top ten biological processes associated with the differentially expressed circRNAs host genes arranged by enrichment score. **B.** Top ten cellular components of differentially expressed circRNAs host genes. **C.** Top ten molecular functions of differentially expressed circRNAs host genes. **D.** Significant KEGG pathway enrichment results of differentially expressed circRNAs host genes.

Diagnostic values of hsa_circ_0001583 in BC

To further study the importance of circRNAs in BC, we detected the expression change of differentially expressed circRNAs by real-time quantitative PCR, including hsa_circ_0000700, hsa_circ_0089153, hsa_circ_0067301, hsa_circ_0001583, hsa_circ_0001589 and hsa_circ_0039908 (Fig.3A). Interestingly, consistent with the microarray results, hsa_circ_0001583 presented the most significant up-regulation in 4 BC tissues (Fig.3B). In fact, hsa_circ_0001583 is generated from *H1-2* gene, which is a histone H1 protein binding to linker DNA (Fig.3C). Therefore, we thought hsa_circ_0001583 might serve as a novel kind of biomarker for BC.

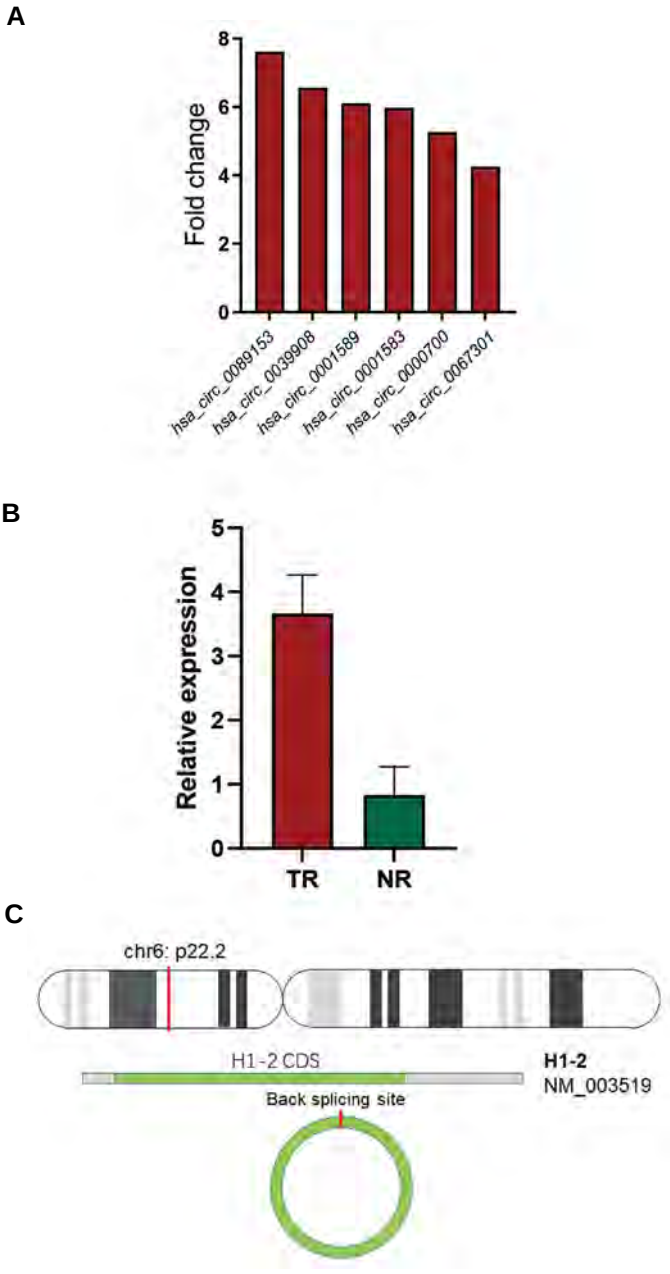

Fig.3: Validation of differentially expressed circRNAs by realtime quantitative polymerase chain reaction (RT-qPCR). **A.** 6 selected up-regulated circRNAs for RT-qPCR validation. **B.** *hsa_circ_0001583* was significantly up-regulated in breast cancer tissues (P=0.0014). **C.** The genome locus and host gene of hsa_circ_0001583.

Prediction of miRNAs acting on hsa_circ_0001583 and downstream genes

To study the function of hsa_circ_0001583, the hsa_circ_0001583-miRNA-mRNA network was predicted (Fig.4A). In detail, the top 5 related miRNAs were exhibited in Figure 4B, containing hsa-miR-6815-3p, hsa-miR-324-3p, hsa-miR-103a-2-5p, hsa-miR-4778-3p and hsa-miR-647, while Figure 4B also shows the possible binding sites between hsa_circ_0001583 and its related miRNAs.

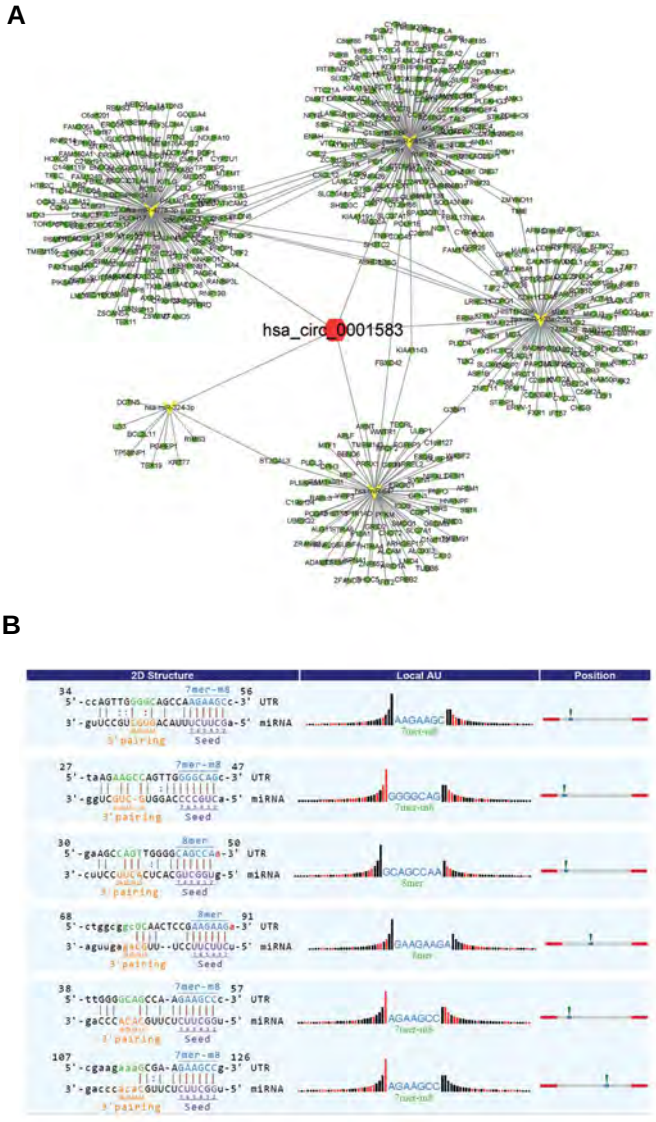

Fig.4: ceRNA network of hsa_circ_0001583. **A.** The predicted hsa_circ_0001583 sponged miRNA and miRNA target genes. **B.** The potential binding sited of hsa_circ_0001583 and sponged miRNAs.

Analyzing the fuctions of hsa_circ_0001583 ceRNA genes

GO enrichment analysis revealed that the target genes of those candidate miRNAs are related to many biological processes and pathways, including negative transcriptional regulation of RNA polymerase II promoter, signal transduction mediated by Rho protein, covalent chromatin modification, protein K48-linked ubiquitination, adaptive

immune response, kinase activity regulation, cell motility, ventricular septum development, and cell proliferation (Fig.5A). The cellular component and molecular function enrichment analysis results are shown in Figure 5B and Figure 5C. KEGG analysis revealed that several immune response pathways are associated with candidate miRNAs, including long-term potentiation, T/B-cell receptor signaling pathway, bile secretion, oxytocin and calcium signaling pathway, infection of vibrio cholerae, proteolysis mediated by ubiquitin, axon guidance (Fig.5D). These results suggested that hsa_circ_0001583 was strongly associated with BC development, which will pave the way for further research in the future.

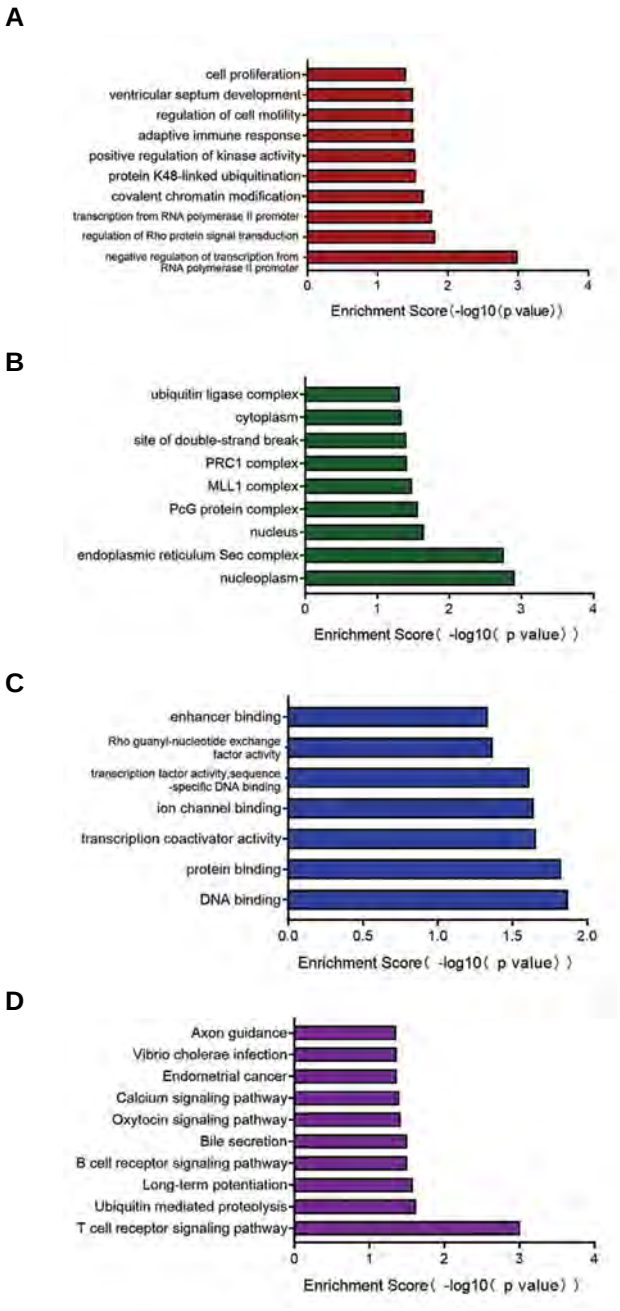

Fig.5: The GO/pathway enrichment analysis of hsa_circ_0001583 ceRNAs. **A.** Top ten GO_BP enrichment terms of candidate circRNA ceRNAs. **B.** The significant GO_CC enrichment results of candidate circRNA ceRNAs. **C.** The significant GO_MF enrichment results of candidate circRNA ceRNAs. **D.** KEGG pathway analysis revealed that several immune related pathways associated with hsa_circ_0001583.

Discussion

It has been found in previous studies that circRNAs exhibited pivotal regulatory functions in cancer progression and carcinogenesis (12). The circRNAs are stable due to the lack of 5' or 3' polarities or polyadenylated tails (13). Moreover, circRNAs are also abundant, showing the high conservation, together with structural stability, timing, organization, and disease-specific activity in eukaryotic cells (14). Therefore, circRNAs are extremely suitable to serve as biomarkers. It has been reported that circEPSTI1 is a prognostic marker in triple-negative BC (9). Hsa_circ_0072995, hsa_circ_0072309 and hsa_circ_0001982 have also been reported in BC (15-17). In the cytoplasm, circRNA can function as miRNA sponges that bind miRNAs, thus impeding their binding and suppressing their target genes. In human astrocyte cells, circHIPK2 can bind miR124-HG, which modulate astrocyte cell autophagy and endoplasmic reticulum stress response (18). During differentiation of human epidermal stem cells, circZNF1 functions as a sponge for miR-23b-3p (19), and circBIRC6 is a sponge for miR-34a and miR-145 which then regulate differentiation of human stem cells (20). Although there have been so many studies, there is no known biomarker that is more clinically appropriate. Therefore, this study aimed to identify a potential biomarker in breast cancer.

In our work, the potential participation of circRNAs in BC was investigated using four pairs of BC patient samples and paracancerous tissues. The results suggested that 256 circRNAs were differentially up-regulated and 277 circRNAs were differentially down-regulated. In addition, we verified the expression of six differentially up-regulated circRNAs in the filtered library, finding that hsa_circ_0001583 expression was indeed up-regulated. Hence, we though that hsa_circ_0001583 might be a novel biomarker in BC. Furthermore, the top 5 related miRNAs are shown by predicting the hsa_circ_0001583-miRNA-mRNA network. Importantly, KEGG analysis revealed that several immune response pathways are associated with candidate miRNA, including long-term potentiation, T/B-cell receptor signaling pathway, bile secretion, oxytocin and calcium signaling pathway, infection of vibrio cholerae, proteolysis mediated by ubiquitin, and axon guidance. These results suggested that hsa_circ_0001583 was strongly associated, which will lay the foundation for further research in the future.

Objectively, this study also has some limitations. At first, this study is a retrospective study with a small sample which would be better with initial or external validation. Second, *in vivo* or *in vitro* functional studies of hsa_circ_0001583 are still lacking. Third, the relationship between hsa_circ_0001583 and long-term outcomes were not investigated in BC patients.

Taken together, we thought hsa_circ_0001583 might act as a biomarker for BC related to the immune response of the body. As is well known, BC immunology has progressed tremendously over the last decade, which is an

important treatment in BC. Therefore, our future research will focus on hsa_circ_0001583 in the immunology and mechanism of BC.

Conclusion

We utilized 4 pairs of BC neoplasm tissues and their paracancerous tissues to investigate the potential of circRNAs biomakers in BC by applying circRNA microarray and real-time quantitative PCR methods. Importantly, hsa_circ_0001583 was discovered to be significantly up-regulated in breast tumors, and it might be an excellent biomarker for BC diagnosis and may modulate tumor immunology through ceRNA mechanism.

Acknowledgements

We are grateful to Dr. Zong-Cai Wang in the First Affliliated Hospital of Fujian Medicial University for clinial sample collection and Dr. Xia Chen for technical support. The present study was financially supported by the Natural Science Foundation of Fujian Province, China (2017J01285). The authors report no conflicts of interest in this work.

Authors' Contribution

Y.-J.C., W.-H.C.; Designed and perform the research, analyzed the data and wrote the manuscript. M.Z., M.-F.W.; Performed the research and analyzed the data. Y.-J.D., L.-L.H.; Collected and analyzed the clinical data. All authors read and approved the final manuscript.

References

1. Siegel RL, Miller KD, Jemal A. Cancer statistics, 2020. CA Cancer J Clin. 2020; 70(1): 7-30.
2. Noh JM, Choi DH, Huh SJ, Park W, Yang JH, Nam SJ, et al. Patterns of recurrence after breast-conserving treatment for early stage breast cancer by molecular subtype. J Breast Cancer. 2011; 14(1): 46-51.
3. Kolakofsky D. Isolation and characterization of Sendai virus DI-RNAs. Cell. 1976; 8(4): 547-55.
4. Memczak S, Jens M, Elefsinioti A, Torti F, Krueger J, Rybak A, et al. Circular RNAs are a large class of animal RNAs with regulatory potency. Nature. 2013; 495(7441): 333-338.
5. Wang F, Nazarali AJ, Ji S. Circular RNAs as potential biomarkers for cancer diagnosis and therapy. Am J Cancer Res. 2016; 6(6): 1167-1176.
6. Qin M, Liu G, Huo X, Tao X, Sun X, Ge Z, et al. Hsa_circ_0001649: A circular RNA and potential novel biomarker for hepatocellular carcinoma. Cancer Biomark. 2016; 16(1): 161-169.
7. Lu J, Zhang PY, Li P, Xie JW, Wang JB, Lin JX, et al. Circular RNA hsa_circ_0001368 suppresses the progression of gastric cancer by regulating miR-6506-5p/FOXO3 axis. Biochem Biophys Res Commun. 2019; 512(1): 29-33.
8. Ji W, Qiu C, Wang M, Mao N, Wu S, Dai Y. Hsa_circ_0001649: A circular RNA and potential novel biomarker for colorectal cancer. Biochem Biophys Res Commun. 2018; 497(1): 122-126.
9. Chen B, Wei W, Huang X, Xie X, Kong Y, Dai D, et al. circEPSTI1 as a prognostic marker and mediator of triple-negative breast cancer progression. Theranostics. 2018; 8(14): 4003-4015.
10. Hansen TB, Kjems J, Damgaard CK. Circular RNA and miR-7 in cancer. Cancer Res. 2013; 73(18): 5609-5612.
11. Liang Y, Song X, Li Y, Ma T, Su P, Guo R, et al. Targeting the circBMPR2/miR-553/USP4 axis as a potent therapeutic approach for breast cancer. Mol Ther Nucleic Acids. 2019; 17: 347-361.
12. Jeck WR, Sorrentino JA, Wang K, Slevin MK, Burd CE, Liu J, et al. Circular RNAs are abundant, conserved, and associated with ALU repeats. RNA. 2013; 19(2): 141-157.
13. Li J, Yang J, Zhou P, Le Y, Zhou C, Wang S, et al. Circular RNAs in cancer: novel insights into origins, properties, functions and implications. Am J Cancer Res. 2015; 5(2): 472-480.
14. Rybak-Wolf A, Stottmeister C, Glažar P, Jens M, Pino N, Giusti S, et al. Circular RNAs in the mammalian brain are highly abundant, conserved, and dynamically expressed. Mol Cell. 2015; 58(5): 870-885.
15. Zhang HD, Jiang LH, Hou JC, Zhou SY, Zhong SL, Zhu LP, et al. Circular RNA hsa_circ_0072995 promotes breast cancer cell migration and invasion through sponge for miR-30c-2-3p. Epigenomics. 2018; 10(9): 1229-1242.
16. Yan L, Zheng M, Wang H. Circular RNA hsa_circ_0072309 inhibits proliferation and invasion of breast cancer cells via targeting miR-492. Cancer Manag Res. 2019; 11: 1033-1041.
17. Tang YY, Zhao P, Zou TN, Duan JJ, Zhi R, Yang SY, et al. Circular RNA hsa_circ_0001982 promotes breast cancer cell carcinogenesis through decreasing miR-143. DNA Cell Biol. 2017; 36(11): 901-908.
18. Huang R, Zhang Y, Han B, Bai Y, Zhou R, Gan G, et al. Circular RNA HIPK2 regulates astrocyte activation via cooperation of autophagy and ER stress by targeting MIR124-2HG. Autophagy. 2017; 13(10): 1722-1741.
19. Kristensen LS, Okholm TLH, Venø MT, Kjems J. Circular RNAs are abundantly expressed and upregulated during human epidermal stem cell differentiation. RNA Biol. 2018; 15(2): 280-291.
20. Yu CY, Li TC, Wu YY, Yeh CH, Chiang W, Chuang CY, et al. The circular RNA circBIRC6 participates in the molecular circuitry controlling human pluripotency. Nat Commun. 2017; 8(1): 1149.

Original Article

An Effective Method for Decellularization of Human Foreskin: Implications for Skin Regeneration in Small Wounds

Shima Rahmati, Ph.D.[1], Ali Jalili, Ph.D.[1]*, Mehdi Banitalebi Dehkordi, Ph.D.[2]*, Michelle Przedborski, Ph.D.[3]

1. Cancer and Immunology Research Center, Research Institute for Health Development, Kurdistan University of Medical Sciences, Sanandaj, Iran
2. Department of Molecular Medicine, School of Advanced Technologies, Shahrekord University of Medical Sciences, Shahrekord, Iran
3. Department of Applied Mathematics, University of Waterloo, Waterloo, ON, Canada

Corresponding Addresses: P.O.Box: 6618634683, Cancer and Immunology Research Center, Research Institute for Health Development, Kurdistan University of Medical Sciences, Sanandaj, Iran
P.O.Box: 8815713471, Department of Molecular Medicine, School of Advanced Technologies, Shahrekord University of Medical Sciences, Shahrekord, Iran
Emails: ali130@gmail.com, mehdibanitalebi@gmail.com

Received: 03/March/2021, Accepted: 28/August/2021

Abstract

Objective: Acellular matrices of different allogeneic or xenogeneic origins are widely used as structural scaffolds in regenerative medicine. The main goal of this research was to optimize a method for decellularization of foreskin for skin regeneration in small wounds.

Materials and Methods: In this experimental study, the dermal layers of foreskin were divided into two sections and subjected to two different decellularization methods: the sodium dodecyl sulfate method (SDS-M), and our optimized foreskin decellularization method (OFD-M). A combination of non-ionic detergents and SDS were used to decellularize the foreskin in OFD-M. The histological, morphological, and biomechanical properties of both methods were compared. In addition, human umbilical cord mesenchymal stem cells (hucMSCs) were isolated, and the biocompatibility and recellularization of both scaffolds by hucMSC were subsequently determined.

Results: We observed that OFD-M is an appropriate approach for successful removal of cellular components from the foreskin tissue, without physical disturbance to the acellular matrix. In comparison to SDS-M, this new bioscaffold possesses a fine network containing a high amount of collagen fibers and glycosaminoglycans (GAG) ($P \leq 0.03$), is biocompatible and harmless for hucMSC (viability 91.7%), and exhibits a relatively high tensile strength.

Conclusion: We found that the extracellular matrix (ECM) structural integrity, the main ECM components, and the mechanical properties of the foreskin are well maintained after applying the OFD-M decellularization technique, indicating that the resulting scaffold would be a suitable platform for culturing MSC for skin grafting in small wounds.

Keywords: Decellularized Scaffolds, Foreskin, Mesenchymal Stem Cell

Cell Journal(Yakhteh), Vol 24, No 9, September 2022, Pages: 506-514

Citation: **Rahmati Sh, Jalili A, Banitalebi Dehkordi M, Przedborski M. An effective method for decellularization of human foreskin: implications for skin regeneration in small wounds. Cell J. 2022; 24(9): 506-514. doi: 10.22074/cellj.2022.8005.**

Introduction

For decades, skin grafts have been used to restore wound healing defects following trauma, vascular diseases, and cancer (1). Skin grafts can reduce the complexity of treatment and minimize the risk of infection and hospitalization, to achieve satisfactory repair results in patients with chronic or recurrent ulcers (2). However, the availability of adequate healthy skin, remains as an overwhelming obstacle. In addition, scar formation and deformity of the donor's skin is a problem that must be considered. To address these challenges, scientists and surgeons work collaboratively to develop appropriate bioengineered and synthetic alternatives that promote the healing of the wounded skin (1). Moreover, it has been shown that when scaffolds are located within the defect, they protect against dehydration, contaminants, and microorganisms (3).

Acellular dermal matrix (ADM) is one of the most widely used grafts in skin transplantation today. ADM can be derived from various allogeneic or xenogeneic sources, such as human cadavers and animal dermises (4). Decellularized extracellular matrix (ECM) from the target tissue is the ideal scaffold for tissue engineering. Decellularization technique, in which most cell components are removed by physical and/or chemical procedures, enables researchers to obtain cell-free, natural ECM that is primarily made up of collagen and glycosaminoglycans (GAGs). ECM retention, especially the maintenance of structural integrity of the collagen mesh, is very important for the effectiveness of recellularization (5). Collagen provides tensile strength and promotes cell migration and tissue development by controlling cellular adhesion. In fact, since collagen has high electrostatic properties, it draws water in the interstitial spaces and causing it to inflate (6, 7). Thus ,it is important to take advantage of such characteristics to achieve a scaffold with ideal physicochemical properties for effective tissue regeneration.

A well-known technique in regenerative medicine

involves the use of a tissue scaffold in combination with stem cells. Because of their trophic and paracrine functions, mesenchymal stem cells (MSCs) can improve cutaneous regeneration. Specifically, they can improve wound healing by enhancing keratinocyte and fibroblast migration following transplantation (8). MSCs secrete several cytokines and growth factors [e.g., vascular endothelial growth factor (VEGF), epidermal growth factor (EGF), stromal cell derived factor 1 (SDF-1), and angiopoietin-1], which can act as chemo-attractants to induce endogenous cell recruitment to the injured tissue (9). The human umbilical cord is considered to be an important and non-invasive source of MSCs (10). While these cells may have a valuable impact on healing, the harsh environment of the wound site limits the grafting, retention, and transplanted cells' survival rate. Thus, the delivery of cells into the wound site through scaffold-based cell applications remains a significant challenge in regenerative medicine (11).

The multifaceted nature of human foreskin, which is a highly vascularized and densely innervated bilayer tissue, is comparable to that of few other parts of the human anatomy. Foreskin circumcision has ancient roots, but its modern version dates back to the early 19th century (12). Foreskin circumcision is performed on most male children in Iran, providing an abundant supply of waste tissue that can be used as a skin graft without damaging the donor. Consequently, in the present study, we compare two methods of decellularization, with the goal of optimizing a technique for creating a foreskin acellular matrix (FAM).

Materials and Methods

Foreskin acellular matrix preparation

In this experimental study, the foreskin samples used in this study were from boys aged one month to four years, and were obtained from Imam-Ali Clinic, Shahre-Kord, with parental informed consent. Specimens were transferred to the laboratory in phosphate-buffered saline (PBS, BIO-IDEA, Iran) containing 10% gentamicin and stored for 6 hours at 4°C. The outer adipose layer was then removed using a scalpel after washing the specimen in PBS. The isolated dermal layers were divided into two parts and subjected to two decellularization methods: the optimized foreskin decellularization method (OFD-M), and the sodium dodecyl sulfate method (SDS-M, Sigma St. Louis, MO), which are both described below.

The SDS-M method was previously reported elsewhere (13). Briefly, samples were placed in SDS 1% in deionized water, and fresh SDS/H_2O media were substituted every 6 hours for three days until the sample color was completely transparent. Finally, specimens were placed in PBS for 2 hours to remove nuclei, cell residues, and detergents from the tissue.

For the OFD-M, the samples were placed in 5% SDS and incubated for 6 hours, then washed for 1 hour in distilled water. In the next step, 0.05% trypsin and 0.01% ethylenediaminetetraacetic acid (EDTA, Life Technologies, Carlsbad, CA), were added to the samples. The specimens were incubated for 6 hours, followed by a wash with Hank's balanced salt solution (HBSS, BIO-IDEA, Iran). The tissues were digested by Triton-X100 (1%) for 1 hour (Bio Basic Inc. cas # 9002-93-1). All the above steps were performed on a shaker (IKA-WERKE Hs501, 90 rmp), and the solutions were replaced every 2 hours. Finally, the tissue was submerged in the HBSS solution at 4˚C for 48 hours to remove residual SDS (Fig. S1, See Supplementary Online Information at www.celljournal.org) (14).

Both groups of FAM samples were rinsed several times with distilled water and subsequently stored in 75% alcohol at -20˚C. Prior to testing, samples were subjected to UV radiation for 20 m.

Colorimetric detection of sodium dodecyl sulfate

The amount of SDS remaining in the scaffolds was measured during the experiments for each method, using a colorimetric assay with methylene blue. First, the standard curve was obtained by measuring the optical density (OD) (Fig.S2A, See Supplementary Online Information at www.celljournal.org). Next, to determine the amount of residual SDS in the tissues, 1 g of FAMs was weighed and prepared according to the method explained by Alizadeh et al. (15). Finally, each sample's OD was measured at 650 nm (microplate reader, STAT FAX 2100), and a standard curve was used to determine the amount of SDS in each sample.

Histological analysis

To assess the decellularization procedure's efficiency regarding ECM integrity and the removal of cell components, the samples were fixed in 10% formalin solution and then embedded in paraffin. Then three 5 to 6 µm thick serial sections were prepared and mounted on slides for further analysis (microtome Leitz1512, Ramsey, USA). The slides were stained with hematoxylin and eosin (H&E) as follows: the samples were first immersed in hematoxylin and acid-alcohol for 6 minutes and 30 seconds, respectively. After washing with distilled water, the sections were submerged in eosin for 1 minute. Finally, serially diluted alcohol (70°, 90°, and 100°) were used for dehydration. The number of residual cells was then observed in three microscopic fields of each stained slide using a 10x objective lens. to analyze the collagen and elastic fibers the sections were also stained with Masson's trichrome following a standard protocol

(16). Briefly, the slides were immersed in Bouin's fluid overnight at room temperature, then rinsed with water and placed in Weigert's haematoxylin solution for 5 minutes, then immersed in Biebrich scarlet-acid fuchsin for 15 minutes. After that, they were rinsed in water and placed in phosphomolybdic/phosphotungstic acid for 15 minutes, then aniline blue stain for 10 minutes, and finally rinsed in water. The slides were finally placed in 1% acetic acid for 5 minutes and dehydrated by rinsing with 100% ethanol.

To assess the efficacy of cell removal and the number of remaining nuclei in decellularized scaffolds in each method, samples were stained with the DNA staining dye Hoechst 33258 (Sigma-Aldrich Corp., MI, USA). After preparation of paraffin-embedded sections, deparaffinization was performed, and the samples were stained by 1:5000 diluted Hoechst in PBS for 30 seconds in a dark room. Finally, the slides were washed with PBS and then visualized using a fluorescence microscope (Nikon-TS-100F, Tokyo, Japan). The collagen content was analyzed using ImageJ software (NIH, Bethesda, MD) as previously reported (17).

DNA quantification

The amount of remaining DNA in the decellularized samples was measured by Geno PlusTM Mini extraction kit (GG2001, Viogene, Taipei, Taiwan). Specifically, 30 mg of each dried FAM and native tissue samples were homogenized in 180 µL of lysis buffer, and after adding 20 µL of proteinase K, the rest of the protocol was carried out in accordance with the manufacturer's instructions (GG2001). Finally, DNA was dissolved in trace HCl (10 mM, pH=9), and the quality and quantity of DNA was evaluated by nanodrop 2000 (Thermo Scientific, USA).

Morphological analysis by scanning electron microscopy

To determine the pore sizes and ensure that the ECM structure has remained intact, the samples were analyzed by scanning electron microscopy (SEM). The samples were fixed in 2.5% glutaraldehyde fixative solution (Sigma-Aldrich, USA) for 90 minutes at room temperature, then washed with PBS to remove the fixative solution. Dehydration was carried out through rinsing the samples with serially diluted ethanol (30, 50, 70, 80, 90, and 100%); 10 minutes for each concentration (18). Finally, the samples were dried, fixed on SEM stubs, and coated with gold (Desk Sputter Coater-DSR1). The samples were then subjected to SEM (Philips XL 30, North Billerica, MA) examination, and multiple images were taken using fluorescence microscope.

Glycosaminoglycans quantification

The GAG content is an indicator of the degree of structural modification in decellularized tissue (18). The standard curve was drawn using the chondroitin 6-sulfate kit (KGAG96, Kiazist, Iran) according to the manufacturer's instructions (Fig.S2B, See Supplementary Online Information at www.celljournal.org). Next, 20 mg of each sample (dried FAMs and native) individually was digested through incubation with 400 µL papain at 65˚C for 16 hours, then centrifuged at 8000g for 15 minutes. After that, the supernatants were transferred into 1.5 mL eppendorf tubes and 50 µL of protein precipitant was added to each tube and centrifuged at 8000g for an additional 15 minutes. Finally, 200 µL of GAG reagent was added to 30 µL of each sample or the standard solution, in triplicates (96 well plate). Finally, the OD of the test was obtained at 510-560 nm using a microplate reader (Stat Fax 2100, Awareness Technology, Palm City, FL).

Collagenase assay

One of the most reliable and cost-effective methods for the measurement of collagen content is biochemical calculation of hydroxyproline (19). The amount of hydroxyproline in the decellularized samples was determined by employing the Kiazist Kit (KHPA96, Kiazist, Tehran, Iran) according to the manufacturer's instructions. First, the standard curve was obtained according to the kit instructions (Fig.S2C, See Supplementary Online Information at www.celljournal.org). Next, 20 mg of native and dried FAM samples were homogenized in 100 µL H_2O plus 100 µL of 12M HCL and incubated for 4 hours at 120C. Oxidation solution and activated charcoal were then added to the samples, and the mixture was centrifuged at 12000g for 15 minutes. The supernatants were harvested, and the OD of the test was obtained at 540-560 nm using the microplate reader in triplicates.

Biomechanical properties: tensile strength

To determine the mechanical properties of the scaffolds, FAMs, and native foreskins were tested by a tensile-test device (TANSAM. STM-1). Briefly, samples of size 2×5 cm were prepared and clamped to the sample holders, then stretched at a speed of 10 mm/minutes. until tearing. The stiffness (N/m), elastic modulus, and maximum force (N) were determined from the resulting stress-strain curve.

Isolation of mesenchymal stem cells from human umbilical cord

The protocol was approved by the Ethical Research Committee of Kurdistan University of Medical Sciences (KUMS), according to the criteria set by the declaration of Helsinki and numbered as #IR.MUK.REC.1397.220. Informed consent was obtained from all the participating women (for the umbilical cord). In the next step, the human umbilical cord mesenchymal stem cells (hucMSCs) were isolated from the entire umbilical cord

using the modulated explant/enzyme method (MEEM) and characterized as previously described (20). The expression of CD29, CD90, CD105, CD34, and CD45 on the cell surface of hucMSCs was analyzed by flow cytometry. Furthermore, hucMSCs were subjected to differentiation into adipogenic, osteogenic, and chondrogenic cell phenotypes (Fig.S3, See Supplementary Online Information at www.celljournal.org). Finally, the isolated cells were cultured in a T75 culture flasks (SPL, Pocheon-si, South Korea) containing Dulbecco's modified Eagle's medium-low glucose (DMEM, Gibco, Thermo Fisher Science, US) supplemented with 13% fetal bovine serum (FBS, Gibco, USA) and 100 IU/mL-100 mg/mL penicillin-streptomycin (Gibco, USA). The flasks were placed in a humidified incubator with 5% CO_2 at 37˚C. Every 2 days, the medium was replaced with fresh medium until the cells were confluent, then they were detached using 0.25% trypsin-0.04% EDTA (Gibco, USA) for cell passages.

Cell /Contact cytotoxicity assay

The biocompatibility/cytotoxicity of FAMs was evaluated through the co-incubation of scaffolds with hucMSCs. Specifically, 2×10^5 cells/well of hucMSCs were seeded in a six-well plate and were allowed to grow until reaching confluency. Then, native tissue and both groups of FAMs (3 mm^2) were placed inside each well. Tissues and medium were subsequently removed from the wells, at time intervals of 48 hours and 72 hours, respectively to evaluate the cytotoxicity of FAMs. Next, 1 ml of FBS-free medium containing 50 µL of resazurin (Kiazist, Iran) was added to each well and the samples were incubated for 4 hours at 37˚C. Finally, the OD was measured at 520-570 nm in a microplate reader (State Fax 2100), and the viability percentage of each of the three groups of hucMSCs was analyzed.

Recellularization of FAMs with hucMSCs

The hucMSCs were seeded in a six-well plate (2×10^5 cells/well) in DMEM medium supplemented with 10% FBS and 1% penicillin-streptomycin (Pen/Strep) and subsequently incubated at 37°C and 5% CO_2. The optimized foreskin decellularization FAM (OFD-FAM) samples were washed in PBS, cut into 10 mm pieces, and placed on hucMSCs for 24 hours. The resulting samples were monitored for 8 days, and recellularization was investigated by H&E and Hoechst staining. Furthermore, the morphology and the attachment of the hucMSCs onto the surfaces of FAMs were observed by SEM.

Statistical methods

Each experiment was performed three times, and the mean values of the results were evaluated. All data were analyzed using SPSS statistical software (18.0 version, SPSS Inc., Chicago, IL, USA). One-way analysis of variance (ANOVA) and Tukey's post-hoc test were performed to compare datasets. Mean differences were considered significant at $P<0.05$. All numerical data analyses were performed using GraphPad Prism 8.0 (GraphPad, CA, USA).

Results

Macroscopic observations

Macroscopic evaluation of the intact human foreskin specimens showed a pink appearance with a fatty layer before the decellularization process (Fig.S1A, See Supplementary Online Information at www.celljournal.org). The tissues were white after decellularization via the OFD-M, implying that the epidermoid layers and cells were probably removed, without any physical tissue disturbance or effects on the elasticity (Fig.S1B, See Supplementary Online Information at www.celljournal.org). However, FAMs obtained by SDS-M showed a shrinking appearance with a rough surface and a rigid structure. In contrast, FAMs obtained by OFD-M were smooth and tensile. (Fig.S1C, See Supplementary Online Information at www.celljournal.org), indicating that they might have more collagens and fewer cells compared to the FAMs obtained by SDS-M.

Histological staining and electron microscopic analysis

H&E staining of the two FAM groups revealed a complete lack of an epidermal layer and residual cells in the group of FAMs obtained by the OFD-M and a partial removal of cells by the SDS-M, compared to the intact tissue. It was also found that the ECM is well preserved in FAMs obtained via the OFD-M (Fig.1A). Masson's trichrome staining, which appears blue in the presence of collagen, indicated that collagen is conserved in the OFD-FAM but not in FAMs obtained via the SDS-M (Fig.1B). ImageJ analysis further confirmed well-maintained collagen content in the OFD-FAM group in comparison to the SDS-FAM group (native tissue 65.1%, OFD-M 74.5%, and SDS-M 69.4%).

Furthermore, Hoechst staining confirmed the complete removal of the cells without residual DNA in the OFD-FMS group, whereas this was not the case in the group obtained by the SDS-M (Fig.1C). We further investigated the degree of cell removal, the pore size, and the matrix fibers' structure in the intact tissue and the two FAM groups using a scanning electron microscope. As illustrated by Figure 2, the OFD-FAMs displayed a network of collagen fibers with high structural integrity and appropriate pore size with no deformation or disruption of the tissue and no residual cells. We see in Figure 3 that this was not the case for FAMs obtained by the SDS-M: the matrix, in this case, was highly irregular, and there were residual cells present.

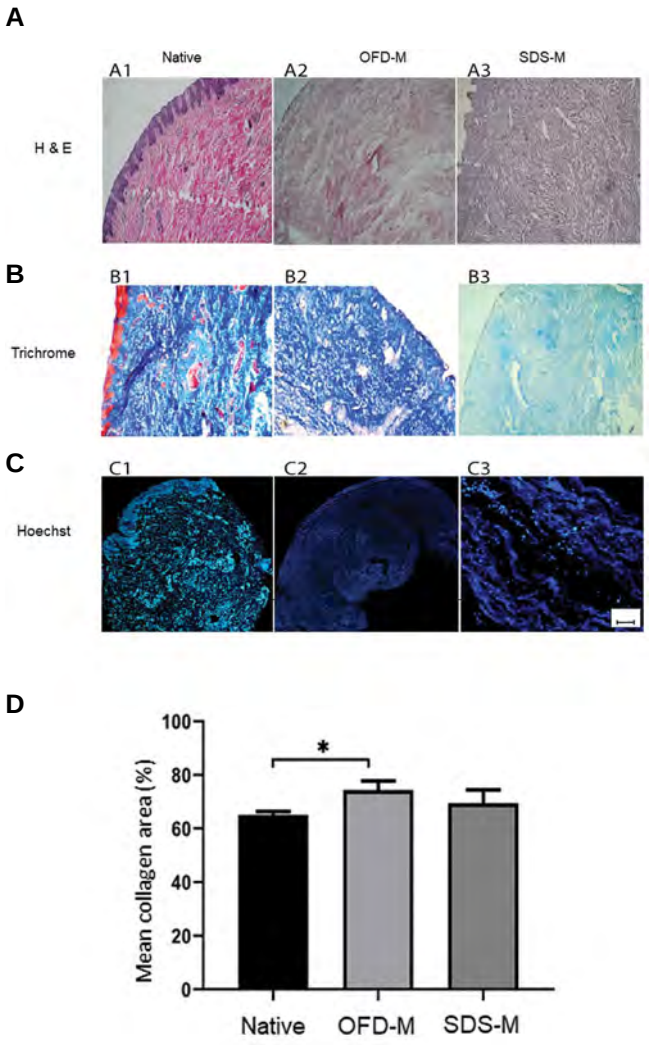

Fig.1: Histological staining of FAMs shows the effectiveness of the OFD-M in comparison to the SDS-M. **A1.** H&E staining showed that both cells and the ECM are intact in native samples. **A2.** The OFD-FAM samples possessed a preserved ECM and lacked any residual cells. **A3.** Decellularized foreskin obtained by the SDS-M partially preserved the ECM and contained residual cells. **B1.** Masson Trichrome staining was used to identify changes in collagen intensity (blue staining) of the matrix in the native samples in comparison to the FAM obtained by the **B2.** OFD-M and the **B3.** SDS-M. **C1.** Hoechst staining of the native samples, where the fluorescent color indicates the location of cell nuclei. **C2.** The FAM prepared by the OFD-M did not contain cell nuclei and residual DNA, and **C3.** FAM obtained by the SDS-M contained fluorescent spots which shows residual DNA (scale bar: 100 µm). **D.** Shows the collagen content in the OFD-FAM compared to the SDS-FAM. The data from 4 independent experiments were semi-quantified by ImageJ (*; P≤0.05). FAM; Foreskin acellular matrix, OFD-M; optimized foreskin decellularization method, SDS-M; Sodium dodecyl sulfate method, H&E; Hematoxylin and Eosin, and ECM; Extracellular matrix.

The OFD-FAMs do not show cytotoxic activity against hucMSCs

A resazurin assay was used to evaluate the toxicity of FAMs for hucMSCs. This assay indicated that the time-dependent cell viability percentage of the FAMs obtained byt the SDS-M was significantly lower than the cell viability of FAMs obtained via the OFD-M, especially at 72 hours. Precisely, the viability percentages of the hucMSCs co-cultured with FAMs obtained by the OFD-M were 91.7% and 83.1% at 48 hours and 72 hours, respectively, whereas they were only 83.5% and 66.7% at 48 hours and 72 hours, respectively, in the hucMSCs co-cultured with FAMs obtained via the SDS-M. In addition, there was a statistically significant difference between both of the two FAM groups and the native tissue group (P≤0.001, Fig.3).

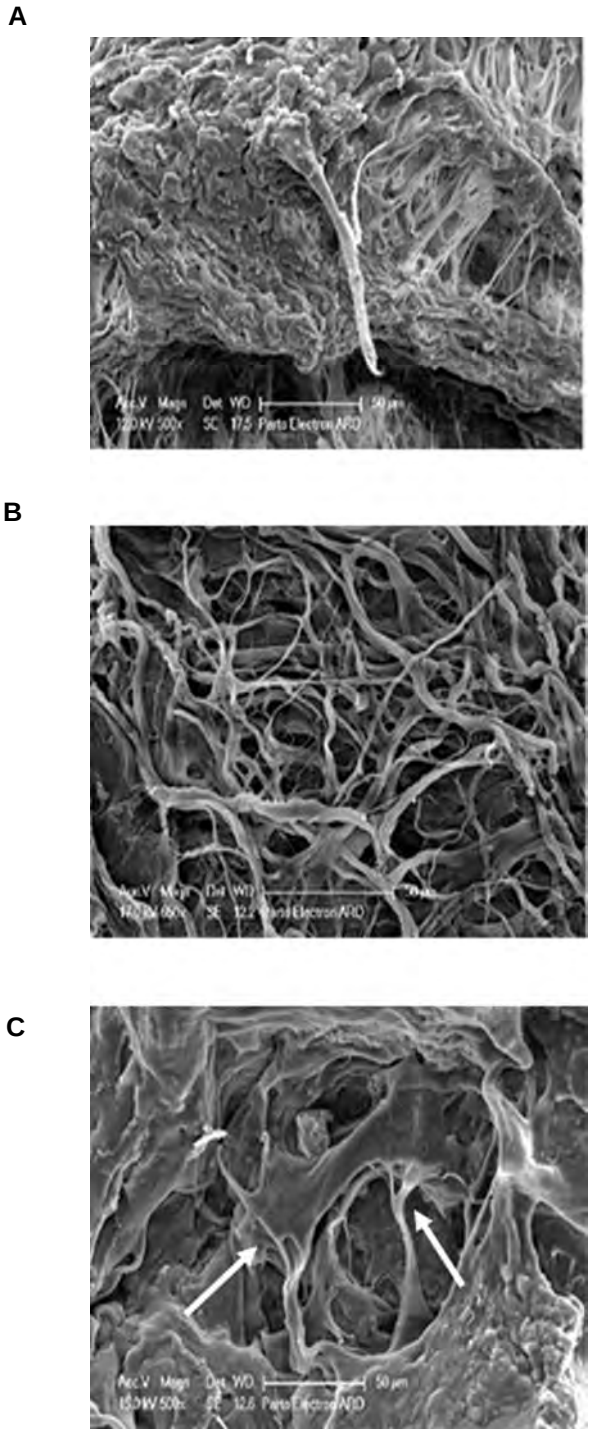

Fig.2: Comparison of the construction of natural and decellularized scaffolds by SEM analysis. **A.** Shows cellular ultrastructure in native tissues. **B.** FAMs obtained via the OFD-M did not contain any cells, and they exhibited an intact matrix and collagen structure. **C.** FAMs obtained via the SDS-M showed an irregular matrix structure. The presence of some cells is shown by arrows (500x, 650x). A representative of at least 3 independent experiments is shown (scale bar show 100 µm in all photos). SEM; Scanning electron microscope, FAM; Foreskin acellular matrix, OFD-M; Optimized foreskin decellularization method, and SDS-M; Sodium dodecyl sulfate method.

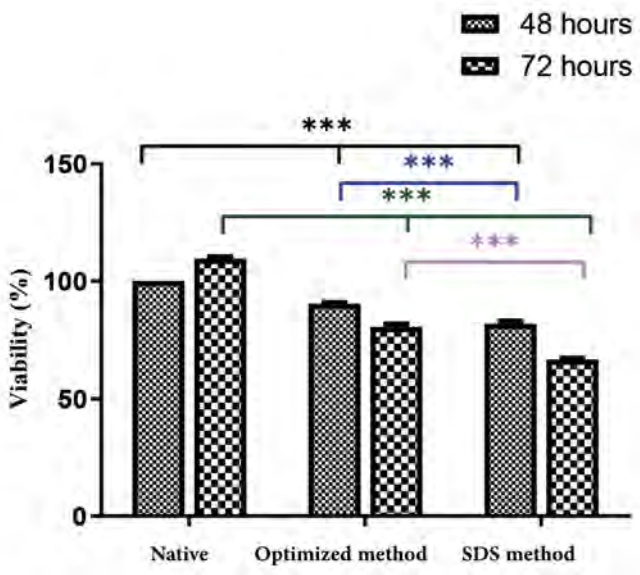

Fig.3: The OFD-M is biocompatible for hucMSCs. The time-dependent cell viability percentage in the FAMs obtained by the SDS-M was significantly lower than the FAMs obtained by the OFD-M (***; P≤0.001). OFD-FAMs showed similar behavior in terms of cell viability when compared to the native group. Pooled data are exhibited as the mean (± standard deviation, SD) of at least four independent experiments, each performed in triplicates. FAM; Foreskin acellular matrix, OFD-M; Optimized foreskin decellularization method, SDS-M; Sodium dodecyl sulfate method, and hucMSCs; Human umbilical cord mesenchymal stem cells.

Analysis of DNA ,SDS ,GAG ,and collagen content

In addition to histology outcomes, the DNA extraction experiments indicated that both the OFD-FAM group and the SDS-FAM group had less DNA than the native tissue. In particular, the DNA content was measured to be 1367 ng/µL in the native tissue, 338 ng/µL in SDS-FAMs, and 86 ng/µL in OFD-FAMs (Fig.4A). These results demonstrated that the OFD-FAMs had the least amount of residual DNA, which indicated that the decellularization processes was most effective in the OFD-M. Furthermore, the colorimetric assay revealed that the amount of residual SDS in the samples obtained via the SDS-M was approximately three folds higher than the OFD-FAMs (Fig.4B).

The remaining collagen and GAGs content were also quantified in both FAM groups. The collagenase assay indicated that the OFD-M approach resulted in the highest amount of collagen content per dry weight of tissue, in comparison to the SDS-M and the native tissue (Fig.4C). The GAG assay indicated that both methods decreased the GAG content in comparison to the native samples, however, the FAMs derived via the OFD-M retained significantly more ECM and GAGs than those perfused with the SDS-M (Fig.4D). These results indicate that the OFD-M is more appropriate for decellularization of foreskin since this method retained the highest amount of major ECM proteins.

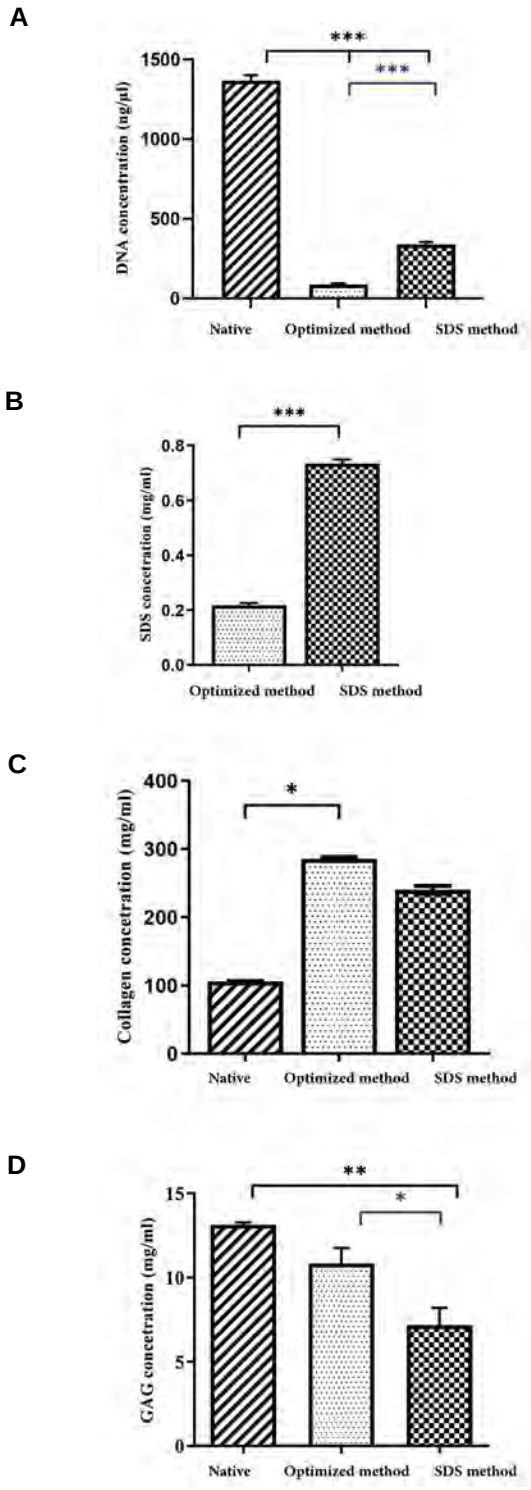

Fig.4: Comparison of the DNA, SDS, hydroxyproline and GAGs content of native tissue and FAM scaffolds. **A.** The DNA content was significantly reduced in the acellular scaffolds in comparison to the native samples. **B.** The content of residual SDS was significantly lower in the OFD-FAM group in comparison to the SDS-FAM group. **C.** A comparison of collagen concentration in the native tissue with the decellularized tissues showed that the FAMs contain a higher concentration of collagen, especially FAMs derived via the OFD-M. **D.** The content of GAGs in the native group compared to the two FAM groups showed that GAGs content was preserved during decellularization. The native foreskin was included as a control. Data with *P≤0.03, **P≤0.002, and ***P≤0.003 were statistically different according to one-way ANOVA and post hoc testing (Tukey's procedure). Pooled data are exhibited as the mean (± standard deviation, SD) of at least four independent experiments, each performed in triplicates. SDS; Sodium dodecyl sulfate method, GAGs; Glycosaminoglycans, FAM; Foreskin acellular matrix, and OFD-M; Optimized foreskin decellularization method.

Mechanical properties of OFD-FAM

In addition to biological efficiency, it is essential for bioscaffolds to have suitable mechanical properties. To address this point, we measured the tensile strength of the samples using a tensile-test device. As shown in Table 1, our data suggested that the native tissue had the highest tensile strength (4.33 ± 0.19 MPa), followed by FAMs derived by the OFD-M (3.66 ± 0.15 MPa), and finally FAMs obtained via the SDS-M (3.21 ± 0.01 MPa). The differences observed between these groups were significant (P=0.002, Fig.S4, See Supplementary Online Information at www.celljournal.org).

Moreover, the experiments indicated that in terms of the stress-strain elongation properties, the OFD-FAMs was similar to the native group (Table 1). Furthermore, the yield strain was shown to be significantly increased in the OFD-FAMs (P=0.01), indicating that the tissue durability had decreased, while at the same time, the elasticity had increased, in comparison to the native tissue.

OFD-FAM recellularization with hucMSCs

It is worth noting that in the recellularization experiments, we did not use seeding or any other technique to deliver cells to the tissues. Rather, we simply placed the OFD-FAMs on top of the cultured hucMSCs for eight days. Interestingly, we observed that hucMSCs were significantly more distributed on the FAMs obtained via the OFD-M compared to the FAMs obtained via the SDS-M. In addition, SEM images demonstrated the adherence of hucMSCs to the FAM surface (Fig.5).

Table 1: Mechanical properties of FAMs obtained by the two methods

	Modulus (Mpa)	Yield stress (Mpa)	Elastic strain	Ultimate tensile strength (Mpa)	Yield strain
Native	11.78 ± 0.68	4.06 ± 0.15	0.34 ± 0.01	4.33 ± 0.19	0.35 ± 0.02
OFD-M	9.66 0.29	3.7 ± 0.2	0.36 ± 0.02	3.66 ± 0.15	0.41 ± 0.02
	P value*: 0.002	P value*: NS#	P value*: NS	P value*: 0.002	P value*: 0.01
SDS-M	9.01 ± 0.01	3.2 ± 0.1	0.34 ± 0.01	3.21 ± 0.01	0.34 ± 0.01
	P value**: 0.0006	P value**: 0.001	P value**: NS	P value**: 0.0002	P value**: NS

FAM; Foreskin acellular matrix, OFD-M; Optimized foreskin decellularization method, SDS-M; Sodium dodecyl sulfate method, Native vs. OFD*; Native vs. SDS**, NS#; Not significant.

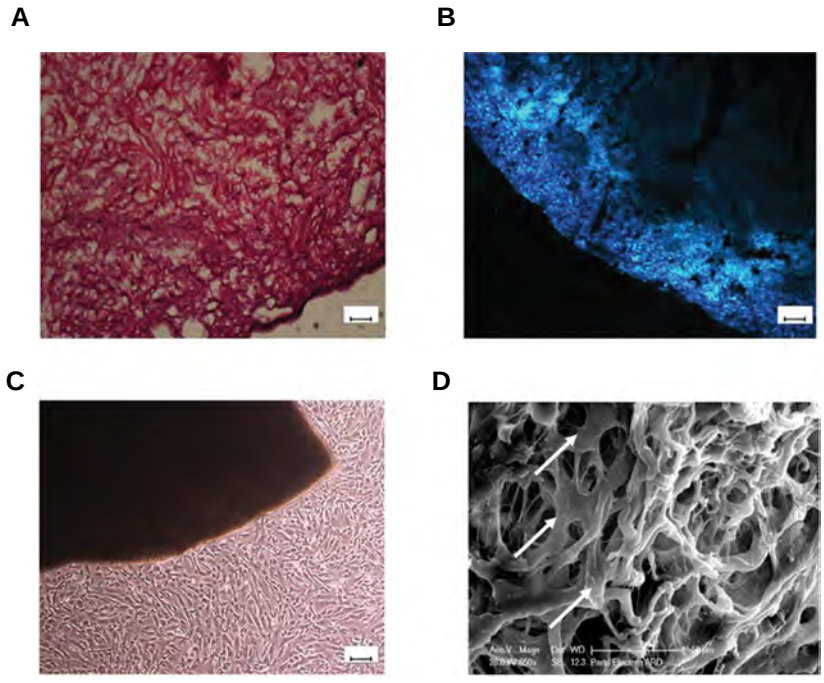

Fig.5: Recellularization of OFD-FAMs on day 8. **A.** H&E staining showed the number of migrated hucMSCs to the acellular scaffold (scale bar: 50 µm). **B.** The presence of cells was also confirmed using nuclear staining by Hoechst (scale bar: 50 µm). **C.** Growth and adherence of hucMSCs to FAMs (scale bar: 100 µm). **D.** SEM images of recellularized FAM on day 8 (650x) (cells are shown by arrows). A representative of at least 3 independent experiments is shown (scale bar: 50 µm).

Discussion

Natural biological scaffolds are commonly used in tissue engineering applications since they are biocompatible and mimic the native cellular microenvironment (20).

However, developing an optimal procedure for removing as much cell debris as possible from the tissue without compromising the structural and mechanical integrity of the ECM remains a challenge. Depending on the process of decellularization, the scaffold will have different properties. Therefore, all of these considerations should be carefully evaluated for designing decellularized scaffolds that are appropriate for tissue-specific stem cell applications (3). In the current study, an effective method for decellularization of the human foreskin was developed so that the resulting bioscaffold could be used as a potential therapy source in skin grafts for small wounds.

Continuous innovations in regenerative medicine have led to the development of various commercially available biological and synthetic substitutes for the reconstruction of skin defects caused by burns, chronic ulcers, and other types of damage (21). In some countries, including Iran, circumcision is a common practice, and the foreskin is considered a wasted tissue (22). The importance of repurposing this wasted tissue as a biological scaffold is compounded by the fact that it possesses components that are anatomically and structurally similar to skin (12). Furthermore, thicker skin grafts contain undesired hair follicles, eventually leading to hair growth in the graft (23). In contrast, the foreskin does not have any hair follicles, and so it has the potential to substitute for small injuries as a skin scaffold while alleviating this problem.

Here we compared two decellularization techniques: the so-called SDS-M and an OFD-M developed in this work to obtain a better scaffold. Other methods of skin decellularization have been reported in the literature (12, 24), and each protocol aims to remove the cells while maintaining the ECM components and the three-dimensional structure of the ECM (25). SDS is a popular detergent for tissue decellularization, which can solubilize both nuclear and cytoplasmic membranes efficiently. It can be considered a standard treatment for complete cell removal and approximately 90% of host DNA in several tissues (26). Treatment with SDS can disrupt protein-protein interactions and lead to protein denaturation, so choosing an optimal concentration of SDS and a suitable exposure time is crucial. In the present study, we developed an OFD-M for decellularization, which used 5% SDS over a limited period of time (6 hours) with Triton X100 and EDTA. This method was found to result in less disruption to the ECM and also better biological activity and cell removal in comparison to the SDS-M, which uses just 1% SDS for about 72 hours.

The FAM samples were evaluated using histology, residual DNA, GAGs, collagen content, cell biocompatibility, and tensile properties. Histological analysis and Hoechst staining showed that the cells were more completely removed in the OFD-FAM group compared to the SDS-FAM group. The findings were supported by H&E results, which revealed a trend that was similar to Hoechst staining. Furthermore, DNA extraction experiments showed that the DNA content was significantly reduced in the OFD-FAM group, compared to the native foreskin tissue.

The extent of disruption to the ECM was also evaluated with the aid of GAG and collagen assays. GAGs play a crucial role in survival, proliferation, differentiation, adhesion, and migration of the cells, so any decrease in GAG content will affect the tissue structure (18). The results of a recent study on decellularization of porcine livers showed that the amount of remaining collagen and GAGs in scaffolds varies, depending on the decellularization method. In particular, scaffolds perfused with Triton-SDS and sodium deoxycholate-SDS were found to retain more ECM and its associated compounds, including total collagen and GAGs, than those perfused with SDS only (27). Our results on human foreskin scaffolds support the findings of those studies. Moreover, collagen content was also quantified in this study using a hydroxyproline assay, to ensure that the decellularization process did not decrease the collagen content (28). As verified by other studies, the increased amount of collagen found in scaffold samples could be attributed to a decrease in sample mass due to the decellularization process (29).

Importantly, our findings indicated that GAG and collagen content in OFD-FAMs were more conserved than in the SDS-FAMs. These results were supported by Masson's trichrome staining (12), which showed that the preserved collagen network in the ECM of the OFD-FAMs was more structurally stable than that in the SDS-FAMs. These findings were substantiated by SEM analysis as well, which revealed that the three-dimensional structures and suitable porosity were well preserved only in the FAMs obtained by the OFD-method. The mechanical resistance of the scaffolds provided useful information regarding its structural integrity under an applied force. The results of the tensile test experiments indicated that during the decellularization process, the scaffold's mechanical strength was preserved.

Conclusion

In this study we have optimized the decellularization process for foreskin and have extensively and effectively removed the cells, while preserving GAG, collagen contents, and the ECM structure. Knowing that MSCs play a crucial role in wound healing, by utilizing these cells in our study, we have introduced a new approach to regenerative medicine. Importantly, hucMSCs were found to be well distributed on the OFD-FAM scaffolds after eight days of co-culture, and the cell viability of the co-culture remained high over the time of the experiment. The results of this study showed that the acellular scaffold obtained from human foreskin has appropriate mechanical properties and structural integrity for use in regenerative medicine, and in particular, for the

reconstruction of human foreskin. Importantly, one of the benefits of using FAM is that it is widely available and is considered a waste tissue after circumcision. In the current study, we found that the structural integrity of the ECM, the major ECM components such as collagen and GAGs, and the mechanical properties of the foreskin are well maintained after the decellularization process, opening up the possibility that FAMs may be well suited for several applications in regenerative medicine, including the treatment of small chronic wounds such as diabetic foot ulcers.

Acknowledgments

This study was funded by a research grant (IR.MUK.1397.220) from Kurdistan University of Medical Sciences (KUMS). There is no conflict of interest in this study.

Authors' Contributions

S.R.; Carried out the experiments and wrote the first draft of the manuscript. M.B.D.; Conceived and planned the experiments and directed the project. A.J.; Supervised the project and performed the first round of editing on the manuscript. M.P.; Performed the final editing, rewriting of the manuscript and data analysis. All authors read and approved the final manuscript.

References

1. Debels H, Hamdi M, Abberton K, Morrison W. Dermal matrices and bioengineered skin substitutes: a critical review of current options. Plast Reconstr Surg Glob Open. 2015; 3(1): e284.
2. Cazzell S, Moyer PM, Samsell B, Dorsch K, McLean J, Moore MA. A prospective, multicenter, single-arm clinical trial for treatment of complex diabetic foot ulcers with deep exposure using acellular dermal matrix. Adv Skin Wound Care. 2019; 32(9): 409-415.
3. Rana D, Zreiqat H, Benkirane-Jessel N, Ramakrishna S, Ramalingam M. Development of decellularized scaffolds for stem cell-driven tissue engineering. J Tissue Eng Regen Med. 2017; 11(4): 942-965.
4. Begum T, Farrelly PJ,Craigie RJ. Non-cross-linked porcine acellular dermal matrix (Strattice Tissue Matrix) in pediatric reconstructive surgery. J Pediatr Surg. 2016; 51(3): 461-464.
5. Lai C, Song G, Zhao B, Wang H, Pan B, Guo X, et al. Preparation and characterization of human scar acellular dermal matrix. J Biomater Sci Polym Ed. 2019; 30(9): 769-784.
6. Rozario T, DeSimone DW. The extracellular matrix in development and morphogenesis: a dynamic view. Dev Biol. 2010; 341(1): 126-140.
7. Salbach J, Rachner TD, Rauner M, Hempel U, Anderegg U, Franz S, et al. Regenerative potential of glycosaminoglycans for skin and bone. J Mol Med (Berl). 2012; 90(6): 625-635.
8. Heirani-Tabasi A, Hassanzadeh M, Hemmati-Sadeghi S, Shahriyari M, Raeesolmohaddeseen M. Mesenchymal stem cells; defining the future of regenerative medicine. Journal of Genes and Cells. 2015; 1(2): 34-39.
9. Shojaei F, Rahmati S, Banitalebi Dehkordi M. A review on different methods to increase the efficiency of mesenchymal stem cell-based wound therapy. Wound Repair Regen. 2019; 27(6): 661-671.
10. Azzopardi JI, Blundell R. Umbilical Cord Stem Cells. Stem Cell Discovery. 2018; 8: 1-11.
11. Duscher D, Barrera J, Wong VW, Maan ZN, Whittam AJ, Januszyk M, et al. Stem cells in wound healing: the future of regenerative medicine? A mini-review. Gerontology. 2016; 62(2): 216-225.
12. Purpura V, Bondioli E, Cunningham EJ, De Luca G, Capirossi D, Nigrisoli E, et al. The development of a decellularized extracellular matrix–based biomaterial scaffold derived from human foreskin for the purpose of foreskin reconstruction in circumcised males. J Tissue Eng. 2018; 9: 2041731418812613.
13. Young DA, Ibrahim DO, Hu D, Christman KL. Injectable hydrogel scaffold from decellularized human lipoaspirate. Acta Biomater. 2011; 7(3): 1040-1049.
14. Kajbafzadeh AM, Abbasioun R, Sabetkish S, Sabetkish N, Rahmani P, Tavakkolitabassi K, et al. Future prospects for human tissue engineered urethra transplantation: Decellularization and recellularization-based urethra regeneration. Ann Biomed Eng. 2017; 45(7): 1795-1806.
15. Alizadeh M, Rezakhani L, Soleimannejad M, Sharifi E, Anjomshoa M, Alizadeh A. Evaluation of vacuum washing in the removal of SDS from decellularized bovine pericardium: method and device description. Heliyon. 2019; 5(8): e02253.
16. Luna LG. Manual of histologic staining methods of the Armed Forces Institute of Pathology. 3rd ed. New York: Blakiston Division, McGraw-Hill; 1968.
17. Martinello T, Pascoli F, Caporale G, Perazzi A, Iacopetti I, Patruno M. Might the Masson trichrome stain be considered a useful method for categorizing experimental tendon lesions. Histol Histopathol. 2015; 30(8): 963-969.
18. Ferdowsi Khosroshahi A, Soleimani Rad J, Kheirjou R, Roshangar B, Rashtbar M, Salehi R, et al. Adipose tissue-derived stem cells upon decellularized ovine small intestine submucosa for tissue regeneration: An optimization and comparison method. J Cell Physiol. 2020; 235(2): 1556-1567.
19. Kajbafzadeh AM, Masoumi A, Hosseini M, Borjian MA, Akbarzadeh A, Mohseni MJ. Sheep colon acellular matrix: immunohistologic, biomechanical, scanning electron microscopic evaluation and collagen quantification. J Biosci Bioeng. 2014; 117(2): 236-241.
20. Qiu YL, Chen X, Hou YL, Hou YJ, Tian SB, Chen YH, et al. Characterization of different biodegradable scaffolds in tissue engineering. Mol Med Rep. 2019; 19(5): 4043-4056.
21. Powers JG, Higham C, Broussard K, Phillips TJ. Wound healing and treating wounds: chronic wound care and management. J Am Acad Dermatol. 2016; 74(4): 607-625.
22. Frisch M, Earp BD. Circumcision of male infants and children as a public health measure in developed countries: a critical assessment of recent evidence. Glob Public Health. 2018; 13(5): 626-641.
23. Shimizu R, Kishi K. Skin graft. Plast Surg Int. 2012; 2012: 563493.
24. Cui H, Chai Y, Yu Y. Progress in developing decellularized bioscaffolds for enhancing skin construction. J Biomed Mater Res A. 2019; 107(8): 1849-1859.
25. Crapo PM, Gilbert TW, Badylak SF. An overview of tissue and whole organ decellularization processes. Biomaterials. 2011; 32(12): 3233-3243.
26. Gilpin A, Yang Y. Decellularization strategies for regenerative medicine: from processing techniques to applications. Biomed Res Int. 2017; 2017: 9831534.
27. Wu Q, Bao J, Zhou Yj, Wang Yj, Du Zg, Shi Yj, et al. Optimizing perfusion-decellularization methods of porcine livers for clinical-scale whole-organ bioengineering. Biomed Res Int. 2015; 2015: 785474.
28. Lynch AP, Ahearne M. Strategies for developing decellularized corneal scaffolds. Exp Eye Res. 2013; 108: 42-47.
29. Luo J, Korossis SA, Wilshaw SP, Jennings LM, Fisher J, Ingham E. Development and characterization of acellular porcine pulmonary valve scaffolds for tissue engineering. Tissue Eng Part A. 2014; 20(21-22): 2963-2974.

Original Article

Modified Bismuth Nanoparticles: A New Targeted Nanoprobe for Computed Tomography Imaging of Cancer

Milad Mohammadi, M.Sc.[1], Sara Khademi, Ph.D.[2], Yazdan Choghazardi, Ph.D.[3], Rasoul Irajirad, Ph.D.[4], Mohammad Keshtkar, Ph.D.[5*], Alireza Montazerabadi, Ph.D.[1*]

1. Medical Physics Research Center, Mashhad University of Medical Sciences, Mashhad, Iran
2. Department of Radiology Technology, School of Paramedical Sciences, Mashhad University of Medical Sciences, Mashhad, Iran
3. Department of Medical Physics, Faculty of Medicine, Isfahan University of Medical Sciences, Isfahan, Iran
4. Department of Medical Physics, School of Medicine, Iran University of Medical Sciences, Tehran, Iran
5. Medical Physics and Radiology Department, Faculty of Medicine, Gonabad University of Medical Sciences, Gonabad, Iran

Corresponding Addresses: P.O.Box: 9691983879, Medical Physics and Radiology Department, Faculty of Medicine, Gonabad University of Medical Sciences, Gonabad, Iran
P.O.Box: 9177948564, Medical Physics Research Center, Mashhad University of Medical Sciences, Mashhad, Iran
Emails: keshtkar.dmohammad@yahoo.com, montazerabadia@mums.ac.i

Received: 14/November/2021, Accepted: 08/March/2022

Abstract

Objective: Recently, development of multifunctional contrast agent for effective targeted molecular computed tomography (CT) imaging of cancer cells stays a major problem. In this study, we explain the ability of Triptorelin peptide-targeted multifunctional bismuth nanoparticles (Bi2S3@ BSA-Triptorelin NPs) for molecular CT imaging.

Materials and Methods: In this experimental study, the formed nanocomplex of Bi2S3@ BSA-Triptorelin NPs was characterized using different methods. The MTT cytotoxicity test was performed to determine the appropriate concentration of nanoparticles in the MCF-7 cells. The X-ray attenuation intensity and Contrast to Noise Ratio (CNR) of targeted and non-targeted nanoparticles were measured at the concentrations of 25, 50, and 75 µg/ml and X-ray tube voltages of 90, 120 and 140 kVp.

Results: We showed that the formed Bi2S3@ BSA-Triptorelin NPs with a Bi core size of approximately ~8.6 nm are nontoxic in a given concentration (0-200 µg/ml). At 90, 120, and 140 tube potentials (kVp), the X-ray attenuation of targeted cells were 1.35, 1.36, and 1.33-times, respectively, more than non-targeted MCF-7cells at the concentration of 75 µg/ml. The CNR values at 90, 120, and 140 kVp tube potentials were 171.5, 153.8 and 146.3 c/σ, respectively.

Conclusion: These findings propose that the diagnostic nanocomplex of Bi2S3@ BSA-Triptorelin NPs can be applied as a good contrast medium for molecular CT techniques.

Keywords: CT Contrast Agents, Molecular Imaging, Targeted Imaging, Triptorelin

Cell Journal(Yakhteh), Vol 24, No 9, September 2022, Pages: 515-521

Citation: **Mohammadi M, Khademi S, Choghazardi Y, Irajirad R, Keshtkar M, Montazerabadi A. Modified bismuth nanoparticles: a new targeted nanoprobe for computed tomography imaging of cancer. Cell J. 2022; 24(9): 515-521. doi: 10.22074/cellj.2022.8348.**

Introduction

Molecular imaging involves the visualization, diagnosis, and quantification of physiological and pathological processes of the body at the cellular and/or molecular level. The biochemical markers and/or other markers molecules provide this aim (1). Either alone or in the combination with imaging agents can image the tissue state. Today, a computed tomography (CT) imaging, a relatively inexpensive, high-resolution method, is used in 75% of all of clinical diagnostic imaging. CT imaging shows higher resolution of spatial and temporal (2), but is less sensitive than other clinical imaging modalities (3). To date small iodine-based molecular compounds used, such as Visipaque, show various disadvantages, including toxicity of renal, short half-lives, and absence of specificity (4, 5). To improve the sensitivity of the images, the new contrast media should include the following properties: surface chemical modification, high atomic number, sufficient concentration, size control, biocompatible and be targeted (4, 6).

Bismuth (atomic number of 83 and k-edge=90.5 KeV) may be a potential candidate to be a contrast enhancer in CT imaging (7). Especially compared to conventional iodine contrast agents, Bi2S3 offers several favorable features, including cost-effective, long half-lives, and capability to embrace functional surface changes (5, 8). Molecular imaging largely depends on the development of specificity and sensitivity of imaging agents (9). Targeting agents such as small molecules, peptides, antibodies, and aptamers (10) are used to label imaging agents as a ligand detector (11). Compared to small molecules, peptides have many advantages, such as good selectivity and specificity, and easy formulation that do not require any binding properties alteration. In addition, peptides are more stable than antibodies at the room temperature and have less immunogenicity than antibodies (10). The gonadotropin-releasing hormone (GnRH), as well called as hypothalamic luteinizing hormone-releasing hormone (LHRH) been proposed as targets for targeted cancer treatment (12). The LHRH is a decapeptide hormone with the primary sequence pGlu-His-Trp-Ser-Tyr-Gly-Leu-Arg-Pro-Gly-NH_2 that secretes from the hypothalamus.

LHRH can bind specifically to Luteinizing Hormone Releasing Hormone Receptor (LHRH-R) at the surface of gonadotropin cells in the pituitary gland and stimulate the synthesis and release of luteinizing hormone (LH) and follicle-stimulating hormone (FSH) (13).

Some tumors express LHRH receptors on their surfaces, like breast, ovary, prostate (14, 15). Therefore, the presence of specific sites for the binding of LHRHs on the membrane of cancer cells provides the conditions for the binding of LHRH as well as its analogues, which also have a high affinity for these cells (16). On the other hand, due to the limited expression of these receptors in normal tissues, it can be used for targeted drug delivery, such as an imaging agent or therapy for LHRH-R^+ tumors (containing hormone receptors). In some cases, LHRH antibodies or peptides that bind to LHRH-R are used to deliver contrast agents in various imaging modalities such as ultrasound, MRI, PET, and SPECT to the expressing LHRH-R cells (17). Triptorelin is a deca peptide with the pGlu-His-Trp-Ser-Tyr-D-Trp-Leu-Arg-Pro-Gly-NH_2 sequence that has a molecular weight of 1311.4 g/mol (13, 18). Receptors are detected by these hormonal peptides, so they can be internalized after binding to their ligands (19). In this study, we synthesized and evaluated the cytocompatibility of the multifunctional Triptorelin peptide conjugated bismuth nanoparticles (Bi2S3@ BSA-Triptorelin NPs). Furthermore, the synthesis of Bi2S3 @ BSA with and without targeting molecule (Triptorelin) was measured for molecular CT technique at various concentrations NPs, and X-ray tube voltages.

Material and Method

This study was approved by the Ethical Research Commitee of Mashhad University of Medical Sciences (IR.MUMS.MEDICAL.REC.1398.557).

Preparation of Bi2S3 @ BSA nanoparticles

Briefly, under stirring, aqueous Bi $(NO_3)3$ (248592, Sigma Aldrich, USA) (2.8 mL in 3 M HNO_3 solution (438073, Sigma Aldrich, USA), 25 mM, 25°C) was added into the BSA solution (40 mL, 66 mg/mL) (810533, Sigma Aldrich, USA) at 25°C temperature. Adding bismuth solution should not take more than 2 minutes. Then, add 6 ml of sodium hydroxide solution (5 M) (S8045, Sigma Aldrich, USA) at once to the above solution. Eventually the color of the solution starts to modify from yellow to brown, and after that to dark black for 10 minutes. The mixture was set aside for another 12 hours to complete the reaction without rotation. All synthesis steps were performed at room temperature. Finally, the product was centrifuged at 12,000 rpm for 15 minutes, reaching a volume of 2.5 cc, and finally dialyzed for 48 hours (20).

Binding of Triptorelin peptide to nanoparticles

1 ml of the above final product was magnetically stirred to a pH of 6.5, then 0.5 mg of peptide was added, and finally 0.15 mg of N-(3-dimethylaminopropyl)-N-ethylcarbodiimide hydrochloride (EDC) (8.51007, Sigma-Aldrich, USA) and 0.09 mg of the N-Hydroxysuccinimide (NHS) (130672, Sigma-Aldrich, USA) was added. The reaction was stirred for 1 hour at room temperature. The final product was dialyzed for 24 hours in refrigerator to obtain Bi2S3@BSA-Triptorelin NPs.

Characterization techniques

Morphology and size distribution of nanoparticles were evaluated using transmission electron microscope (TEM) (Gatan model 791, Philips CM 12, Poland) and image J, respectively. X-ray Diffraction (XRD) patterns of dried nanoparticle powders were analyzed through the GNR EXPLORER (XRD) X-ray diffraction gauge with a wavelength of 1.54 Å K_a lines. Fourier Transform Infrared (FTIR) spectra were evaluated using an infrared spectrometer Red (AVATAR 370, Thermo Nicolet AVATAR 370 FTIR, USA). The surface charge of nanoparticles and the hydrodynamic size of nanoparticles were measured by a device (SZ100, HORIBA, Japan). The contents of bismuth in the samples were measured using Inductively Coupled Plasma - Optical Emission Spectrometry (ICP-OES) (VISTA-MPX, Varian Inc., USA).

Stability of Bi2S3@BSA-Triptorelin NPs

The stability of Bi2S3@BSA-Triptorelin NPs was evaluated using DLS analysis. 100 µl of Bi2S3@ BSA-Triptorelin NPs was added to 500 µl of 10% FBS (16000044, GIBCO, USA) culture medium. After 24 hours, the hydrodynamic size of nanoparticles was assessed from the obtained solution. The result was compared with the hydrodynamic size obtained from the DLS test of Bi2S3@BSA-Triptorelin nanoparticles.

X-ray attenuation measurements of Bi2S3@BSA-Triptorelin NPs versus Visipaque

The X-ray attenuation intensity of Bi2S3 @ BSA Triptorelin NPs was compared with CT contrast agent based on iodine Visipaque (320 mg/ml), (544031, GE Healthcare, Ireland). Different concentrations (500-3000 µg/ml) of the mentioned materials were prepared in the 200 µl microtubes and placed in a polymethylmethacrylate (PMMA) phantom (Iran). CT imaging was performed through clinical CT modality (Neusoft) with the parameters of: 1. tube voltages: 90, 120, and 140 kVp, 2. tube current: 250 mA, 3. exposure time: 1000 milliseconds, 5. thickness cutting: 1 mm, 6. Scanning Field of View (SFOV): 250×250 mm, 7. pitch: 1. The attenuation intensity was done in the region of interest (ROI) of the acquired images.

Cell culture

Human breast cancer cells (MCF-7) were cultured in RPMI 1640 medium (51800-035., GIBCO, USA) with 10% FBS and 1% penicillin-streptomycin (P4333, Sigma Aldrich, USA). The MCF-7 cells were incubated in 37°C, 5% CO_2 for 24 hours.

Cytotoxicity test

MTT method was used to estimate the cytotoxicity

of Bi2S3 @ BSA-Triptorelin and Bi2S3 @ BSA NPs at concentrations of 0-200 µg/ml ranges. Subsequently, 10^4 MCF-7 cells per well were seeded for 24 hours incubation under 37°C and 5% CO_2. Then, the each wells medium was replaced with fresh medium of Bi2S3 @ BSA-Triptorelin and Bi2S3 @ BSA with various concentrations from 0-200 µg/ml of nanoparticles. After 24 hours, an appropriate concentration of MTT solution (10 µl of MTT solution per 100 µl) was added to each sample and incubated for 4 hours. Then the medium was removed attentively and added 100 µl of dimethyl sulfoxide (DMSO, D2650, Sigma Aldrich, USA). The absorbance of each well was measured through a microplate absorbance reader (Stat Fax 2300, USA) at 570 nm.

In vitro CT imaging of MCF-7 cancer cells

MCF-7 cells were seeded in the 6-well plates with a density of 5×10^5 cells per each well. After that, MCF7 cells were incubated with Bi2S3 @ BSA Triptorelin and Bi2S3 @ BSA NPs at a concentration of 0-75 µg/ml range. The cells were washed 3 times with PBS and then trypsinized. The trypsinized cells were centrifuged and the cell suspension supernatant was removed from the cell plaque. The remaining cells plaque was transferred to 200 µl microtubes and 0.4% agarose gel solution (A9539, Sigma Aldrich, USA) was added on the cell plate to fix the cells. The microtubes were placed in phantom cavities for imaging. The CT values (HU) were caught at the similar workstation through software provided through the manufacturer. The contrast-to-noise ratio (CNR) was obtained using the Hounsfield unit (HU), which is recorded by an analysis that draws a ROI on the chosen image. The CNR was measured as equation (1).

Equation (1): $CNR=(x_S-x_{BG})/\sigma_{BG}$

Among them, X_S and X_{BG} are the signal intensities derived in two different structures of interest in the same image. At the same time, σ_{BG} is the standard deviation of the background noise in the image. The workflow of this study is illustrated in Figure 1.

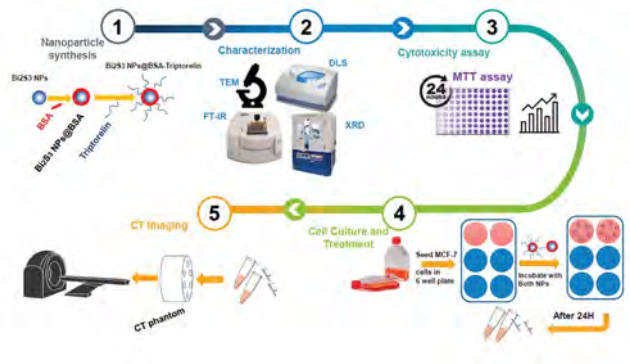

Fig.1: Work flow of this study.

Statistical analysis

Statistical analysis was done using SPSS software version 22 (IBM, USA). A one-way analysis of variance (ANOVA) was done to evaluate the statistically significant differences between the means of groups and the $P<0.05$ was assumed statistically significant.

Results

Synthesis and characterization of nanoparticles

Solutions of Bi2S3 @ BSA and Bi2S3 @ BSA-Triptorelin NPs were synthesized using the protocols described above. The size and morphology of the formed Bi2S3 @ BSA-Triptorelin NPs were determined using TEM (Fig.2).

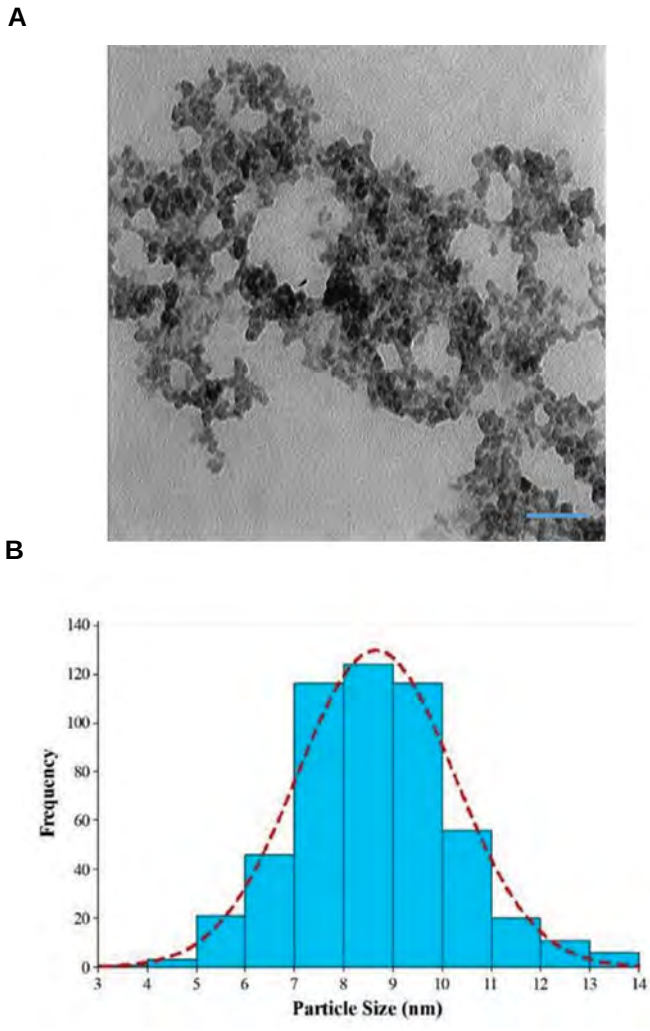

Fig.2: Characterization of targeted Bismuth nanoparticles. **A.** Transmission electron microscope (TEM) image (scale bar: 50 nm) and **B.** Size distributions of Bi2S3 @ BSA-Triptorelin NPs. NPs; Nanoparticles.

It may be noted that the formed Bi2S3 @ BSA-Triptorelin NPs have a circular shape with an average size of 8.6 ± 1.6 nm. The hydrodynamic size of Bi2S3 @ BSA and Bi2S3 @ BSA-Triptorelin NPs were measured by DLS at 14.8 nm and 17.1 nm, respectively (Fig.S1A, B, See Supplementary Online Information at www.celljournal.org). Furthermore,

the hydrodynamic size of Bi2S3@BSA-Triptorelin NPS showed good stability in the culture medium. It was 17.2 ± 1.1 nm after 24 hours incubation (Fig.S1C, See Supplementary Online Information at www.celljournal.org).

We observed that the surface potential of Bi2S3 @ BSA and Bi2S3 @ BSA-Triptorelin NPs were -77.8 mV and -84.7 mV, respectively (Fig.S2, See Supplementary Online Information at www.celljournal.org).

The Triptorelin binding to the bismuth sulfide nanoparticles was confirmed by comparing the FTIR spectra of Bi2S3 @ BSA-Triptorelin with Bi2S3 @ BSA NPs. As shown in the Figure 3, the formation of 1651 and 1576 peaks related to the Amide and Primary Amine bonds in the FTIR spectrum of non-peptide bismuth nanoparticles that indicates the BSA presence on the nanoparticles. On the other hand, the removal of the thiol peak of region 2360 is due to the complex formation of bismuth and thiol, which leads to the bismuth bonding with a sulfur that results in a sulfide bond. Also, 670 peak can be related to bismuth sulfide bond. The 3412 peak is related to N-H and O-H stretching vibration. Also, 2921 and 2847 peaks relate to the C-H stretching vibration. The FTIR spectrum of peptide nanoparticles shows that the peptide binds to the nanoparticle surface via an amide bond, which together with BSA-related amides appeared on the nanoparticle surface in 1651 peak. On the other hand, the presence of 702 peak indicates the bond of aromatic C-H, which is related to the aromatic ring of the Triptorelin peptide compound.

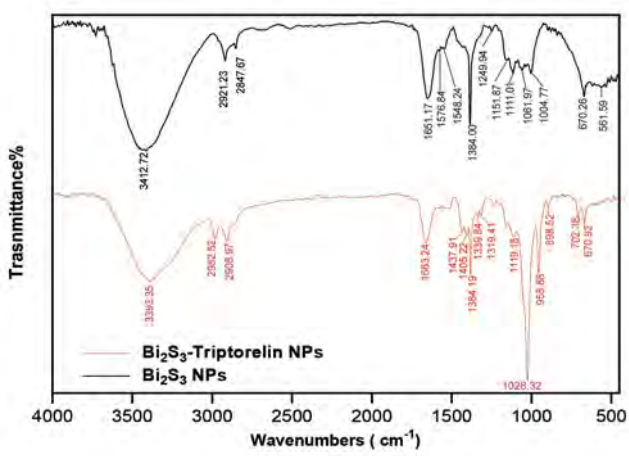

Fig.3: FTIR spectra of Bi2S3 @ BSA and Bi2S3 @ BSA-Triptorelin NPs; Nanoparticles.

The crystallographic structure of the synthesized nanoparticles was investigated by the XRD in the range of 80°-20°. For this purpose, the powder sample was tested. By adapting the diffraction pattern shown in the figure with the reference codes related to the crystal structures of different materials, it can be seen that this pattern is related to the Bi2S3 crystal structure with the reference code JCPDS No. 96-900-3474. The nanoparticles have an Orthorhombic crystal system with lattice constants a=11.345 Å, b=3.994 Å, c=11.193 (Fig.S3, See Supplementary Online Information at www.celljournal.org).

X-ray attenuation measurements of Bi2S3@BSA-Triptorelin nanoparticles versus Visipaque

X-ray attenuation properties of Bi2S3 @ BSA-Triptorelin were compared with an iodine-based small molecule contrast media (Visipaque) as a contrast media concentration function (iodine or bismuth) and X-ray tube potentials difference (Fig.4). As represented in Figure 4, the attenuation intensity of targeted NPs, and Visipaque are increased follow of materials concentration increasing at the different kVp. The X-ray attenuation of targeted nanoparticles versus Visipaque was 3.57 times at 90 kVp and 3000 µg/ml concentration.

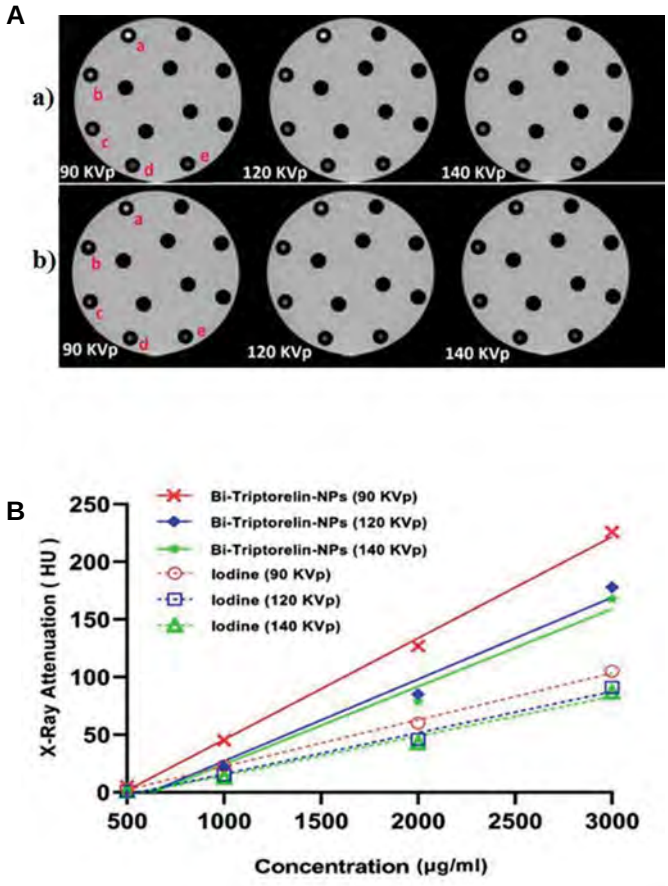

Fig.4: CT images and X-ray attenuations intensity of targeted Bismuth NPs and Visipaque at different concentrations and tube potentials. **A.** CT images of Bi2S3 @ BSA-Triptorelin NPs (a) and Visipaque (b) at different concentrations (a; 3000 (µg/ml), b; 2000 (µg/ml), c; 1000 (µg/ml), d; 500 (µg/ml), e; Deionized water) and tube voltages. **B.** Diagram of Attenuation X-ray intensity (HU) of Bi2S3 @ BSA-Triptorelin NPs and Visipaque at different tube potentials and concentrations. CT; Computed Tomography and NPs; Nanoparticles.

Cytocompatibility assays

We performed the MTT assay to evaluate the toxicity of Bi2S3 @ BSA-Triptorelin and Bi2S3 @ BSA nanoparticles in the MCF-7 cell line. Survival of the cells was measured at two groups of nanoparticles and a wide range of concentrations (0 to 200 µg/ml). The cell survival was decreased with increasing concentration in the both groups of bismuth nanoparticles (Fig. S4, See Supplementary Online Information at www.celljournal.org). Cytotoxicity was not significant in the

group of peptide-targeted nanoparticles and non-target nanoparticles up to 75 and 150 µg/ml, respectively, compared with the control group (P>0.05).

Targeted CT imaging of MCF-7 cells *in vitro*

In the next step, we investigated the possibility of using Bi2S3 @ BSA-Triptorelin for targeted cells imaging. Figure 5A shows an axial image of CT images of MCF-7 cells with bismuth nanoparticles with and without Triptorelin in different concentrations and kilo voltages (5). As shown in Figure 5B, at 90 kVp and 75 µg/ml, the X-ray attenuation intensity of cells in the presence of targeted nanoparticles is 1.4 times greater than cells in the presence of non-targeted nanoparticles.

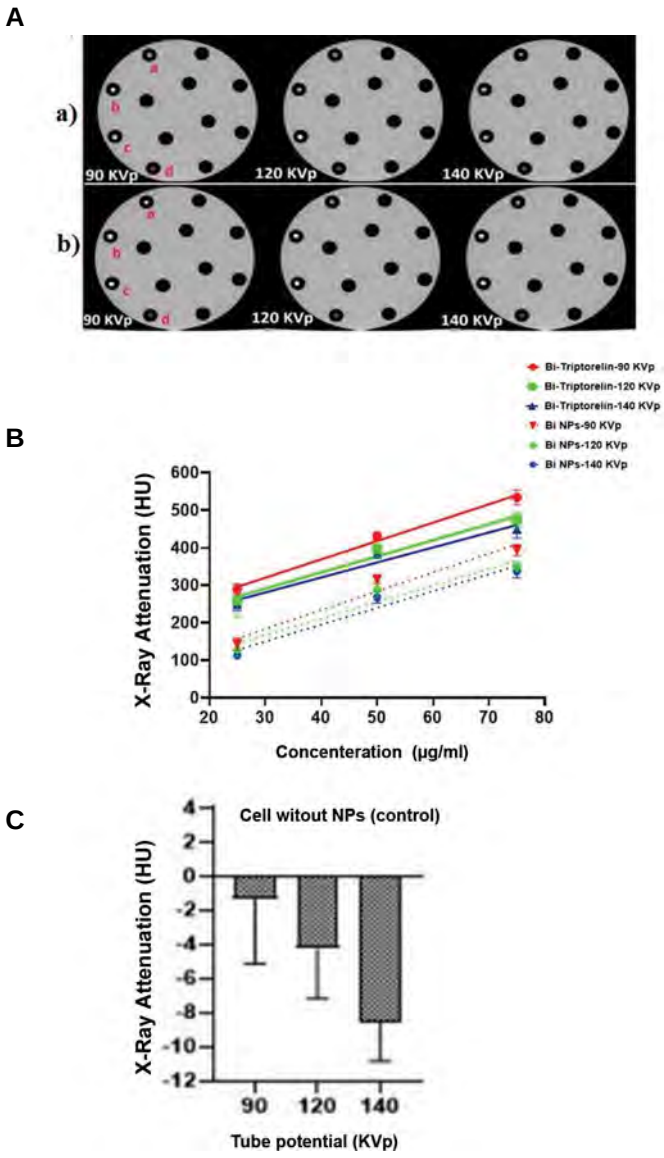

Fig.5: CT images and X-ray attenuation intensity of targeted and non-targeted bismuth nanoparticles at different concentrations and X-ray tube potential. **A.** Axial CT images of MCF-7 cells incubated with (a) Bi2S3@BSA and (b) Bi2S3@BSA-Triptorelin NPs at different concentrations [a; 25 (µg/ml), b; 50 (µg/ml), c; 75 (µg/ml), d; MCF-7 cells without presence of NPs]. **B.** Diagram of X-ray Attenuation intensity (HU) of Bi2S3@BSA and Bi2S3 @ BSA-Triptorelin NPs at different tube potentials and concentrations. **C.** Diagram of X-ray attenuation intensity of MCF-7 cells without NPs at different tube potentials. CT; Computed Tomography and NPs; Nanoparticles.

Investigation of contrast-to-noise ratio of nanoparticle-treated cells

Based on mentioned equation (1), the CNR of cells in the presence of targeted and non-targeted nanoparticles was calculated. The sample without the nanoparticles was considered as the background. At the different voltages, the amount of CNR was obtained according to the amount of attenuation and noise of cell images. The results are summed up in the Figure 6. The results show that the targeted bismuth nanoparticles have greater CNR versus the non-target nanoparticles at the same voltages and concentrations. At 90 kVp and 75 µg/ml concentration, the CNR value showed a 45 unit difference between targeted and non-target nanoparticles. The CNR value was decreased by increasing the tube potential and decreasing the concentration. At 90 kVp and 75 µg/ml, the CNR value of targeted cells is 1.4 times rather than non-targeted cells.

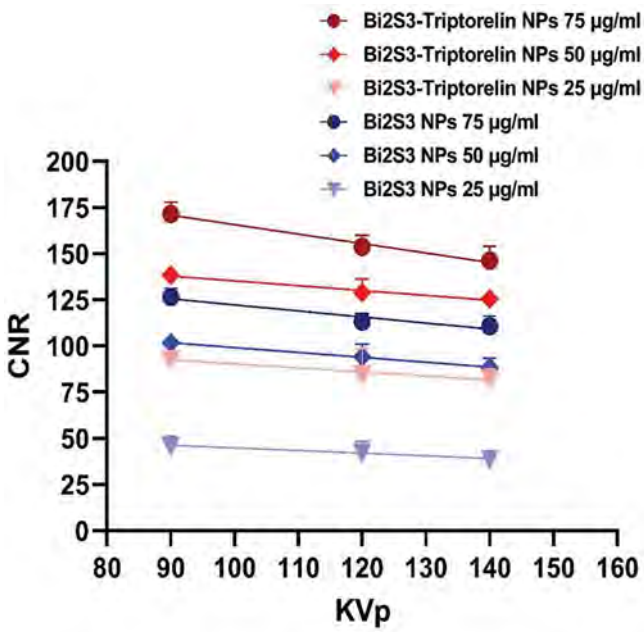

Fig.6: CNR obtained from CT images of cancer cells in the presence of targeted and non-targeted NPs. CNR; Contrast to Noise Ratio, CT; Computed Tomography, and NPs; Nanoparticles.

Discussion

The brightness of CT images and X-ray attenuation intensity were increased with increasing concentration of Bi2S3 @ BSA-Triptorelin NPs and iodine contrast agent. However, the CT values of Bi2S3 @ BSA-Triptorelin NPs was greater than Visipaque with the same concentration. For example, the X-ray attenuation of Bi2S3 @ BSA-Triptorelin was approximately 3.57 times greater than Visipaque at the concentration of 3000 µg/ml and 90 kVp. At 90 keV to 130 keV photon energy range, mass attenuation coefficient of bismuth is higher than Visipaque (22). Bi2S3 @ BSA has a greater attenuation intensity

coefficient than the low molecular weight iodine because of its much greater electron density and atomic number (1.69×10^{30} e/m^3 and 83) than those of iodine (2.34×10^{28} e/m^3 and 53), respectively.

We showed that the formed Bi2S3@ BSA-Triptorelin NPs with a Bi core size of ~8.6 nm are nontoxic in a certain concentration. It should be noted that the employee of Bi2S3 @ BSA-Triptorelin NPs as a contrast medium in a lower concentration and lower side effects has a good potential in the imaging. Ahamed et al. (23) calculated the toxicity of non-targeted Bi2O3 nanoparticles in the MCF-7 cell line. They showed a significant cytotoxicity at the 50 µg/ml concentration. However, at the concentrations above 50 µg/ml, their results indicated more cytotoxicity than our study. Dong et al. (24) evaluated the cytotoxicity of Bi2S3 @ BSA-FA nanoparticles at the concentration of 400 µg/ml on 4T1 cell line. Their results did not show any significant cytotoxicity. In our study, the cytotoxicity of Bi2S3 @ BSA-Triptorelin and Bi2S3 @ BSA NPs was not significant, up to 75 µg/ml and 150 µg/ml, respectively.

Based on several studies, the cytotoxicity of nanoparticles depends on many factors such as cell line type, nanoparticle type, coating, target agents of nanoparticles, and incubation time. Obviously, based on X-ray attenuation intensity, greater concentration leads to greater cellular uptake of both NPs. The CT values of targeted and non-targeted NPs in the MCF-7 cells were much higher than untreated control cells and there was a good statistically significant difference. The highest amount of HU value was related to the targeted bismuth nanoparticles at 90 kVp X-ray tube potential and the concentration of 75 µg/ml. At the same concentration and X-ray tube potential, the HU value of targeted nanoparticles was 1.4 and 398 times greater than the HU value of non-targeted bismuth nanoparticles and the cells without the presence of nanoparticles (control), respectively. Higher CT values of Bi2S3 @ BSA-Triptorelin compared to Bi2S3 @ BSA can be attributed to the targeting of nanoparticles by the Triptorelin peptide and their greater cell uptake via enhancement of internalization of Bi2S3@ BSA-Triptorelin NPs through GnRH receptors in the MCF-7 cells. In the X-ray imaging, this is hard to visually distinguish the brightness of cancer cells incubated with various concentrations of nanoparticles.

New CTs have a strength of 4096 tons of gray, which produces various densities in HU. But, the human eye cannot detect higher than 20 tons of gray in a CT image. Thus, a CT value is a smaller value representing the actual attenuation of an object's X-rays (HU), which is safer, more specific, and more accurate than an image. The CNR value or CT contrast enhancement of Bi2S3 @ BSA-Triptorelin was significantly higher than cells treated with non-target nanoparticles at the same concentration and tube potential. The results of CT contrast enhancement were related to the X-ray CT attenuation of the contrast media. The CNR value increased by increasing the concentrations of Bi, because of more atoms are existed for interaction at higher concentrations. The CNR value of Bi2S3 @ BSA-Triptorelin and Bi2S3 @ BSA NPs were decreased by increasing X-ray tube potential range from 90 to 140 kVp. It was in agreement with Algethami et al. (25) study. Our findings propose that Bi2S3 @ BSA-Triptorelin can be targeted MCF-7 cells for particular X-ray imaging utilizations.

Conclusion

We have provided an easy way to synthesize Bi2S3 @ BSA-Triptorelin for the targeted CT imaging. Our results indicated targeted NPs have a greater X-ray attenuation than non-targeted cells at the same concentration. Furthermore, targeted and non-targeted cells have a higher attenuation intensity rather than iodine contrast media (Visipaque). Our findings revealed that the attenuation intensity and CNR highly depend on the bismuth concentration and the tube potentials. Our findings indicated the Bi2S3 @ BSATriptorelin NPs can be applied as a contrast agent for molecular CT of breast cancer. In the future studies, the targeted NPs can be assessed in radiotherapy and *in vivo* study.

Acknowledgments

The authors gratefully acknowledge the Medical Physics Research Center, Mashhad University of Medical Sciences, Mashhad, Iran. This study was supported by a grant (No: 980650) from Mashhad University of Medical Sciences, Mashhad, Iran. The authors declare that they have no conflicts of interest in this study.

Authors' Contribution

A.M., S.Kh., M.K.; Contributed to conception and design. M.M., Y.Ch.; Contributed to all experimental work, data and statistical analysis, and interpretation of data. R.I.; Contributed to the synthesis of nanoparticles and interpretation of characterization nanoparticles data. A.M.; Drafted the manuscript. M.K., A.M.; Revised the manuscript. All authors read and approved the final manuscript.

References

1. MacRitchie N, Frleta-Gilchrist M, Sugiyama A, Lawton T, McInnes IB, Maffia P. Molecular imaging of inflammation-Current and emerging technologies for diagnosis and treatment. Pharmacol Ther. 2020; 211: 107550.
2. Cole LE, Ross RD, Tilley JM, Vargo-Gogola T, Roeder RK. Gold nanoparticles as contrast agents in x-ray imaging and computed tomography. Nanomedicine. 2015; 10(2): 321-341.
3. Goldman W. Principles of CT: radiation dose and image quality. J Nucl Med Technol. 2007; 35(4): 213-225.
4. Khademi S, Sarkar S, Shakeri-Zadeh A, Attaran N, Kharrazi S, Ay MR, et al. Folic acid-cysteamine modified gold nanoparticle as a nanoprobe for targeted computed tomography imaging of cancer cells. Mater Sci Eng C Mater Biol Appl. 2018; 89: 182-193.
5. Zhou D, Li C, He M, Ma M, Li P, Gong Y, et al. Folate-targeted perfluorohexane nanoparticles carrying bismuth sulfide for use in US/CT dual-mode imaging and synergistic high-intensity focused ultrasound ablation of cervical cancer. J Mater Chem B. 2016; 4(23): 4164-4181.
6. Zhu HL, Cheng QY, Liao MY, Zhang ZL, Cai WG, Ma JJ, et al. Economical synthesis of ultra-small Bi2S3 nanoparticles for high-sensitive CT imaging. Mater Res Express. 2019; 6(9): 095005.
7. Koç MM, Aslan N, Kao AP, Barber AH. Evaluation of X-ray tomog-

raphy contrast agents: a review of production, protocols, and biological applications. Microsc Res Tech. 2019; 82(6): 812-848.
8. Zheng X, Shi J, Bu Y, Tian G, Zhang X, Yin W, et al. Silica-coated bismuth sulfide nanorods as multimodal contrast agents for a non-invasive visualization of the gastrointestinal tract. Nanoscale. 2015; 7(29): 12581-12591.
9. Luo S, Zhang E, Su Y, Cheng T, Shi C. A review of NIR dyes in cancer targeting and imaging. Biomaterials. 2011; 32(29): 7127-7138.
10. Chen ZY, Wang YX, Lin Y, Zhang JS, Yang F, Zhou QL, et al. Advance of molecular imaging technology and targeted imaging agent in imaging and therapy. Biomed Res Int. 2014; 2014: 819324.
11. James ML, Gambhir SS. A molecular imaging primer: modalities, imaging agents, and applications. Physiol Rev. 2012; 92(2): 897-965.
12. Huerta-Reyes M, Maya-Núñez G, Pérez-Solis MA, López-Muñoz E, Guillén N, Olivo-Marin JC, et al. Treatment of breast cancer with gonadotropin-releasing hormone analogs. Front Oncol. 2019; 9: 943.
13. Deng X, Qiu Q, Ma K, Huang W, Qian H. Synthesis and in vitro anti-cancer evaluation of luteinizing hormone-releasing hormone-conjugated peptide. Amino Acids. 2015; 47(11): 2359-2366.
14. Schally AV, Engel JB, Emons G, Block NL, Pinski J. Use of analogs of peptide hormones conjugated to cytotoxic radicals for chemotherapy targeted to receptors on tumors. Curr Drug Deliv. 2011; 8(1): 11-25.
15. Schally AV, Comaru-Schally AM, Nagy A, Kovacs M, Szepeshazi K, Plonowski A, et al. Hypothalamic hormones and cancer. Front Neuroendocrinol. 2001; 22(4): 248-291.
16. Schally AV, Nagy A. Chemotherapy targeted to cancers through tumoral hormone receptors. Trends Endocrinol Metab. 2004; 15(7): 300-310.
17. Roy J, Kaake M, Low PS. Small molecule targeted NIR dye conjugate for imaging LHRH receptor positive cancers. Oncotarget. 2019; 10(2): 152.
18. Venturelli M, Guaitoli G, Omarini C, Moscetti L. Spotlight on triptorelin in the treatment of premenopausal women with early-stage breast cancer. Breast Cancer (Dove Med Press). 2018; 10: 39-49.
19. Mező G, Manea M. Receptor-mediated tumor targeting based on peptide hormones. Expert Opin Drug Deliv. 2010; 7(1): 79-96.
20. Zu Y, Yong Y, Zhang X, Yu J, Dong X, Yin W, et al. Protein-directed synthesis of Bi2S3 nanoparticles as an efficient contrast agent for visualizing the gastrointestinal tract. RSC Adv. 2017; 7(28): 17505-17513.
21. Vattikuti SVP, Police AKR, Shim J, Byon C. Sacrificial-template-free synthesis of core-shell C@ Bi2S3 heterostructures for efficient supercapacitor and H2 production applications. Sci Rep. 2018; 8: 4194.
22. De La Vega JC, Häfeli UO. Utilization of nanoparticles as X-ray contrast agents for diagnostic imaging applications. Contrast Media Mol Imaging. 2015; 10(2): 81-95.
23. Ahamed M, Akhtar MJ, Khan MM, Alrokayan SA, Alhadlaq HA. Oxidative stress mediated cytotoxicity and apoptosis response of bismuth oxide (Bi2O3) nanoparticles in human breast cancer (MCF-7) cells. Chemosphere. 2019; 216: 823-831.
24. Dong L, Zhang P, Liu X, Deng R, Du K, Feng J, et al. Renal clearable Bi–Bi2S3 heterostructure nanoparticles for targeting cancer theranostics. ACS Appl Mater Interfaces. 2019; 11(8): 7774-7781.
25. Algethami M, Blencowe A, Feltis B, Geso M. Bismuth sulfide nanoparticles as a complement to traditional iodinated contrast agents at various x-ray computed tomography tube potentials. J Nanomater Mol Nanotechnol. 2017; 9: 25-28.

Original Article

Ionizing Radiation Promotes Epithelial-Mesenchymal Transition Phenotype and Stem Cell Marker in The Lung adenocarcinoma: *In Vitro* and Bioinformatic Studies

Mehdi Raei, Ph.D.[1], Mahdi Bagheri, Ph.D.[2], Safieh Aghaabdollahian, Ph.D.[3], Masoud Ghorbani, Ph.D.[4*], Afshin Sadeghi, M.Sc.[2]

1. Health Research Center, Life Style Institute, Baqiyatallah University of Medical Sciences, Tehran, Iran
2. Student Research Committee, Baqiyatallah University of Medical Sciences, Tehran, Iran
3. Department of Nanobiotechnology, New Technologies Research Group, Pasteur Institute of Iran, Tehran, Iran
4. Applied Biotechnology Research Center, Baqiyatallah University of Medical Sciences, Tehran, Iran

**Corresponding Address: P.O.Box: 19395-5487, Applied Biotechnology Research Center, Baqiyatallah University of Medical Sciences, Tehran, Iran*
Email: yasin.ghorbani93@gmail.com

Received: 31/December/2021, Accepted: 16/April/2022

Abstract

Objective: Ionizing radiation (IR) is one of the major therapeutic approaches in the non-small cell lung cancer (NSCLC); however, it can paradoxically result in cancer progression likely through promoting epithelial-mesenchymal transition (EMT) and the cancer stem cell phenotype. Therefore, we aimed to determine whether IR promote EMT/CSC and to investigate the clinical relevance of EMT/CSC hallmark genes.

Materials and Methods: In this experimental and bioinformatic study, A549 cell line was irradiated with a high dosage (6 Gy) or a fractionated regimen (2 Gy/day for 15 fractions). The EMT-related features, including cellular morphology, migratory and invasive capacities were evaluated using scratch assay and transwell migration/invasion assays. The mRNA levels of EMT-related genes (*CDH1, CDH2, SNAI1* and *TWIST1*), stemness-related markers (*CD44, PROM1,* and *ALDH1A1*) and the *CDH2/CDH1* ratio were evaluated via real-time polymerase chain reaction (PCR). The clinical significance of these genes was assessed in the lung adenocarcinoma (LUAD) samples using online databases.

Results: Irradiation resulted in a dramatic elongation of cell shape and enhanced invasion and migration capabilities. These EMT-like alterations were accompanied with enhanced levels of *SNAI1, CDH2, TWIST1, CD44, PROM1*, and *ALDH1A1* as well as an enhanced *CDH2/CDH1* ratio. *TCGA* analysis revealed that, *TWIST1, CDH1, PROM1* and *CDH2* were upregulated; whereas, *CD44, SNAI1* and *ALDH1A1* were downregulated. Additionally, correlations between *SNAI1-TWIST1, CDH2-TWIST1, CDH2-SNAI1*, and *ALDH1A1-PROM1* was positive. Kaplan-Meier survival analysis identified lower expression of *CDH1, PROM1* and *ALDH1A1* and increased expression of *CDH2, SNAI1*, and *TWIST1* as well as *CDH2/CDH1* ratio predict overall survival. Additionally, downregulation of *ALDH1A1* and upregulation of *CDH2, SNAI1* and *TWIST1* could predict a shorter first progression.

Conclusion: Altogether, these findings demonstrated that IR promotes EMT phenotype and stem cell markers in A549 cell line and these genes could function as diagnostic or prognostic indicators in LUAD samples.

Keywords: Dose Fractionation Lung Neoplasms, Epithelial-Mesenchymal Transition, Neoplastic Stem Cells, Radiotherapy

Cell Journal(Yakhteh), Vol 24, No 9, September 2022, Pages: 522-530

Citation: Raei M, Bagheri M, Aghaabdollahian S, Ghorbani M, Sadeghi A. Ionizing radiation promotes epithelial-mesenchymal transition phenotype and stem cell marker in the lung adenocarcinoma: in vitro and bioinformatic studies. Cell J. 2022; 24(9): 522-530. doi: 10.22074/cellj.2022.8403.

Introduction

Lung cancer is one of the most common cancers worldwide that leads to the highest number of cancer mortality. Lung cancer accounts for one-quarter of all cancer deaths (1). Non-small-cell lung cancer (NSCLC) is regarded as the main type of lung cancer, 85% of cases (2). In spite of the improvement in the survival rate of most cancers, the 5-year survival rate is 5% of lung cancer cases with distant stage disease (1). This low rate of survival could be due to intrinsic or acquired resistance to treatments, including radiotherapy and chemotherapy. Thus, it is necessary to define the molecular mechanism of such resistance and also, exploit potential agents to improve the lung cancer patient survival.

Ionizing radiation (IR), is classified as a main treatment strategy for patients with lung cancer. Various efforts such as dose escalation and altered fractionation have been done to improve the outcome (3). However, the results are inconclusive owing to various obstacles such as radioresistance. Emerging results demonstrated that epithelial-mesenchymal transition (EMT) can lead to the development of therapy resistance in lung cancer (4-6). EMT is a fundamental program that contributes to physiological events including embryogenesis and wound healing or human pathology including fibrosis and tumorigenic process. During EMT, an epithelial cell loses its traits such as epithelial junction and instead develops mesenchymal features including elongation of cytoplasm and nucleus, enhanced motility and invasive capacities. Moreover, EMT phenotype that contributes to the migration and invasion of tumor cells, also promotes the tumor cell dissemination from a primary site to secondary distant sites, and overrides chemotherapy- or radiotherapy-induced apoptosis (7). These changes are

regulated by EMT-core transcriptional factors which include SNAIL, TWIST, and zinc-finger E-box-binding (ZEB) families (8). For example, SNAIL and TWIST1 suppress the expression of genes linked to the epithelial phenotype such as *CDH1* (encoding E-cadherin) and concurrently promote the expression of genes linked to the mesenchymal phenotype such as *CDH2* (encoding N-cadherin). Moreover, the activation of EMT enables tumor cells to acquire stem-like properties, termed cancer stem cell (CSC) state. Enforced expression of EMT-master transcription factors such as SNAIL or TWIST in the epithelial cells induces the CSC phenotype development linking EMT phenotype with CSC state. These CSC subpopulations are defined using cell-surface markers such as CD44 and CD133 or via functional regulator of stemness such as ALDH (7).

Studies indicated that IR can lead to the EMT phenotype in the NSCLC cell lines (5, 6). Also, the induced changes were linked with enhanced radioresistance (5). A study showed that dose escalation might improve the survival rate of patients (9); while another report indicated that dose escalation not only did not improve the survival rate but also could likely be harmful (3).

A recent study documented that fractionation of irradiation (5 or 10 fractions of 2 Gy given one fraction per day) could induce EMT phenotype in the A549 human NSCLC cell line but not in the HT-29 human colorectal adenocarcinoma cell line (6). Induction of EMT phenotype that is recently envisioned to be the main cause of radioresistance might be impaired using higher dose or higher fractions of IR. In this study, we aimed to determine whether a higher dose or higher fractions of IR could induce EMT phenotype. Furthermore, the clinical significance of EMT and CSC-related genes was identified.

Materials and Methods

Cell culture

In this experimental and bioinformatic study, the human NSCLC cell line, A549, was obtained from National Cell Bank of Iran (NCBI). The cells were maintained in the Dulbecco's modified eagle's medium (DMEM, Gibco, Grand Island, NY, USA). The culture medium was completed via 10% (v/v) fetal bovine serum (FBS, Gibco, Grand Island, NY, USA), and 1% (v/v) penicillin/streptomycin. The cultured cells were incubated at 37ºC in a humidified 5% CO_2 environment. The present study was conducted with the approval of the Ethical Committee of the Baqiyatallah University of Medical Sciences, Tehran, Iran (IR.BMSU.REC.1399.414).

Irradiation

The A549 cell line was cultured in T25 flasks (Cat. No. 70025, SPL Life Sciences, Pocheon, South Korea). Once the cultured cells were more than 50-60% confluent, the cells were irradiated via a Varian linear accelerator (Varian Medical Systems, Palo Alto, CA, USA) with 6 MV energy and at a 2 Gy per min dose rate. The irradiation was performed with either a high dose of 6 Gy or a fractionated regimen consisting of a 2 Gy per fraction (five times/week) for 15 fractions (15 FR). Different analyses were carried out after 24 hours after the last irradiation.

Wound healing assay

Immediately, after the final irradiation, the cells were washed 3 times with phosphate buffered saline (PBS, Cat. No. BI-1401, Bioidea, Tehran, Iran) and digested by trypsin. Thereafter, the trypsin- digested cells were washed using PBS and resuspended in the complete medium. A sufficient number of cells ($\cong 5\times10^5$) were cultured into 6-well plates (Cat. No. 30006, SPL Life Sciences, Pocheon, South Korea) and allowed to adhere for 24 hours and reach confluency. The control (non-irradiated) cells were treated identically to the irradiated cells. The cell monolayer was scratched in a straight line via a sterile 200 µL pipette tip. To remove cell debris, the cells were washed with DMEM. Culture medium (DMEM) supplemented with 1% FBS was added and incubated in a 5% CO_2 environment at 37ºC. This FBS percentage was used to minimize the effect of cell proliferation on the assessment of migration. The wounded areas were captured through a microscope with 10x magnification at 0, 18, and 36 hours after wounding. The images were analyzed using ImageJ MRI-Wound-Healing-Tool (National Institutes of Health, Bethesda, Maryland, USA).

Transwell migration and invasion assays

The migratory capacity of irradiated and control cells was determined via transwell migration assay using 24-well transwell inserts (Cat. No. 35224, SPL Life Sciences, Pocheon, South Korea). The cells were seeded in the serum-free medium on the upper side of the porous membrane (8 µm pore size) of transwell insert. The transwell insert was placed in the lower well that was filled with 650 µL complete medium and incubated for 24 hours at 37ºC in a 5% CO_2 environment. The non-migrated cells were removed using a cotton swab, and the migrated cells were fixed and stained with methanol and crystal violet, respectively. The migrated cells were counted with ImageJ. Migration of cells was expressed as a relative migration which is calculated by percentage of a number of the migrated irradiated cells to the migrated control cells.

The invasive capacity of irradiated and control cells was evaluated via transwell invasion assay, which is carried out like transwell migration assay. Unlike transwell migration assay, the porous membrane must be pre-coated with matrigel (BD Biosciences, San Jose, CA, USA) in this assay. The invasion capability of the cells was expressed as relative invasion which is defined as percentage of invasion of the irradiated cells to invasion of control cells.

Real-time polymerase chain reaction

The mRNA levels of EMT and CSC markers were

evaluated via Quantitative real-time polymerase chain reaction (PCR). To this end, the total RNA extraction was carried out via RNeasy Plus-Mini Kit (Qiagen, Hilden, Germany). cDNA synthesis from 1 µg of the extracted-RNA from each treatment group was performed using QuantiTect Reverse Transcription Kit (Qiagen, Hilden, Germany). The real time qPCR analysis was set up via the QuantiNova SYBR Green PCR Kit (Qiagen, Hilden, Germany) and carried out in a LightCycler 96 System (Roche, Basel, Switzerland). The primer sequences were listed in a previous study (6). The primers with their melting temperatures (Tm), the accession number of the targeted refseq mRNA and length of the amplicon were provided in the Table S1 (See Supplementary Online Information at www.celljournal.org). The relative quantitation of gene expression was measured via the comparative CT (ΔΔCT) method and normalized to the HPRT gene. The Y- axis was represented as Log2 -transformed values.

Transcriptional expression and survival analysis using web tools

The relative expression of deregulated genes in human lung adenocarcinoma (LUAD) compared to normal samples was evaluated in The Cancer Genome Atlas (TCGA, http://cancergenome.nih.gov) using UALCAN (http://ualcan.path.uab.edu/) web tool. It should be noted that between the two predominant NSCLC histological phenotypes including adenocarcinoma and squamous cell carcinoma, we chose the adenocarcinoma because of our cell line. The analysis was carried out on 515 primary tumors of LUAD and 59 normal samples from TCGA. The expression of the gene of interest is provided as transcripts per million via Box and whisker plot. Moreover, the T-test was done via a PERL script with Comprehensive Perl Archive Network (CPAN) module "Statistics::TTest" (http://search.cpan.org/~yunfang/Statistics-TTest-1.1.0/TTest.pm) in order to evaluate the significance of difference in mRNA levels between primary tumors of LUAD and normal samples from TCGA (10). Additionally, the correlation among genes was evaluated in the LUAD samples from TCGA database using the gene expression profiling interactive analysis (GEPIA, http://gepia.cancer-pku.cn/) (11). The correlation coefficients (R value) were interpreted as follows: 0.00-0.1 indicates a negligible relationship; 0.1-0.39 indicates a weak relationship; 0.4-0.69 indicates a moderate relationship; 0.7-0.89 indicates a strong relationship; 0.9-1 indicates a very strong relationship (12).

The prognostic significance of the genes of interest in the human LUAD was evaluated using an online Kaplan-0Meier plotter (www.kmplot.com) which includes the microarray gene expression data and clinical survival data from the Cancer Biomedical Informatics Grid (caBIG, http://cabig.cancer.gov), the Gene Expression Omnibus (GEO, https://www.ncbi.nlm.nih.gov/geo/) and TCGA databases (13). According to the median value, the cases were classified into two risk groups, i.e. patient groups with higher or lower expression level of the gene of interest. The influence of differential gene expression on the overall survival (OS) and the first progression (FP) were determined via Kaplan-Meier curves. Of note, mean expression of the selected gene-probe sets was used when the prognostic value of metagene signatures was evaluated. Kaplan-Meier curves were provided with Hazard ratio (HR) and its 95% confidence intervals as well as log-rank P values. Moreover, $P<0.05$ were regarded to be statistically significant.

Statistical analysis

The statistical analysis was done via SPSS v.24.0 (SPSS, Inc., Chicago, IL). The Kolmogorov-Smirnov test was performed to evaluate whether the data was normally distributed. Mean differences between two groups were evaluated using the Independent t test, while, in the case of more than two groups, one-way analysis of variance (ANOVA) was carried out. A $P<0.05$ was regarded statistically significant. The data were shown as mean ± SD.

Results

Ionizing radiation changes cellular morphology

A previous study demonstrated that 2 Gy/day of fractionated radiotherapy for 5 or 10 days could promote EMT phenotype in the A549 cells (6); therefore, we aimed to evaluate whether higher fractions (15 fractions) or higher dose of IR could still induce EMT in the A549 cells (Fig.1A). As shown in Figure 1B, the morphology of irradiated A549 cells was significantly different in comparison with the control cells that did not receive any irradiation. Irradiation either fractionated (15FR) or high dose (6 Gy) resulted in a dramatic elongation of cellular shape and formation of membrane protrusions. These changes, which are characteristics of mesenchymal-like phenotype indicated that IR could promote EMT phenotype in A549 cell line.

Ionizing radiation enhances cell motility

Previous studies linked IR with enhanced cell motility. Based on the available data and morphological changes displayed above, we hypothesized that higher dose or higher fractions of IR could enhance cell motility. To evaluate this, we carried out a wound healing assay in which a wound was made in a confluent monolayer of control and irradiated cells (Fig.1C). As seen in Figure 1D, irradiated cells were able to refill the wounded area significantly faster than the control cells.

For A549-15 FR and A549-6 Gy cells, wound closure was 92.71% and 77.04% of the initial size after 36 hours,

respectively; whereas, for the control cells (no irradiation), wound closure was only 41.80% of the wounded area after 36 hours. This data indicated that irradiated cells had a higher motility than the control cells.

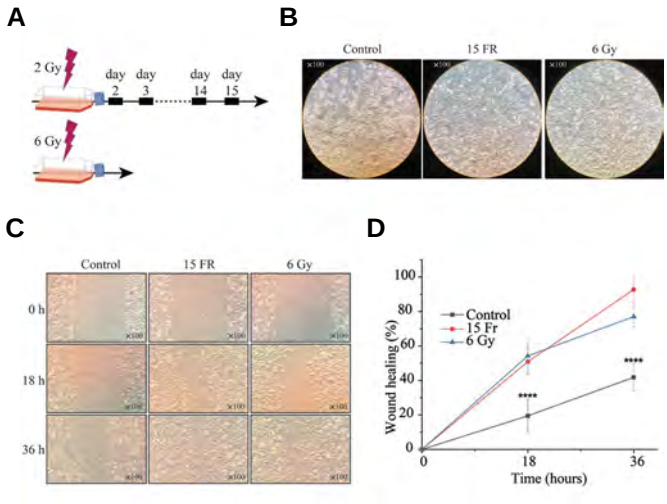

Fig.1: Ionizing radiation (IR) leads to morphological changes and enhanced migratory capacity of A549 cell line. **A.** Schematic representation of the cell line irradiation schedule. The A549 cells were irradiated with either a fractionated regimen comprising a 2 Gy fraction each day for 15 fractions (15 FR) or a single high dose of 6 Gy. **B.** Representative images of morphological alterations mediated by IR. **C.** Representative bright-field images showed that the scratches were enclosed faster in the irradiated cells. **D.** The motility of irradiated cells was statistically enhanced in comparison with the non-irradiated cells (****; P<0.001). The data were expressed as mean ± SD.

Ionizing radiation induces the migratory and invasive behaviors

EMT is featured with enhanced migratory and invasive capabilities (7). To further determine whether irradiated cells undergo EMT, we performed serum-promoted migration and invasion assays via transwell inserts. As represented in Figure 2A and B, A549-15 FR and A549-6 Gy cells migrated 46.67% (P=0.001) and 41.72%, respectively (P=0.004) that were migrated more than the non-irradiated cells through porous membrane. Moreover, the irradiated cells, A549-15 FR and A549-6 Gy, invaded 64.78% (P<0.001) and 45.18% (P=0.009) more than the parental cells through matrigel-coated membrane, respectively (Fig.2A). These results demonstrated that either higher fractions or higher dose of IR increased the migratory and invasive behaviors of the A549 cell line.

Ionizing radiation regulates EMT markers

To explore whether irradiation regulates the molecular changes consistent with EMT and CSC states, we performed RT-qPCR for several classic EMT/CSC marker genes. *CDH1*, an epithelial state marker, was not significantly downregulated in the A549-15 FR (P=0.665) and the A549-6 Gy (P=0.364); while, *CDH2*, the mesenchymal marker, was significantly upregulated in the A549-15 FR (P=0.024) and the A549-6 Gy (P<0.001, Fig.3A). The process of reduced expression of *E-CADHERIN* and increased expression of *N-CADHERIN* is referred to as 'Cadherin switch' which is considered as the EMT hallmark. We measured *CDH2* over *CDH1* ratio which could be an indicator of cadherin switch. This ratio in the A549-15 FR and the A549-6 Gy were approximately 10.59 (P<0.001) and 8.48 (P<0.001) folds higher, respectively, than in the control cells (Fig.3B), emphasizing the induction of EMT phenotype in the irradiated cells. Moreover, EMT related markers including *SNAI1* (A549-15 FR, A549-6 Gy, P<0.001) and *TWIST1* (A549-15 FR, P=0.036, A549-6 Gy, P<0.001) and CSC markers including *CD44* (A549-15 FR, A549-6 Gy, P<0.001), *PROM1* (A549-15 FR, A549-6 Gy, P<0.001) and *ALDH1A1* (A549-15 FR, P=0.036, A549-6 Gy, P<0.001) were significantly upregulated in irradiated cells.

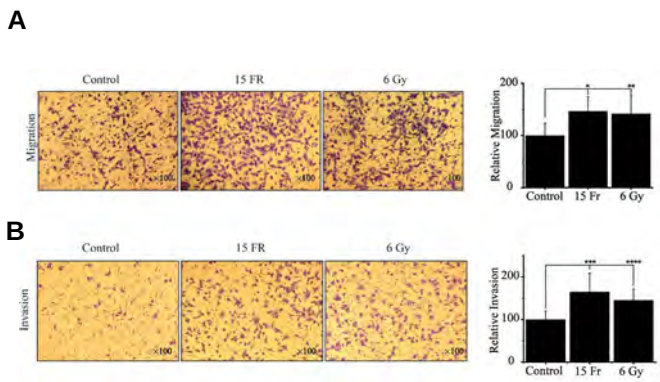

Fig.2: Ionizing Radiation (IR) increased the migratory and invasive capacities of A549 cell line. **A.** Microscopic images of migrated cells (on the left) and the analysis (on the right) showed the relative migration of A549-15 FR cells (*; P=0.001) and A549-6 Gy cells (**; P=0.004) was statistically more than that of non-irradiated cells. **B.** Microscopic images of migrated cells (on the left) and the analysis (on the right) showed the relative invasion of A549-15 FR cells (***; P<0.001) and A549-6 Gy cells (****; P=0.009) was statistically increased in comparison with the non-irradiated cells.

Transcriptional expression of deregulated genes in human LUAD

To further assess the clinical significance of our data, we analyzed the correlation of expression of EMT related genes with clinically relevant parameters. Using TCGA database, we first assessed the expression level of these genes in the human LUAD tumor tissues and compared with the normal non-cancerous tissues. Our analyses indicated that the expression of all seven genes was significantly altered in the tumor samples in comparison with the normal tissues (P<0.05). Consistent with their enhanced expression

in the irradiated A549 cells, *CDH2* (P<0.001), *PROM1* (P<0.001) and *TWIST1* (P<0.001) were statistically upregulated in the LUAD samples in comparison with the normal samples; while unlike cell line data, *CDH1* (P<0.001) was significantly upregulated and *CD44* (P<0.001), *SNAI1* (P=0.03), and *ALDH1A1* (P<0.001) were significantly downregulated in the tumor tissues (Fig.4A-G).

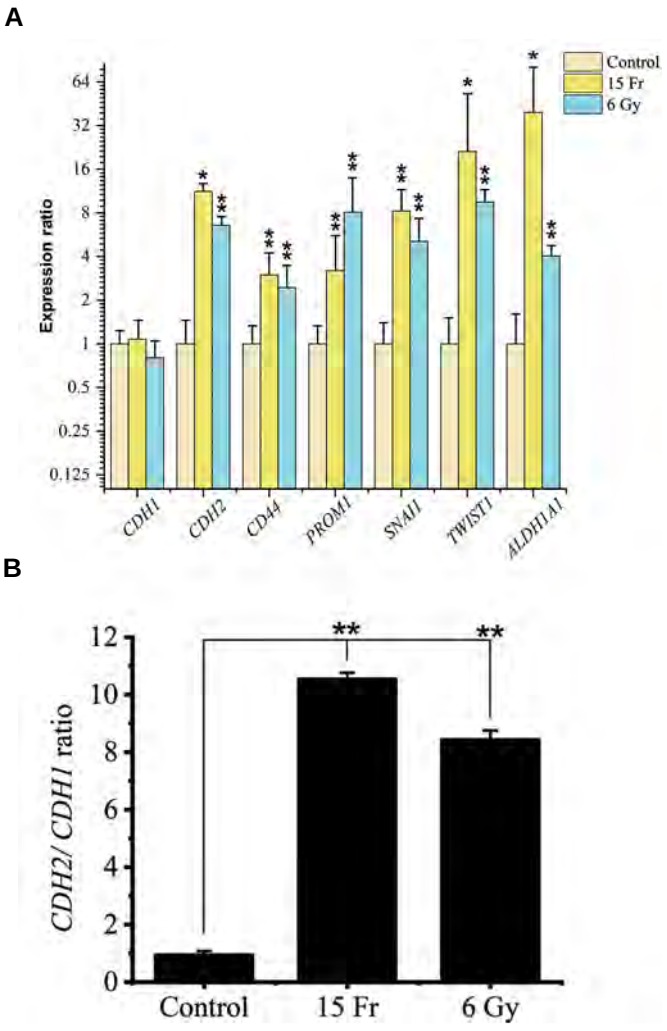

Fig.3: Ionizing radiation (IR) deregulated the expression of EMT related genes. **A.** The expression levels of *CDH2* (A549-15 FR: P=0.024, A549-6 Gy: P<0.001), *CD44* (A549-15 FR, A549-6 Gy: P<0.001), *PROM1* (A549-15 FR, A549-6 Gy: P<0.001), *SNAI1* (A549-15 FR, A549-6 Gy: P<0.001), *TWIST1* (A549-15 FR: P=0.036, A549-6 Gy: P<0.001) and *ALDH1A1* (A549-15 FR: P=0.036, A549-6 Gy: P<0.001) were significantly enhanced in the irradiated cells. **B.** The *CDH2* over *CDH1* ratio is enhanced (A549-15 FR, A549-6 Gy: P<0.001) in the irradiated cells in comparison with the non-irradiated cells. EMT; Epithelial-mesenchymal transition, *; P<0.05; and **; P<0.001.

Moreover, correlation among the EMT related genes was assessed in the LUAD samples from the TCGA using GEPIA. The analysis represented that there was a moderate and statistically significant correlation between *SNAI1* and *TWIST1* expression (R=0.48, P<0.001, Fig.4H). Moreover, the correlation between a pair of genes, including *CDH2-TWIST1* (R=0.36, P<0.001), *CDH2- SNAI1* (R=0.34, P<0.001), and *ALDH1A1-PROM1* (R=0.34, P<0.001) were weak but significant. However, the correlation among other genes was negligible (data not shown).

These data showed that the mRNA levels of EMT related genes are altered in primary lung cancer patient tissues, suggesting the potential importance of these genes in lung cancer development.

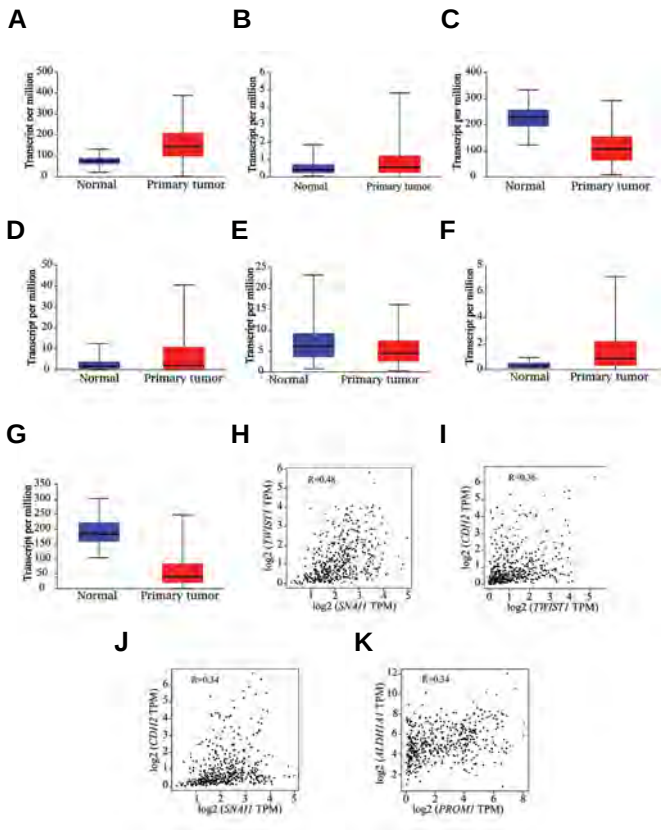

Fig.4: The expression of epithelial-mesenchymal transition (EMT) related genes was evaluated in the human lung adenocarcinoma (LUAD) tissues and the normal tissues deposited in the The Cancer Genome Atlas (TCGA) database. The analysis was carried out on the 515 primary LUAD tissues and the 59 normal samples. **A.** *CDH1* (P<0.001), **B.** *CDH2* (P<0.001), **C.** *CD44* (P<0.001), **D.** *PROM1* (P<0.001), **E.** *SNAI1* (P=0.03), **F.** *TWIST1* (P<0.001), **G.** *ALDH1A1* (P<0.001), **H.** *SNAI1* expression was associated with *TWIST1* expression in the LUAD patients (P<0.001). **I.** *TWIST1* expression was associated with *CDH2* expression in the LUAD patients (P<0.001). **J.** *SNAI1* expression was correlated with the *CDH2* expression in the LUAD patients (P<0.001). **K.** *PROM1* expression was associated with *ALDH1A1* expression in the LUAD patients (P<0.001).

Survival analysis of the deregulated genes in the human LUAD

Given the significant gene expression alterations of EMT related genes in the patient tumor tissues, we then assessed their association with survival rates of the LUAD patients. Survival analysis exhibited that

expression levels of *CDH1* (P=0.7), *CDH2* (P=0.85), *CD44* (P=0.45), *PROM1* (P=0.069), *SNAI1* (P=0.26), *TWIST1* (P=0.49), *ALDH1A1* (P=0.67), and Cadherin switch (P=0.7) did not statistically correlate with survival of the lung cancer patients who underwent radiotherapy (Fig.5).

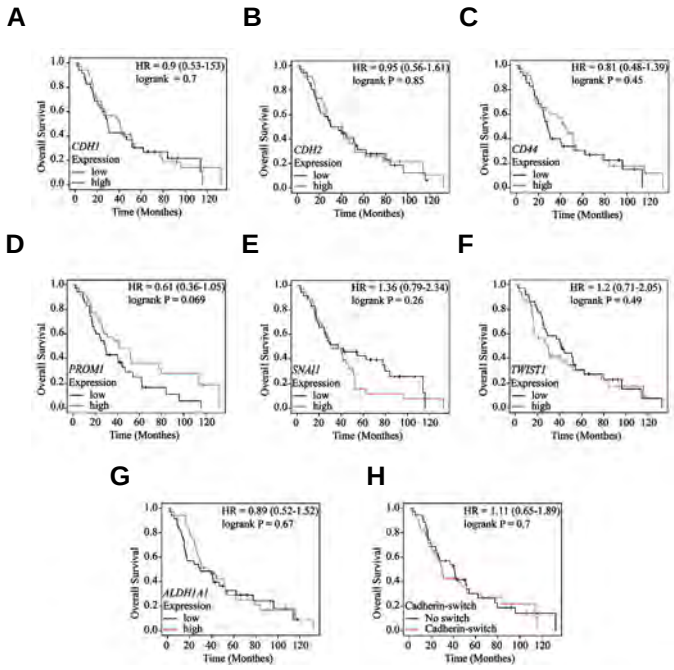

Fig.5: The overall survival (OS) lung adenocarcinoma (LUAD) patients who received radiotherapy was evaluated via the Cancer Biomedical Informatics Grid (caBIG), The Cancer Genome Atlas (TCGA) and GEO databases using the Kaplan–Meier plotter. **A.** *CDH1* (patients with high (35) and low (35) expression of *CDH1*; probe sets: 201130_s_at and 201131_s_at), **B.** *CDH2* (patients with high (34) and low (36) expression of *CDH2*; probe sets: 203440_at and 203441_s_at), **C.** *CD44* (patients with high (35) and low (35) expression of *CD44*; probe sets: 204490_s_at, 209835_x_at, 210916_s_at, 212014_x_at, 212063_at, 216056_at and 217523_at). **D.** *PROM1* (patients with high (35) and low (35) expression of *PROM1*; probe set: 204304_s_at). **E.** *SNAI1* (patients with high (35) and low (35) expression of *SNAI1*; probe set: 219480_at). **F.** *TWIST1* (patients with high (34) and low (36) expression of *TWIST1*; probe set: 213943_at). **G.** *ALDH1A1* (patients with high (35) and low (35) expression of *ALDH1A1*; probe set: 212224_at). **H.** Cadherin switch (Patients with cadherin switch (335) and no cadherin switch (35); probe sets: 201130_s_at, 201131_s_at, 203440_at and 203441_s_at).

Moreover, Kaplan-Meier analyses showed that elevated expression of *CDH2* (with HR=1.56 and P<0.001), *SNAI1* (with HR=1.41 and P=0.003) and *TWIST1* (with HR=1.31 and P=0.022) significantly correlated with decreased OS; whereas, decreased expression of *CDH1* (with HR=0.68 and P=0.001), *PROM1* (with HR=0.76 and P=0.02) and *ALDH1A1* (with HR=0.71 and P=0.004) significantly correlated with decreased OS (Fig.6). Moreover, the survival analysis of Cadherin switch (a subgroup in which *CDH1* is reduced and *CDH2* is enhanced) revealed that this combination was statistically correlated with reduced OS (HR=1.53, P<0.001) in LUAD patients (Fig.6H).

In the FP case, higher expression of *CDH2* (HR=1.88, P<0.001), *SNAI1* (HR=1.89, P<0.001) and *TWIST1* (HR=1.76, P<0.001) were significantly correlated with a shorter FP survival, while decreased expression of *ALDH1A1* (HR=0.59, P=0.001) was significantly correlated with a shorter FP survival (Fig.S1, See Supplementary On line Information at www.celljournal.org). Altogether, these data revealed the prognostic value of some of EMT related genes in lung cancer.

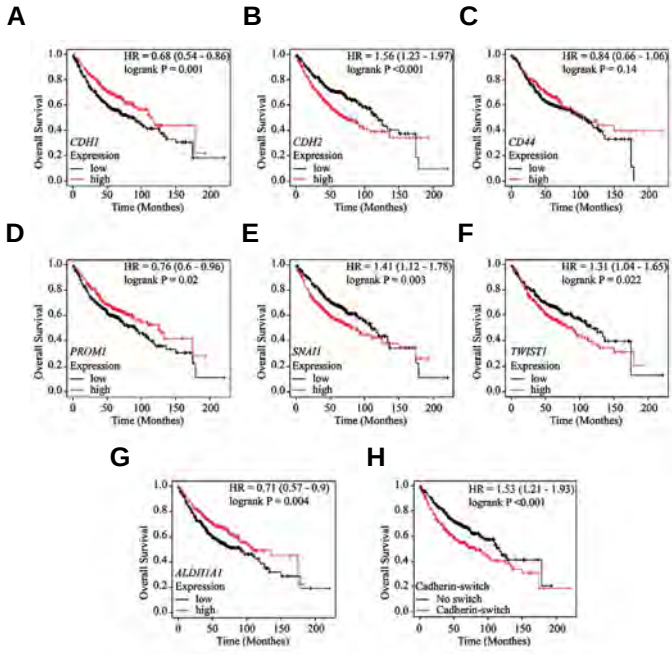

Fig.6: The overall survival (OS) of the lung adenocarcinoma (LUAD) patients was evaluated in the Cancer Biomedical Informatics Grid (caBIG), The Cancer Genome Atlas (TCGA) and GEO databases using the Kaplan–Meier plotter. **A.** *CDH1* (patients with high (359) and low (360) expression of *CDH1*; probe sets: 201130_s_at and 201131_s_at), **B.** *CDH2* (patients with high (359) and low (360) expression of *CDH2*; probe sets: 203440_at and 203441_s_at), **C.** *CD44* (patients with high (336) and low (336) expression of *CD44*; probe sets: 1557905_s_at, 204489_s_at, 204490_s_at, 209835_x_at, 210916_s_at, 212014_x_at, 212063_at, 216056_at and 217523_at). **D.** *PROM1* (patients with high (359) and low (360) expression of *PROM1*; probe set: 204304_s_at). **E.** *SNAI1* (patients with high (356) and low (363) expression of *SNAI1*; probe set: 219480_at). **F.** *TWIST1* (patients with high (359) and low (360) expression of *TWIST1*; probe set: 213943_at). **G.** *ALDH1A1* (patients with high (359) and low (360) expression of *ALDH1A1*; probe set: 212224_at). **H.** cadherin switch (patients with cadherin switch (359) and no cadherin switch (360); probe sets: 201130_s_at, 201131_s_at, 203440_at and 203441_s_at).

Discussion

Because of often asymptotic in the earlier stages, many cases of lung cancer patients were diagnosed at a distant stage. More than 50% of lung cancer at distant stage are treated with radiotherapy; however, the 5-year survival rate is 5% for these cases (14). Therefore, radiotherapy for these cases mainly remains palliative because of the intrinsic and/or acquired radioresistance (5). Identification of the mechanism and signaling pathway underlying such resistance might be crucial to find the therapeutic targets and develop novel therapeutic strategies to avert

radioresistance and eventually enhance the survival rate of patients. Recently, the radioresistance phenotype has been ascribed to a subset of tumor cells undergoing EMT (15). A previous study demonstrated that irradiation of 2Gy/day for 5 or 10 consecutive days promoted EMT phenotype in NSCLC cell line (A549) but not in the human colorectal adenocarcinoma cell line (HT-29). It was documented that higher fractions or higher doses of radiation are two strategies to improve radiotherapy outcome probably through reversing phonotypes that are ascribed to radioresistance such as EMT (16). Therefore, in the current study, we evaluated whether higher fractions or higher dosage of radiation could induce EMT in the NSCLC cell line, A549 Cell line. We observed that IR either fractionated or high dose could promote EMT phenotype in A549 cell line.

EMT is a complex program that enables epithelial cells to lose their features and acquire more mesenchymal features. Furthermore, EMT participates in the embryogenesis and the underlying mechanism is reactivated in the tumor progression and metastasis (7). Induction of EMT process regulates numerous aspects of cellular physiology, including cytoskeletal reorganization, cellular shape, loss of epithelial cell contacts, cellular polarity, development of cellular protrusions and induction of migratory and invasive capacities (17). These cellular changes are orchestrated via a cohort of transcription factors such as SNAIL, TWIST, and Zeb families (8). Many signals from tumor microenvironment have been identified that could lead to the EMT induction (18). In the current study, we also demonstrated that IR could promote morphological changes, including elongation of cellular shape, formation of membrane protrusions and loss of cell-cell interactions. These morphological changes were accompanied with enhanced motility of irradiated cells, a feature that plays a pivotal role in the cancer cell metastasis. Furthermore, the invasive capability of irradiated cells increased in comparison with non-irradiated cells. Accordingly, these findings were consistent with induction of Cadherin switch and enhanced the mRNA levels of mesenchymal markers (*CDH2*, *SNAI1* and *TWIST1*) and CSC marker (*CD44*, *PROM1* and *ALDH1A1*). These results were in consistence with previous findings that indicated that IR can induce an EMT state in the NSCLC cell lines (5, 19, 20). However, a previous study indicated that carbon ion irradiation inhibits the invasive capacity of the A549 cell line, demonstrating that carbon ion irradiation is more effective than photon irradiation in the suppressing the metastatic abilities of A549 cells (21). In the current study, we demonstrated that IR could induce Cadherin switch. During this switch, the transitioning cells tend to contact with mesenchymal cells instead of epithelial cells. However, the contacts between mesenchymal cells are weaker since the interaction between the homotypic *N-CADHERIN* is weaker than that of the homotypic *E-CADHERIN*. Thereby, Cadherin switch facilitates the motility and invasion (22, 23). Consistently, we showed that Cadherin switch is positively associated with the enhanced migration and invasion. As indicated, these processes are orchestrated by a set of transcription factors (22). Accordingly, we demonstrated that *TWIST1*, an EMT transcription factor that has emerged as a master regulator of the Cadherin switch (24-26), was significantly upregulated in the irradiated cells. After identification of the deregulated genes upon IR, their clinical relevance was evaluated using in silico approaches. The TCGA database composed 515 primary LUAD tumors and 59 normal samples. The TCGA database analysis revealed that *CDH1* was significantly upregulated in the LUAD samples. While, in vitro analysis indicated that IR did not statistically alter the *CDH1* expression in the NSCLC cell line and the reduced expression of *CDH1* predicted a poor prognosis of the LUAD patients. However, further studies are required to address the potential link between *CDH1* expression and prognosis of lung cancer patients who have undergone radiotherapy. In line with our irradiated *in vitro* model, *CDH2*, was significantly upregulated in the LUAD samples deposited in the TCGA database and this upregulation predicted a poor prognosis (both OS and FP) of LUAD patients. Cadherin switch could also predict the OS of the LUAD patients. The prognostic value of Cadherin switch was reported for prostate cancer and extrahepatic cholangiocarcinoma (27, 28). Given to the observed correlation between mRNA levels of *CDH2* and *TWIST1* in the LUAD and normal samples, the same trend was observed for *TWIST1*. Consistently, another study identified that either *CDH2* or *TWIST1* in primary NSCLCs was associated with a shorter OS (29). Altogether, these data indicated that these biomarkers might have diagnostic and/or prognostic values and targeting of which might be a therapeutic strategy, particularly in the case of LUAD that harbors an activating mutation in KRAS. Intriguingly, it was demonstrated that targeting of *TWIST1* has a synthetic lethal interaction with the frequently occurring *KRAS* mutation (30).

CD44 is mainly known as a CSC marker involving in the multiple aspects of metastasis, including proliferation, migration, invasion and radioresistance (31). A previous study, demonstrated that *CD44* is up regulated in the NSCLC cell line that undergone EMT and radioresistance phenotypes (6). While the bioinformatic analysis indicated that *CD44* is significantly downregulated in lung adenocarcinoma samples compared with normal tissues. These contradictory data indicate that radiotherapy might contribute in the induction of EMT or it might contribute in the selection of tumor cells undergoing EMT. In line with a meta-analysis (32), our bioinformatic data indicated that *CD44* expression did not significantly associated with OS and first progression. However, several studies indicated that *CD44* overexpression was associated with poor prognosis (33, 34); while, other studies demonstrated that downregulation of *CD44* was a poor prognostic factor demonstrating the dual role of *CD44* in cancer progression (35, 36). The dualistic role of *CD44* might be due to the cell lines variations, culture condition, tumor microenvironment, and evaluating *CD44* expression at

different stages of tumor progression (36). For example, hyaluronan (HA), one of the main elements of the ECM in the tumor microenvironment, in its high molecular weight could interact with *CD44* and promote formation of a complex among CXCL12, CD44 and CXCR4, that leads to angiogenesis and tumor metastasis, whereas low molecular weight hyaluronan could inhibit this complex formation (37). Additional controversies might be due to alternative splicing (38, 39). Alternative splicing of *CD44* generates two families of *CD44* isoforms, including: *CD44* standard isoform (*CD44*s) and variant isoforms of *CD44* (*CD44*v) (39). Recently, it has been identified that splice isoforms of *CD44* have opposite functions. *CD44*s is positively correlated with CSC/EMT gene signatures, while the *CD44*v shows an inverse correlation (38, 39). The *CD44*v is the major splice isoform in the epithelial state of tumor cells, however the *CD44*v expression switches to that of *CD44*s once the epithelial cells have undergone EMT or CSC phenotype. The *CD44* isoforms switching (*CD44*v to *CD44*s) is negatively regulated by ESRP1, a protein that is highly expressed in the epithelial cells (38, 39).

Conclusion

Altogether, these findings demonstrated that IR (either fractionated or high dose) could promote EMT in NSCLC cell line, A549 cell line, and EMT hallmark genes, particularly *CDH2* and *TWIST1*, could function as diagnostic or prognostic indicators in LUAD samples.

Acknowledgements

There is no financial support and conflict of interest in this study.

Authors' Contributions

M.R., M.B., M.G.; Contributed to conception and design. M.R., M.G., S.A., A.S.; Contributed to all experimental work, data and statistical analysis, and interpretation of data. M.G.; Overall supervision. M.G., S.A., A.S.; Drafted the manuscript. M.R., M.B.; Manuscript reviser. All authors read and approved the final manuscript.

References

1. Siegel RL, Miller KD, Jemal A. Cancer statistics, 2018. CA Cancer J Clin. 2018; 68(1): 7-30.
2. Chen Z, Fillmore CM, Hammerman PS, Kim CF, Wong KK. Non-small-cell lung cancers: a heterogeneous set of diseases. Nat Rev Cancer. 2014; 14(8): 535-546.
3. Bradley JD, Paulus R, Komaki R, Masters G, Blumenschein G, Schild S, et al. Standard-dose versus high-dose conformal radiotherapy with concurrent and consolidation carboplatin plus paclitaxel with or without cetuximab for patients with stage IIIA or IIIB non-small-cell lung cancer (RTOG 0617): a randomised, two-by-two factorial phase 3 study. Lancet Oncol. 2015; 16(2): 187-199.
4. Ghasemi Z, Tahmasebi-Birgani MJ, Ghafari Novin A, Motlagh PE, Teimoori A, Ghadiri A, et al. Fractionated radiation promotes proliferation and radioresistance in bystander A549 cells but not in bystander HT29 cells. Life Sci. 2020; 257: 118087.
5. Gomez-Casal R, Bhattacharya C, Ganesh N, Bailey L, Basse P, Gibson M, et al. Non-small cell lung cancer cells survived ionizing radiation treatment display cancer stem cell and epithelial-mesenchymal transition phenotypes. Mol Cancer. 2013; 12(1): 94.
6. Tahmasebi-Birgani MJ, Teimoori A, Ghadiri A, Mansoury-Asl H, Danyaei A, Khanbabaei H. Fractionated radiotherapy might induce epithelial-mesenchymal transition and radioresistance in a cellular context manner. J Cell Biochem. 2018; 120(5): 8601-8610.
7. Dongre A, Weinberg RA. New insights into the mechanisms of epithelial-mesenchymal transition and implications for cancer. Nat Rev Mol Cell Biol. 2019; 20(2): 69-84.
8. Ye X, Weinberg RA. Epithelial-mesenchymal plasticity: a central regulator of cancer progression. Trends Cell Biol. 2015; 25(11): 675-686.
9. Brower JV, Amini A, Chen S, Hullett CR, Kimple RJ, Wojcieszynski AP, et al. Improved survival with dose-escalated radiotherapy in stage III non-small-cell lung cancer: analysis of the National Cancer Database. Ann Oncol. 2016; 27(10): 1887-1894.
10. Chandrashekar DS, Bashel B, Balasubramanya SAH, Creighton CJ, Ponce-Rodriguez I, Chakravarthi B, et al. UALCAN: a portal for facilitating tumor subgroup gene expression and survival analyses. Neoplasia. 2017; 19(8): 649-658.
11. Tang Z, Li C, Kang B, Gao G, Li C, Zhang Z. GEPIA: a web server for cancer and normal gene expression profiling and interactive analyses. Nucleic Acids Res. 2017; 45(W1): W98-W102.
12. Schober P, Boer C, Schwarte LA. Correlation coefficients: appropriate use and interpretation. Anesth Analg. 2018; 126(5): 1763-1768.
13. Győrffy B, Surowiak P, Budczies J, Lánczky A. Online survival analysis software to assess the prognostic value of biomarkers using transcriptomic data in non-small-cell lung cancer. PLoS One. 2013; 8(12): e82241.
14. Miller KD, Siegel RL, Lin CC, Mariotto AB, Kramer JL, Rowland JH, et al. Cancer treatment and survivorship statistics, 2016. CA Cancer J Clin. 2016; 66(4): 271-289.
15. Krause M, Dubrovska A, Linge A, Baumann M. Cancer stem cells: Radioresistance, prediction of radiotherapy outcome and specific targets for combined treatments. Adv Drug Deliv Rev. 2017; 109: 63-73.
16. Moding EJ, Kastan MB, Kirsch DG. Strategies for optimizing the response of cancer and normal tissues to radiation. Nat Rev Drug Discov. 2013; 12(7): 526-542.
17. Shibue T, Weinberg RA. EMT, CSCs, and drug resistance: the mechanistic link and clinical implications. Nat Rev Clin Oncol. 2017; 14(10): 611-629.
18. Marcucci F, Stassi G, De Maria R. Epithelial-mesenchymal transition: a new target in anticancer drug discovery. Nat Rev Drug Discov. 2016; 15(5): 311-325.
19. Choi YJ, Baek GY, Park HR, Jo SK, Jung U. Smad2/3-regulated expression of DLX2 is associated with radiation-induced epithelial-mesenchymal transition and radioresistance of A549 and MDA-MB-231 human cancer cell lines. PLoS One. 2016; 11(1): e0147343.
20. Lu J, Zhong Y, Chen J, Lin X, Lin Z, Wang N, et al. Radiation enhances the epithelial- mesenchymal transition of A549 cells via miR3591-5p/USP33/PPM1A. Cell Physiol Biochem. 2018; 50(2): 721-733.
21. Ogata T, Teshima T, Inaoka M, Minami K, Tsuchiya T, Isono M, et al. Carbon ion irradiation suppresses metastatic potential of human non-small cell lung cancer A549 cells through the phosphatidylinositol-3-kinase/Akt signaling pathway. J Radiat Res. 2011; 52(3): 374-379.
22. Lamouille S, Xu J, Derynck R. Molecular mechanisms of epithelial-mesenchymal transition. Nat Rev Mol Cell Biol. 2014; 15(3): 178-196.
23. Theveneau E, Mayor R. Cadherins in collective cell migration of mesenchymal cells. Curr Opin Cell Biol. 2012; 24(5): 677-684.
24. Yang F, Sun L, Li Q, Han X, Lei L, Zhang H, et al. SET8 promotes epithelial-mesenchymal transition and confers TWIST dual transcriptional activities. EMBO J. 2012; 31(1): 110-123.
25. Yang MH, Hsu DS, Wang HW, Wang HJ, Lan HY, Yang WH, et al. Bmi1 is essential in Twist1-induced epithelial-mesenchymal transition. Nat Cell Biol. 2010; 12(10): 982-992.
26. Yang MH, Wu MZ, Chiou SH, Chen PM, Chang SY, Liu CJ, et al. Direct regulation of TWIST by HIF-1alpha promotes metastasis. Nat Cell Biol. 2008; 10(3): 295-305.
27. Araki K, Shimura T, Suzuki H, Tsutsumi S, Wada W, Yajima T, et al. E/N-cadherin switch mediates cancer progression via TGF-β-induced epithelial-to-mesenchymal transition in extrahepatic cholangiocarcinoma. Br J Cancer. 2011; 105(12): 1885-1893.
28. Gravdal K, Halvorsen OJ, Haukaas SA, Akslen LA. A switch from E-cadherin to N-cadherin expression indicates epithelial to mesenchymal transition and is of strong and independent importance for the progress of prostate cancer. Clin Cancer Res. 2007; 13(23):

7003-7011.
29. Hui L, Zhang S, Dong X, Tian D, Cui Z, Qiu X. Prognostic significance of twist and N-cadherin expression in NSCLC. PLoS One. 2013; 8(4): e62171.
30. Tran PT, Shroff EH, Burns TF, Thiyagarajan S, Das ST, Zabuawala T, et al. Twist1 suppresses senescence programs and thereby accelerates and maintains mutant Kras-induced lung tumorigenesis. PLoS Genet. 2012; 8(5): e1002650.
31. Chen C, Zhao S, Karnad A, Freeman JW. The biology and role of CD44 in cancer progression: therapeutic implications. J Hematol Oncol. 2018; 11(1): 64.
32. Jiang H, Zhao W, Shao W. Prognostic value of CD44 and CD44v6 expression in patients with non-small cell lung cancer: meta-analysis. Tumour Biol. 2014; 35(8): 7383-7389.
33. Hirata T, Fukuse T, Naiki H, Hitomi S, Wada H. Expression of CD44 variant exon 6 in stage I non-small cell lung carcinoma as a prognostic factor. Cancer Res. 1998; 58(6): 1108-1110.
34. Luo Z, Wu RR, Lv L, Li P, Zhang LY, Hao QL, et al. Prognostic value of CD44 expression in non-small cell lung cancer: a systematic review. Int J Clin Exp Pathol. 2014; 7(7): 3632-3646.
35. Leung EL, Fiscus RR, Tung JW, Tin VP, Cheng LC, Sihoe AD, et al. Non-small cell lung cancer cells expressing CD44 are enriched for stem cell-like properties. PLoS One. 2010; 5(11): e14062.
36. Louderbough JM, Schroeder JA. Understanding the dual nature of CD44 in breast cancer progression. Mol Cancer Res. 2011; 9(12): 1573-1586.
37. Fuchs K, Hippe A, Schmaus A, Homey B, Sleeman JP, Orian-Rousseau V. Opposing effects of high- and low-molecular weight hyaluronan on CXCL12-induced CXCR4 signaling depend on CD44. Cell Death Dis. 2013; 4(10): e819.
38. Zhang H, Brown RL, Wei Y, Zhao P, Liu S, Liu X, et al. CD44 splice isoform switching determines breast cancer stem cell state. Genes Dev. 2019; 33(3-4): 166-179.
39. Zhao S, Chen C, Chang K, Karnad A, Jagirdar J, Kumar AP, et al. CD44 expression level and isoform contributes to pancreatic cancer cell plasticity, invasiveness, and response to therapy. Clin Cancer Res. 2016; 22(22): 5592-5604.

Original Article

The Global mRNA Expression Profiles of Inhibiting PHGDH Induced Cisplatin Resistance in Gastric Cancer

Kailing Pan, M.Sc., Xiaoya Zhao, M.Sc., Wenxia Xu, Ph.D.*

Central Laboratory, Affiliated Jinhua Hospital, Zhejiang University School of Medicine, Jinhua, Zhejiang Province, China

**Corresponding Address: Central Laboratory, Affiliated Jinhua Hospital, Zhejiang University School of Medicine, Jinhua, Zhejiang Province, China*
Email: xuwenxia@zju.edu.cn

Received: 15/April/2021, Accepted: 27/July/2021

Abstract

Objective: Drug resistance is the main hindrance to improve the prognosis of patients with gastric cancer. Amino acid metabolic reprograming is essential to satisfy the different requirements of cancer cells during drug resistance, of which serine deprivation could promote resistance to cisplatin in gastric cancer. As the key enzyme in the de novo biosynthesis of serine, phosphoglycerate dehydrogenase (PHGDH) inhibition could also induce cisplatin resistance in gastric cancer. This study aims to reveal the potential mechanisms of drug resistance induced by PHGDH inhibition via exploring the global mRNA expression profiles.

Materials and Methods: In this experimental study, the viability and the apoptotic rate of gastric cancer cells were evaluated by using Cell Counting Kit-8 (CCK-8) analysis and flow cytometric determination, respectively. The identification of differentially expressed genes (DEGs) was tested by mRNA-sequencing (mRNA-Seq) analysis. The confirmation of sequencing results was verified using real-time quantitative reverse transcription polymerase chain reaction (RT-qPCR).

Results: The inhibition of PHGDH significantly increased the viability and decreased the apoptotic rate induced by cisplatin in gastric cancer cells. mRNA-Seq analysis revealed that the combined treatment of NCT503 reduced the number of DEGs induced by cisplatin. Gene Ontology (GO), Kyoto Encyclopedia of Genes and Genomes (KEGG) and Gene Set Enrichment Analysis (GSEA) showed that unfolded protein response, ECM receptor interaction and cell cycle signaling pathways were modulated by NCT503 treatment. Hub genes were identified by using protein-protein interaction network modeling, of which E1A binding protein p300 (EP300) and heat shock protein family A (Hsp70) member 8 (HSPA8) act as the vital genes in cisplatin resistance induced by the inhibition of PHGDH.

Conclusion: These findings suggested that the inhibition of PHGDH promoted cisplatin resistance in gastric cancer through various intercellular mechanisms. And appropriate serine supplementation or the modulation of EP300 and HSPA8 may be of great help in overcoming cisplatin resistance in gastric cancer.

Keywords: Cisplatin, Drug Resistance, Gastric Cancer, Phosphoglycerate Dehydrogenase

Cell Journal(Yakhteh), Vol 24, No 9, September 2022, Pages: 531-539

Citation: Pan K, Zhao X, Xu W. The global mRNA expression profiles of inhibiting PHGDH induced cisplatin resistance in gastric cancer. Cell J. 2022; 24(9): 531-539. doi: 10.22074/cellj.2022.8046.

Introduction

Gastric cancer is the leading cause of cancer death worldwide, with the fifth-highest incidence and third-highest mortality (1). Due to its late detection, aggressive characteristic and poor response to available therapies, gastric cancer displays a poor prognosis. Chemotherapy is the standard first-line treatment for patients with advanced gastric cancer (2). And cisplatin is one of the most widely used chemotherapeutic drugs inducing DNA double-strand break and finally leads to cell apoptosis (3). However, the development of drug resistance in gastric cancer is still a hindrance of cisplatin to effective cancer treatment (4). Therefore, understanding the molecular mechanisms that control cisplatin resistance in gastric cancer is imperative and important for the establishment of new strategies in its clinical treatment.

The mechanisms of drug resistance in gastric cancer involves decreased drug uptake, increased drug efflux, enhanced DNA damage repair, epigenetic modifications changes, autophagy and metabolic reprogramming (5-8). Metabolic reprogramming, which is essential to satisfy the different requirements of cancer cells during tumorigenesis, invasion and resistance to drug therapy, is one of the significant characteristics of cancers (9, 10). Recently, serine/glycine metabolism has attracted more attention. Our previous study demonstrated that the deprivation of serine could promote resistance to cisplatin in gastric cancer. And the inhibition of phosphoglycerate dehydrogenase (PHGDH), the first and only rate-limiting enzyme of serine biosynthesis pathway (SSP), could promote cisplatin resistance and attenuate DNA damage induced by cisplatin in gastric cancer cells (11). However, the specific mechanisms of inhibiting PHGDH promoted cisplatin resistance in gastric cancer remain unclear.

Transcriptomics analysis can reflect the gene expression information of cells in different conditions quickly and comprehensively (12). Due to the advantages such as low background signals, the accurate quantification of expression levels, and RNA sequencing can provide us deep insight into the

regulation mechanisms of specific factors on cells. To clarify the intracellular mechanism changes induced by PHGDH inhibition, we used RNA-Seq analysis to reveal gene expression patterns.

On the basis of our previous study that serine deprivation promotes cisplatin resistance in gastric cancer, here, through RNA-Seq analysis combined with cell functional validation, we gained a comprehensive and detailed understanding of the mechanisms of PHGDH inhibition-induced cisplatin resistance in gastric cancer. Our data provided possible mechanisms for understanding the cisplatin resistance in gastric cancer.

Materials and Methods

Reagents

In this experimental study, human gastric cancer cell lines SGC7901 and MGC803 was obtained from the Type Culture Collection of the Chinese Academy of Sciences (Shanghai, China). The following reagents were used in this research: RPMI-1640 medium (31800-105) from Gibco (Grand Island, New York, USA). Cell Counting Kit-8 agent (CCK-8, C0042) from Beyotime (Shanghai, China). Penicillin streptomycin solution (GNM15140) and trypsin (GNM25200) from Genome (Hangzhou, Zhejiang, China). Fetal bovine serum (11011-8611) from Every Green (Hangzhou, China). NCT-503 (HY-101966) from MedChemExpression (Shanghai, China). TRIzon reagent (CW0580) from Cwbio (Beijing, China).

Cell culture

SGC7901 and MGC803 were cultured at 37°C in an atmosphere of 5% CO_2. All cells were kept in RPMI-1640 medium, supplemented with 100 mg/mL streptomycin, 100 U/mL penicillin and 10% fetal bovine serum.

Cell viability

Cells were plated at a density of 1×10^4 cells per well onto 96-well plates. These cells were divided into 2 groups (control group and cisplatin treatment group). Then, each group was subdivided into 4 groups (treated with 0, 1, 10 or 50 μM NCT503, respectively) and each concentration has 3 repeats. After 24 hours, cells were treated with cisplatin combined with different concentrations of NCT503 for 24 h. Then 100 μL medium containing 10 μL CCK-8 was added after discarding the supernatant and reacted at 37°C for 1 hour. The optical density values at 450 nm which reflect the viability of cells were determined using a Microplate Reader (Synergy HTZX-22; Bio-Tek Instruments, USA).

Cell apoptosis

Cells were plated onto 6-well plates at a density of 70-80% for 24 hours. Cells were divided into four groups: Control (CN), Cisplatin (DDP), NCT503 (NCT) and Cisplatin combined with NCT503 (CB). The cells were treated with vehicles, 1.2 μg/mL cisplatin, 50 μM NCT503 and 1.2 μg/mL cisplatin combined with 50 μM NCT503 respectively. Among which each group was set to three biological replicates. After 24 hours, cells including floating and adherent were collected. Then 300 μL Annexin V-FITC binding reagent containing 6 μL propidium iodide (PI) and 3 μL Annexin V-FITC (C1062L, Beyotime Biotechnology, China) was added and reacted at 37°C for 15 minutes. The apoptotic rate was measured using a Flow cytometer (EasyCell 204A1/206A1, Wellgrow, China).

Real-time quantitative reverse transcription polymerase chain reaction

The total cellular RNA was extracted using TRIzon reagent and cDNAs were synthesized using PrimeScript™ RT Master Mix (RR036A, Takara). Real-time PCR was performed using SYBR Green Realtime PCR Master Mix (RR430, Takara) and Cobas z 480 (Roche, Basel, Switzerland). The primers for HSPA8, EP300, ras homolog family member A (*RHOA*), RNA polymerase II subunit C (*POLR2C*) and *β-ACTIN* were synthesized by TSINGKE Biological Technology (Beijing, China). β-actin was served as an internal reference of RNA integrity. The sequences are as following:

HSPA8-

F: 5′- ATGGTGCAGCTGTCCAG-3′
R: 5′- ACAGTCATGACTCCACCAG-3′

EP300-

F: 5′- ATGGCACAGATTTTGGCTCTC-3′
R: 5′- TACCAGATCGCAGCAATTCTGAC-3′

RHOA-

F: 5′- ATGGAAAGCAGGTAGAGTTGGC-3′
R: 5′- ACTATCAGGGCTGTCGATGG-3′

POLR2C-

F: 5′- GCTCACAGGCTTGGATTAATTCC-3′
R: 5′- ATGTGCAGTCCCGAGAGTACTG-3′

β-ACTIN-

F: 5′-ACTCTTCCAGCCTTCCTTCC-3′
R: 5′-CGTCATACTCCTGCTTGCTG-3′

Total RNA extraction and transcriptome sequencing

Total RNA was enriched by Oligo (dT) and then fractured into short pieces using Fragmentation buffer. The double-stranded cDNA was synthesized and purified. The cDNA was then repaired, added with base A and a sequencing adapter. The target size fragments are recovered by agarose gel electrophoresis and PCR amplification is performed to construct the sample library. Finally, the constructed library was detected on the Illumina platform. Sequencing analysis was conducted

by JiGuang Gene (Nanjing, China).

Bioinformatics analyses

Transcripts Per Million (TPM) was used to represent gene expression levels (13). Limma was used to normalize the data and the DEGs were visualized by ggplot2 and pheatmap packages (14). The threshold of DEGs was set to P<0.05 and |logFC|>1. ClusterProfiler package was used to perform GO (http://www.geneontology.org/) and KEGG (http://www.genome.jp/kegg/) pathway analyses based on DEGs. And the results were visualized by GOplot and ggplot2 packages (15). GSEA analysis was performed using GSEA software (v. 4.1.0). The PPI analysis was produced in STRING website (https://string-db.org/), and the results were subjected into Cytoscape (https://www.cytoscape.org). Then MCODE, a Cytoscape plugin, was used to find clusters in the network. The clusters, whose score >8, were subjected to ClueGo for GO and KEGG analysis. Finally, hub genes were predicted by cytoHubba. The prognostic values of these hub genes were assessed with the Kaplan-Meier Plotter tool (http://kmplot.com).

Statistical analysis

All data were processed by GraphPad Prism 9 for Mac (GraphPad Prism Software Inc., San Diego, CA, USA). Differences between two groups were evaluated by the unpaired two-tailed student's t test. One-way analysis of variance (ANOVA) was used to assess differences between multiple groups. Data are presented in the form of mean ± standard deviation (SD). P<0.05 denotes statistical significance.

Statement of ethics

The design and the protocols of the experiments have been reviewed and approved by the Medical Ethics Committee of Jinhua Central Hospital (No. 2020-205-001).

Results

The inhibition of PHGDH promoted cisplatin resistance in gastric cancer

To verify the effect of PHGDH in cisplatin resistance in gastric cancer. We treated SGC7901 and MGC803 cells with differential concentrations of NCT503, an inhibitor of PHGDH, combined cisplatin. The results showed that the inhibition of PHGDH slightly decreased the viability of MGC803 cells. And the treatment of cisplatin impaired the viability of both SGC7901 and MGC803 cells. However, the cell viability was significantly increased by the combined treatment of NCT503 and cisplatin compared to cisplatin-treated cells, especially in SGC7901 cells. And a high concentration of NCT503 correlated with a high cell viability (Fig.1A, B). We further examined the apoptosis rate in SGC7901 cells due to the significant response of SGC7901 to NCT503. The results showed that the treatment of cisplatin significantly promoted cell apoptosis, and the inhibition of PHGDH partially reversed the process of cell apoptosis (Fig.1C, D). Together, our results demonstrated that the inhibition of PHGDH promoted cisplatin resistance in gastric cancer.

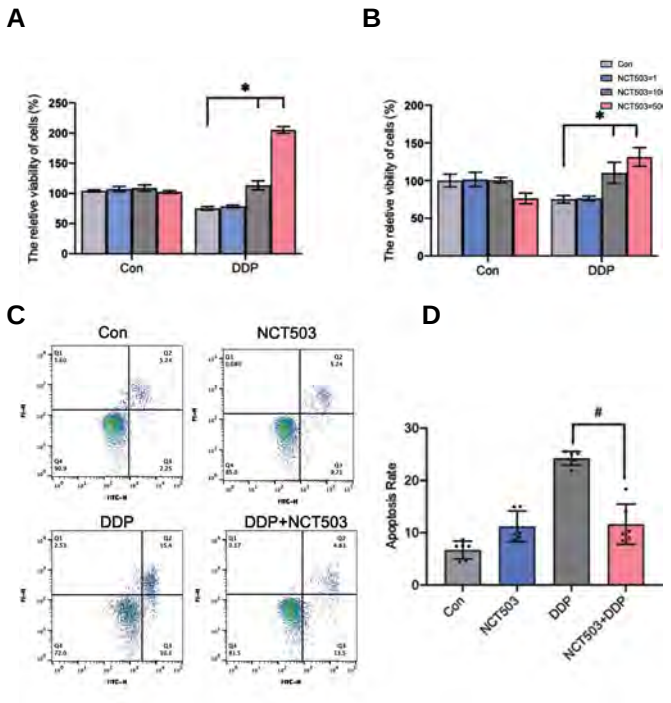

Fig.1: The inhibition of PHGDH promoted cisplatin resistance in gastric cancer. **A.** Cell viability in SGC7901 cells with vehicles or 1.2 μg/ml cisplatin under the treatment of different concentration of NCT503 (0, 1,10, 50 μM, n=3). **B.** Cell viability in MGC803 cells with vehicles or 3.0 μg/ml cisplatin under the treatment of different concentration of NCT503 (0, 1, 10, 50 μM, n=3). **C, D.** Flow cytometric determination of cell apoptosis rate in SGC7901 cells with vehicles, 50 μM NCT503, 1.2 μg/ml cisplatin or the combination of NCT503 with cisplatin (n=3). *; P<0.05, compared to control group and #; P<0.05, compared to DDP group, PHGDH; Phosphoglycerate dehydrogenase, and DDP; Cisplatin.

Identification of DEGs in NCT503-induced cisplatin resistance

To fully understand the potential molecular mechanisms of NCT503-induced cisplatin resistance, we divided SGC7901 cells into four groups: control group (CN), cisplatin-treated group (DDP), NCT503-treated group (NCT) and cisplatin combined with NCT503 treated group (CB), and carried out a series evaluation using RNA-Seq.

The DEGs was selected according to the criteria of P<0.05 and |log FC|>1. The integral gene expression variation between each group were visualized by volcano plots. The results showed that after treatment with cisplatin, a total of 3240 genes displayed differential expression, including 1467 upregulated genes and 1773 downregulated genes (Fig.2Aa). The inhibition of PHGDH led to 468 DEGs, within 179 upregulated genes and 289 downregulated genes (Fig.2Ab). In addition, the combination treatment of NCT503 significantly reduced the number of DEGs caused by cisplatin and just 2031

genes showed significantly difference (Fig.2Ac). A comparative analysis between CB group and DDP group showed that 411 genes were significantly different, of which 196 genes upregulated and 215 one down regulated (Fig.2Ad). Heatmaps were used to reflect the differences and clustering between different groups (Fig.2B).

Since the combination use of NCT503 significantly reduced the number of DEGs caused by cisplatin, these genes that no longer have significant differences may be the key genes that promote cisplatin resistance in gastric cancer. Therefore, we analyzed the DEGs between CB group and DDP group. The result showed that 1582 genes were no longer significantly different after NCT503 combined treatment, and 373 genes significantly changed on the basis of cisplatin treatment (Fig.2C).

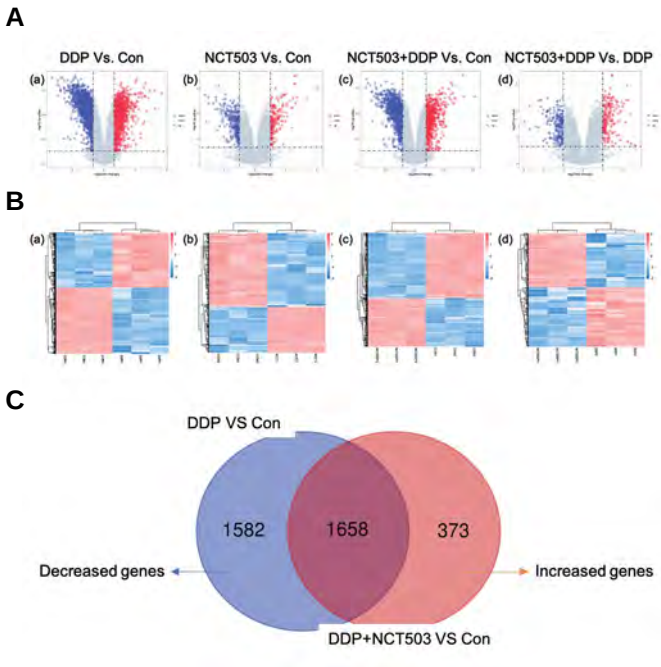

Fig.2: Identification of DEGs in NCT503-induced cisplatin resistance. **A.** Volcano plots showing the gene expression alterations between different drug treatment groups. Blue dots and red dots represent downregulated genes and upregulated genes, respectively. **B.** Heat maps of significantly differentially expressed genes between each group. **C.** Venn diagram showing common regulated genes shared between cisplatin induced DEGs and the combination of cisplatin with NCT503 induced DEGs. DEGs; Differentially expressed genes, DDP; Cisplatin, and Con; Control.

GO analysis revealed the related biological processes

To further demonstrate the mechanisms induced by the inhibition of PHGDH, GO enrichment analysis was conducted. GO analysis includes cellular component (CC), biological process (BP) and molecular function (MF), of which BP analysis can reveal the BP that the DEGs participated in. Circle plot was used to visualize the GO-BP analysis, in which upregulated genes were red and downregulated genes were blue. In DDP group, we found that the genes related with cell-substrate adhesion and extracellular matrix organization were downregulated, and the genes related to cell cycle arrest were upregulated (Fig.3A). After the inhibition of PHGDH, the genes related to cellular response to unfolded protein (UPR) and response to endoplasmic reticulum stress (ERS) upregulated (Fig.3B). Also the treatment of NCT503 combined with cisplatin downregulated extracellular structure organization related genes, and upregulated *UPR* related genes (Fig.3C). In addition, compared with DDP group, the CB group upregulated *UPR* related genes (Fig.3D). Our results indicated that the BP of *UPR* may be the key of NCT503-induced cisplatin resistance in gastric cancer cells.

To confirm the effect of *UPR* in gastric cisplatin resistance, we performed GO-BP analysis on the reduced DEGs in CB group compared to DDP group. The result showed that these genes were related to protein folding and ribosome biogenesis, which promote protein expression (Fig.3E). And the increased DEGs in CB group were related to *UPR* (Fig.3F). Under the treatment of drugs, misfolded and unfolded proteins in cells accumulate in the endoplasmic reticulum, thereby inducing ERS. Cells can initiate UPR to restore cell homeostasis by reducing the rate of protein synthesis, activating ER-related degradation and other mechanisms (16). Therefore, we hypothesized that cisplatin promoted cell apoptosis through the accumulation of misfolded proteins and NCT503 promote cisplatin resistance through activating the BP of UPR to balance cell homeostasis.

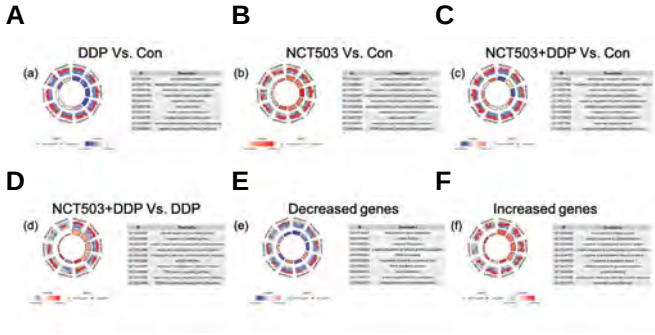

Fig.3: GO analysis revealed the related biological processes. The top 10 GO-BP annotations of the DEGs are shown. **A.** GO analysis of DEGs between DDP group and CN group, **B.** GO analysis of DEGs between NCT group and CN group, **C.** GO analysis of DEGs between CB group and CN group, **D.** GO analysis of DEGs between CB group and DDP group, **E.** GO analysis of the decreased DEGs between CB group and DDP group, **F.** GO analysis of the increased DEGs between CB group and DDP group. Red dots represent upregulated genes; blue dots represent downregulated genes. The gradual size and color of rectangles in the middle represents the adjust P value and the regulation of genes in the enriched biological process, respectively. GO; Gene Ontology, BP; Biological process, DEGs; Differentially expressed genes, DDP; Cisplatin, NCT; NCT503, CB; Cisplatin combined with NCT503, and CN; Control.

KEGG and GSEA enrichment revealed the related signaling pathways

To further reveal the potential signaling pathway of NCT503-mediated cisplatin resistance, we performed KEGG pathway enrichment analysis. The results showed that cisplatin is mainly involved in the regulation of P53 signaling pathway, adherens junction and Apoptosis

(Fig.4Aa). NCT503 affects the P53 signaling pathway, IL-17 signaling pathway and Protein processing in ER (Fig.4Ab). The combination treatment of NCT503 and cisplatin regulated P53 signaling pathway, Adherens junction and TNF signaling pathway (Fig.4Ac). In addition, NCT503 combination mainly influenced Glycine, serine and threonine metabolism, Biosynthesis of amino acid and Protein processing in ER compared to cisplatin-treated group (Fig.4Ad). And after the combination of NCT503, the genes no longer have significant differences were related to Proteasome and Cell cycle pathway, and the genes changed were related to TNF signaling pathway (Fig.4A-e, f). Together, our results showed that both cisplatin and NCT503 could modulate P53 signaling pathway, and the combination of NCT503 could restore the expression of cell cycle related proteins, at the same time affect TNF signaling pathway and Protein processing in endoplasmic reticulum.

The intracellular signaling pathway is often amplified by signal cascades, and slight changes in upstream signal molecules that can also cause significant changes in downstream genes. Therefore, pathway enrichment analysis based on DEGs often fails to capture the overall signaling pathways changed in the cell. GSEA, which bases on the whole genes obtained by RNA-Seq, overcome this shortcoming perfectly. We used GSEA to analyze the effect of PHGDH inhibition on cisplatin resistance. The results showed that, consistent with GO and KEGG analysis, cisplatin treatment resulted in the downregulation of Adherens junction and ECM receptor interaction (Fig.4Ba, b). In addition, compared with DDP group, the combination of NCT503 upregulated genes related to Adherens junction and ECM receptor interaction (Fig.4Ca, b). And NCT503 combination also upregulated Mismatch repair and VEGF signaling pathway (Fig.4Cc, d). Altogether, our results showed that NCT503 promoted cisplatin resistance in gastric cancer cells by restoring Adherens junction and ECM receptor interaction and promoting Mismatch repair and VEGF signaling pathway.

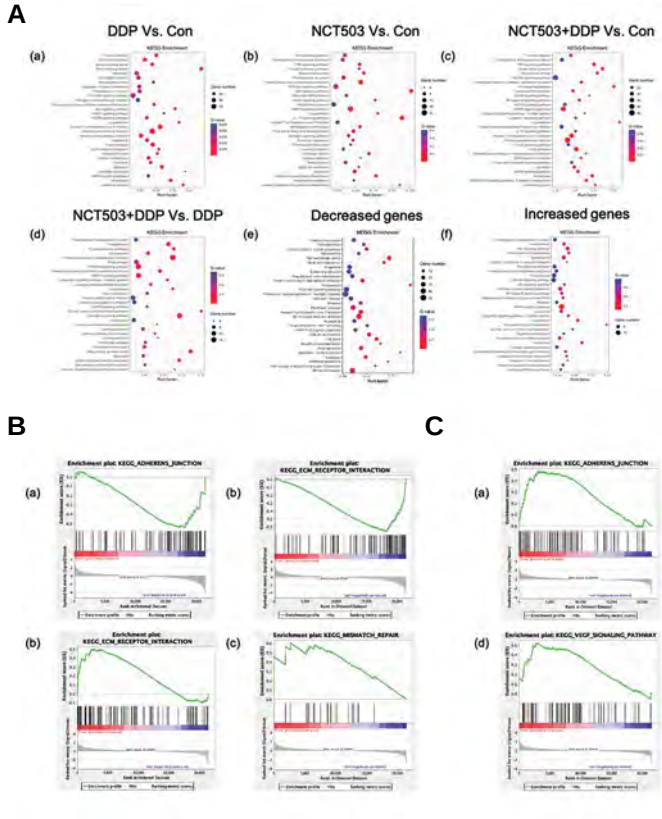

Fig.4: KEGG and GSEA enrichment revealed the related signaling pathways. **A.** KEGG pathway enrichment analysis of DEGs. The gradual color represents the Q value, and the size of the black spots represents the gene number enriched in this pathway. **B.** GSEA analysis of detected genes between DDP group and CN group. **C.** GSEA analysis of detected genes between CB group and DDP group. KEGG; Kyoto Encyclopedia of Genes and Genomes, GSEA; Gene Set Enrichment Analysis, DEGs; Differentially expressed genes, CN; Control, CB; Cisplatin combined with NCT503, and DDP; Cisplatin.

Protein-protein interactions networks analysis

Proteins function often based on the protein-protein interactions which is essential for almost all biochemical activities. For deeply understanding the regulatory mechanisms in NCT503-induced cisplatin resistance in gastric cancer cells, we performed PPI analysis based on DEGs between DDP group and CB group. STRING was used to construct the PPI network, in which the network with the highest confidence score (0.9) was selected and imported into Cytoscape for functional enrichment analysis (Fig.5A). MCODE plugin was used to find clusters in the network (Fig.5B). Then the top highly interconnected cluster was dissected using ClueGo. The result of GO-BP analysis showed that the cluster predominantly involved UPR and Negative regulation of inclusion body assembly (Fig.5C). And pathway enrichment analysis showed that this cluster was related to Antigen processing and presentation and Protein processing in ER (Fig.5D).

Hub genes play vital roles in BP that the other genes often affected by these genes in related pathways. Thus, we screened the hub genes, that modulated NCT503-mediated cisplatin resistance in gastric cancer cells, using cytoHubba. The 10 highest scoring genes were shown in Figure 5E, of which the genes associated with UPR including heat shock protein family A (Hsp70) member 5 (HSPA5), HSPA8 and heat shock protein family A (Hsp70) member 1A (HSPA1A) were screened.

Considering the combination of NCT503 reduced the number of DEGs induced by cisplatin. We also performed PPI analysis using these reduced DEGs. The PPI network and the highest clusters were shown in Figure 5F, G and S1 (See Supplementary Online Information at www.celljournal.org). Figure 1A-C. For GO-BP analysis, these clusters were mainly focused on mRNA export from nucleus and positive regulation of viral transcription (Fig.5H). For KEGG analysis, there were mainly related to Spliceosome, Ubiquitin mediated proteolysis and mRNA surveillance pathway (Fig.5I). In addition, the hub gens including RHOA, EP300 and POLR2C were screened by using cytoHubba (Fig.5J).

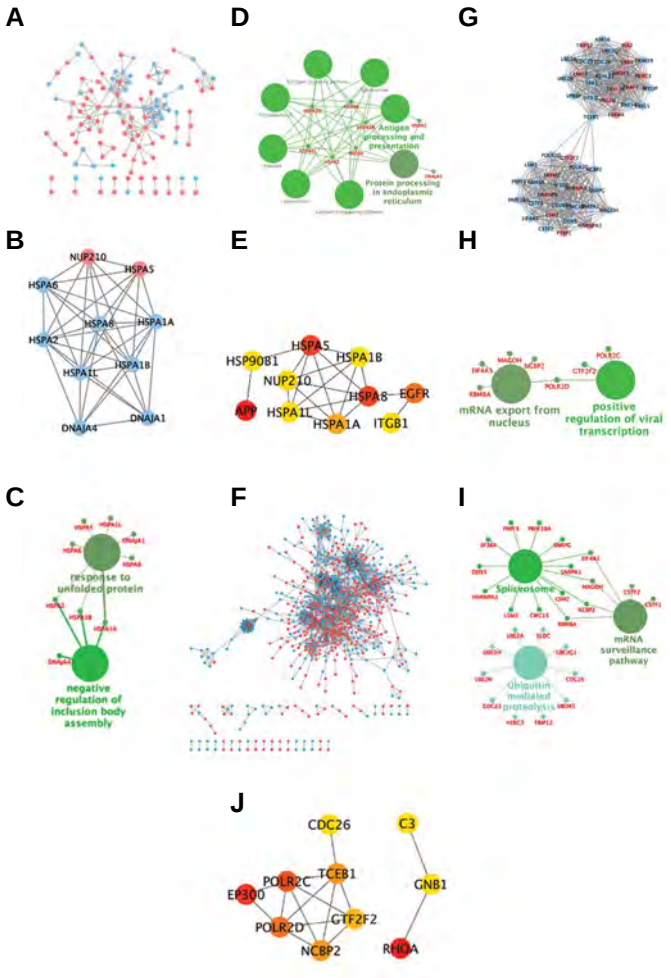

Fig.5: PPI networks analysis. **A.** PPI network of DEGs between CB group and DDP group. Red nodes represent upregulated genes; blue nodes represent downregulated genes. **B.** The most highly connected module identified by MCODE. **C-D.** GO and KEGG analysis of the module by ClueGo. **E.** The top 10 hub genes of DEGs identified by cytoHubba. **F.** PPI network of DEGs decreased by the combination of NCT503 compared to the cisplatin induced DEGs. **G.** The most highly connected module. **H-I.** GO and KEGG analysis of the module. **J.** The top 10 hub genes of DEGs. PPI; Protein-protein interactions, DEGs; Differentially expressed genes, CB; Cisplatin combined with NCT503, DDP; Cisplatin, GO; Gene Ontology, and KEGG; Kyoto Encyclopedia of Genes and Genomes.

Validation of hub genes

The prognostic significance of the 20 hub genes in gastric cancer patients was investigated using the Kaplan-Meier Plotter tool. All of these genes were found to be significantly associated with both overall survival (OS) and first progression (FP) that 19 genes were significantly associated with post progression survival (PPS). As show in Figure 6A-C, 11 of them were protective factors for prognosis (HR<1), whereas 9 were risk factors for prognosis (HR>1).

Among the 20 genes, four genes showed the most significant prognostic value for OS, FP or PPS (HSPA8 and POLR2C for OS, RHOA and POLR2C for FP, HSPA8 and EP300 for PPS). Therefore, we examined the expression level of the four hub genes (HSPA8, RHOA, POLR2C and EP300) by RT-qPCR in SGC7901 cells. The results showed that cisplatin treatment upregulated POLR2C expression, downregulated HSPA8 and EP300 expressions, the combined usage of NCT503 reversed the changes of HSPA8 and EP300 induced by cisplatin (Fig.6D). Our results showed that the inhibition of PHGDH could reverse the expression model of HSPA8 and EP300 to promote cisplatin resistance in gastric cancer cells.

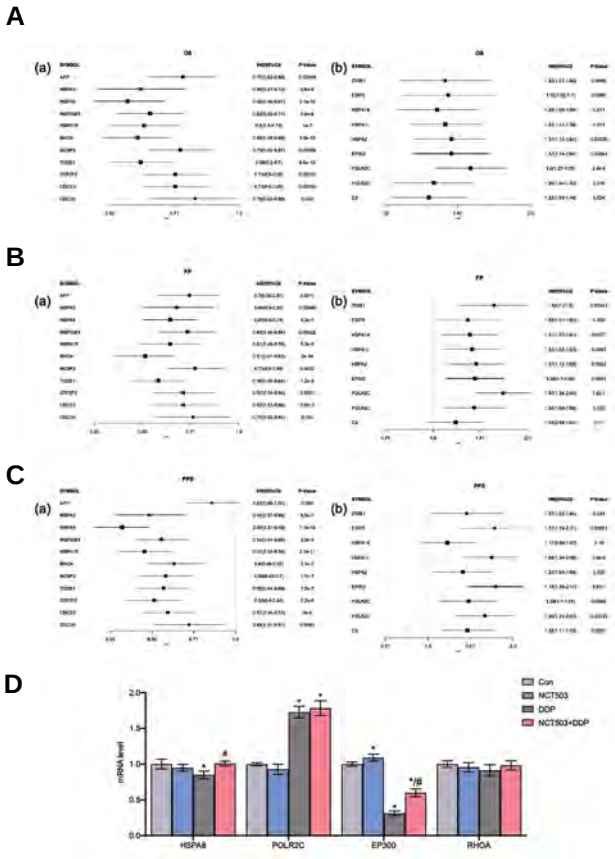

Fig.6: Validation of hub genes. **A-C.** OS, FP and PPS of hub genes, among which the genes on the left forest plots represents prognostic protective genes and the right represents prognostic risk genes. **D.** The mRNA levels of HSPA8, POLR2D, RHOA and EP300 in different groups. The $2^{-\Delta\Delta Ct}$ method was used to determine the relative expression levels (n=6). *; P<0.05. Compared to control group, #; P<0.05. Compared to DDP group. OS; Overall survival, FP; First progression, PPS; Post progression survival, and DDP; Cisplatin.

Discussion

Emerging evidence suggests that SSP is closely associated to cancer progression. Tumor needs numerous nutrients to sustain its rapid proliferation. Serine provides the necessary precursor for the biosynthesis of other amino acids such as glycine and cysteine and the production of phospholipids such as sphingolipids and phosphatidylserine (17). Serine is synthesized by the glycolytic intermediate 3-phophoglycerate through a three-step enzymatic transformation. As the first and only rate-limiting enzyme of SSP, PHGDH is overexpressed in various types of cancers including breast (18), glioma (19), gastric (20) and so on. And genetic silencing or

inhibition of PHGDH can disrupt the serine synthesis pathway and suppress tumor growth (21). In addition, studies showed that the inhibition of PHGDH could promote drug sensitivity in various cancers [eg, breast (22), hepatocellular carcinoma (23), lung adenocarcinoma (24), melanoma (25), renal cell carcinoma (26) and multiple myeloma (27)]. However, our previous results showed that the combination of PHGDH inhibitors with cisplatin failed to increase drug sensitivity in gastric cancer. On the contrary, the inhibition of PHGDH significantly reduced the cytotoxicity of cisplatin and the addition of extra serine increased the efficacy of cisplatin in gastric cancer cells (11). Therefore, the mechanisms of serine metabolism on the chemotherapy sensitivity of gastric cancer may be different from other cancers. Gaining a good command of the mechanisms of cisplatin resistance induced by PHGDH inhibitors is of importance to overcome the obstacle of drug resistance in gastric cancer.

In this study, high-throughput sequencing was used to detect DEGs in cells treated with different drugs. Compared to control group, the treatment of cisplatin dysregulated the expression levels of 3240 genes. And the combination of NCT503 significantly reduced the number of DEGs to only 2031 dysregulated genes. In order to investigate the key genes and potential mechanisms involved in cisplatin resistance, DEGs were proved to integrative bioinformatic analyses. GO, KEGG and GSEA analyses were used to discover the potential functions of these DEGs.

Cisplatin, which is one of the most commonly used drugs for the treatment of cancers, exerts anticancer activity via the generation of DNA lesion by interacting with purine bases on DNA followed by cell cycle arrest and finally lead to cell apoptosis (3). GO enrichment analysis showed that the top-ranking BP modulated by cisplatin in gastric cancer cells comprised cell-substrate adhesion, extracellular matrix organization and cell cycle arrest, which were in accordance with previous studies (28). Compared to cisplatin treated cells, the combination of NCT503 increased the expression levels of genes related to UPR and ERS and decreased the expression levels of genes related to protein folding and rRNA processing. ER is the pivotal organelle responsible for protein folding. Various intrinsic and extrinsic stresses including hypoxia, dysregulation of calcium metabolism and drugs often disturbed the homeostasis of ER, resulting in accumulation of misfolded protein (29). Cancer cells adapt to this homeostasis imbalance by activating UPR which reduces RNA translation and promote the degradation of misfolded proteins (30). Studies also showed that the activation of UPR could promote tumor growth and drug resistance (31). Here, our results showed that the inhibition of PHGDH could reduce sensitivity to cisplatin in gastric cancer cells and increase the expression levels of UPR-related genes suggesting that the drug resistance induced by PHGDH inhibition may related to the activation of UPR.

KEGG enrichment analysis revealed that NCT503 induced Glycine, serine and threonine metabolism and biosynthesis of amino acid based on the treatment of cisplatin which were consistent with the role of PHGDH in regulating serine biosynthesis. Besides, genes participated in the regulation of proteasome and cell cycle signaling pathways were no longer have significant changes compared to cisplatin group after the combination treatment of NCT503. This indicated that PHGDH inhibition dysregulate the metabolism of amino acid and return the expression levels of genes regulating proteasome and cell cycle to a normal line. GSEA analysis showed that cisplatin decreased the gene expression of adherens junction and ECM receptor interaction but NCT503 reversed the downregulation of these genes. As an important component of tumor microenvironment, ECM is involved in almost all development processes of tumors including tumor growth, apoptosis, drug resistance and invasion (32). The downregulation of adherens junction and ECM receptor interaction could promote cell apoptosis and the inhibition of PHGDH promote drug resistance by restoring the expression levels of the genes related to these two signaling pathways.

The construction of PPI network and further module analysis also verified the role of PHGDH inhibition in promoting ERS and UPR. Finally, hub genes were calculated by using the degree algorithm of cytoHubba, of which HSPA8, RHOA, POLR2C and EP300 were significantly associated to the survival analysis. RT-qPCR analysis showed that the cisplatin-induced downregulation of HSPA8 and EP300 could be reversed by the inhibition of PHGDH. As the pivotal protein of the protein quality control system, HSPA8 participated in a wide variety of cellular processes, including folding and transport of newly synthesized polypeptides, protection of the proteome from stress and activation of proteolysis of misfolded proteins (33-35). Our results suggested that the inhibition of PHGDH maintain cell homeostasis by upregulating the expression of HSPA8. EP300 is a histone acetyltransferase, which regulates transcription via chromatin remodeling that is important in the process of cell proliferation and differentiation (36, 37). It has also been identified as an activator of VEGF (38) explaining the upregulation of VEGF signaling pathway in the CB group revealed by the GSEA analysis. Therefore, the high expression of EP300 may serve as a key regulatory molecule for NCT503-mediated cisplatin resistance in gastric cancer and promote the survival of gastric cancer cells through chromatin remodeling and activation of VEGF signaling pathways.

In summary, our studies showed that the PHGDH inhibition promoted cisplatin resistance in gastric cancer cells and the addition of serine could promote the sensitivity of gastric cancer cells to cisplatin (11). These indicated that the combination of PHGDH inhibitors with cisplatin may not be a good strategy in the treatment of gastric cancer. On the contrary, the supplementation of serine combined with cisplatin may be a candidate therapy. But the effectiveness of the therapy still needs

the support of clinical data.

Mechanically, we found that the inhibition of PHGDH mainly activated *ERS* and *UPR*. And it also involved in restoring the expression levels of genes related to ECM receptor interaction and cell cycle signaling pathways to normal levels. These play important roles in maintaining cell homeostasis and cell survival. In addition, we also found that HSPA and EP300 may be the vital regulatory genes involved in intracellular activities after PHGDH inhibition, respectively regulating UPR and chromatin remodeling. The relationship of PHGDH with HSPA8 and EP300 will be further studied in the follow-up studies.

Conclusion

Via transcriptomics analysis, we found the crucial intercellular mechanisms regulating the cisplatin resistance induced by PHGDH inhibition. PHGDH is the key enzyme for the de novo biosynthesis of serine. Therefore, appropriate serine supplementation or the modulation of EP300 and HSPA8 may be of great help in overcoming cisplatin resistance in gastric cancer.

Acknowledgments

This work was supported by the Jinhua Science and Technology Research Program (2020-3-046); Program of Zhejiang Province Natural Science Foundation (LY21H160014). Foundation for Basic Research of Affiliated Jinhua Hospital, Zhejiang University School of Medicine (JY2020-6-04). The authors have declared that no competing interest exists in this work.

Authors' Contribution

K.P.; Performed all experiments, analyzed the data and wrote the manuscript. X.Z.; Performed cell experiments. W.X.; Contributed to concept and design, financial support, and final approval of the manuscript. All authors read and approved the final manuscript.

References

1. Siegel RL, Miller KD, Jemal A. Cancer statistics, 2019. CA Cancer J Clin. 2019; 69(1): 7-34.
2. Smyth EC, Nilsson M, Grabsch HI, Van Grieken NC, Lordick F. Gastric cancer. Lancet. 2020; 396(10251): 635-648.
3. Ghosh S. Cisplatin: the first metal based anticancer drug. Bioorg Chem. 2019; 88: 102925.
4. Zhang H, Deng T, Liu R, Ning T, Yang H, Liu D, et al. CAF secreted miR-522 suppresses ferroptosis and promotes acquired chemoresistance in gastric cancer. Mol Cancer. 2020; 19(1): 43.
5. Assaraf YG, Brozovic A, Gonçalves AC, Jurkovicova D, Linē A, Machuqueiro M, et al. The multi-factorial nature of clinical multidrug resistance in cancer. Drug Resist Updat. 2019; 46: 100645.
6. Pourhanifeh MH, Vosough M, Mahjoubin-Tehran M, Hashemipour M, Nejati M, Abbasi-Kolli M, et al. Autophagy-related microRNAs: Possible regulatory roles and therapeutic potential in and gastrointestinal cancers. Pharmacol Res. 2020; 161: 105133.
7. Ramezankhani R, Solhi R, Es HA, Vosough M, Hassan M. Novel molecular targets in gastric adenocarcinoma. Pharmacol Ther. 2021; 220: 107714.
8. Shafabakhsh R, Arianfar F, Vosough M, Mirzaei HR, Mahjoubin-Tehran M, Khanbabaei H, et al. Autophagy and gastrointestinal cancers: the behind the scenes role of long non-coding RNAs in initiation, progression, and treatment resistance. Cancer Gene Ther. 2021; 28(12): 1229-1255.
9. Faubert B, Solmonson A, DeBerardinis RJ. Metabolic reprogramming and cancer progression. Science. 2020; 368(6487): eaaw5473.
10. Ohshima K, Morii E. Metabolic reprogramming of cancer cells during tumor progression and metastasis. Metabolites. 2021; 11(1): 28.
11. Zhao X, Fu J, Tang W, Yu L, Xu W. Inhibition of serine metabolism promotes resistance to cisplatin in gastric cancer. Onco Targets Ther. 2020; 13: 4833-4842.
12. Sun J, Wang J, Zhang N, Yang R, Chen K, Kong D. Identification of global mRNA expression profiles and comprehensive bioinformatic analyses of abnormally expressed genes in cholestatic liver disease. Gene. 2019; 7079-7021.
13. Vera Alvarez R, Pongor LS, Mariño-Ramírez L, Landsman D. TPMCalculator: one-step software to quantify mRNA abundance of genomic features. Bioinformatics. 2019; 35(11): 1960-1962.
14. Ritchie ME, Phipson B, Wu D, Hu Y, Law CW, Shi W, et al. limma powers differential expression analyses for RNA-sequencing and microarray studies. Nucleic Acids Res. 2015; 43(7): e47.
15. Walter W, Sánchez-Cabo F, Ricote M. GOplot: an R package for visually combining expression data with functional analysis. Bioinformatics. 2015; 31(17): 2912-2914.
16. Chen X, Cubillos-Ruiz JR. Endoplasmic reticulum stress signals in the tumour and its microenvironment. Nat Rev Cancer. 2021; 21(2): 71-88.
17. Li AM, Ye J. Reprogramming of serine, glycine and one-carbon metabolism in cancer. Biochim Biophys Acta Mol Basis Dis. 2020; 1866(10): 165841.
18. Chandrika M, Chua PJ, Muniasamy U, Huang RYJ, Thike AA, Ng CT, et al. Prognostic significance of phosphoglycerate dehydrogenase in breast cancer. Breast Cancer Res Treat. 2021; 186(3): 655-665.
19. Li M, Wu C, Yang Y, Zheng M, Yu S, Wang J, et al. 3-Phosphoglycerate dehydrogenase: a potential target for cancer treatment. Cell Oncol (Dordr). 2021; 44(3):541-556.
20. Zhang Y, Yang L, Dai G, Cao H. Knockdown of PHGDH potentiates 5-FU cytotoxicity in gastric cancer cells via the Bcl-2/Bax/caspase-3 signaling pathway. Int J Clin Exp Pathol. 2018; 11(12): 5869-5876.
21. Mullarky E, Lucki NC, Beheshti Zavareh R, Anglin JL, Gomes AP, Nicolay BN, et al. Identification of a small molecule inhibitor of 3-phosphoglycerate dehydrogenase to target serine biosynthesis in cancers. Proc Natl Acad Sci USA. 2016; 113(7): 1778-1783.
22. Zhang X, Bai W. Repression of phosphoglycerate dehydrogenase sensitizes triple-negative breast cancer to doxorubicin. Cancer Chemother Pharmacol. 2016; 78(3): 655-659.
23. Wei L, Lee D, Law CT, Zhang MS, Shen J, Chin DW, et al. Genome-wide CRISPR/Cas9 library screening identified PHGDH as a critical driver for Sorafenib resistance in HCC. Nat Commun. 2019; 10(1): 4681.
24. Dong JK, Lei HM, Liang Q, Tang YB, Zhou Y, Wang Y, et al. Overcoming erlotinib resistance in EGFR mutation-positive lung adenocarcinomas through repression of phosphoglycerate dehydrogenase. Theranostics. 2018; 8(7): 1808-1823.
25. Ross KC, Andrews AJ, Marion CD, Yen TJ, Bhattacharjee V. Identification of the serine biosynthesis pathway as a critical component of BRAF inhibitor resistance of melanoma, pancreatic, and non-small cell lung cancer cells. Mol Cancer Ther. 2017; 16(8): 1596-1609.
26. Yoshino H, Nohata N, Miyamoto K, Yonemori M, Sakaguchi T, Sugita S, et al. PHGDH as a key enzyme for serine biosynthesis in HIF2α-targeting therapy for renal cell carcinoma. Cancer Res. 2017; 77(22): 6321-6329.
27. Zaal EA, Wu W, Jansen G, Zweegman S, Cloos J, Berkers CR. Bortezomib resistance in multiple myeloma is associated with increased serine synthesis. Cancer Metab. 2017; 5(7).
28. Bao A, Li Y, Tong Y, Zheng H, Wu W, Wei C. 1,25-Dihydroxyvitamin D3 and cisplatin synergistically induce apoptosis and cell cycle arrest in gastric cancer cells. Int J Mol Med. 2014; 33(5): 1177-1184.
29. Sontag EM, Samant RS, Frydman J. Mechanisms and Func-

tions of spatial protein quality control. Annu Rev Biochem. 2017; 86: 97-122.
30. Chen L, Brewer MD, Guo L, Wang R, Jiang P, Yang X. Enhanced degradation of misfolded proteins promotes tumorigenesis. Cell Rep. 2017; 18(13): 3143-3154.
31. Chen CY, Kawasumi M, Lan TY, Poon CL, Lin YS, Wu PJ, et al. Adaptation to endoplasmic reticulum stress enhances resistance of oral cancer cells to cisplatin by up-regulating polymerase η and increasing DNA repair efficiency. Int J Mol Sci. 2020; 22(1): 355.
32. Mohan V, Das A, Sagi I. Emerging roles of ECM remodeling processes in cancer. Semin Cancer Biol. 2020; 62: 192-200.
33. Bonam SR, Ruff M, Muller S. HSPA8/HSC70 in Immune disorders: a molecular rheostat that adjusts chaperone-mediated autophagy substrates. Cells. 2019; 8(8): 849.
34. Chen BH, Chang YJ, Lin S, Yang WY. Hsc70/Stub1 promotes the removal of individual oxidatively stressed peroxisomes. Nat Commun. 2020; 11(1): 5267.
35. Sirtori R, Riva C, Ferrarese C, Sala G. HSPA8 knock-down induces the accumulation of neurodegenerative disorder-associated proteins. Neurosci Lett. 2020; 736: 135272.
36. Dutta R, Tiu B, Sakamoto KM. CBP/p300 acetyltransferase activity in hematologic malignancies. Mol Genet Metab. 2016; 119(1-2): 37-43.
37. Tang W, Zhou W, Xiang L, Wu X, Zhang P, Wang J, et al. The p300/YY1/miR-500a-5p/HDAC2 signalling axis regulates cell proliferation in human colorectal cancer. Nat Commun. 2019; 10(1): 663.
38. Fish JE, Cantu Gutierrez M, Dang LT, Khyzha N, Chen Z, Veitch S, et al. Dynamic regulation of VEGF-inducible genes by an ERK/ERG/p300 transcriptional network. Development. 2017; 144(13): 2428-2444.

Original Article

Altered Expression of *GDF9* and *BMP15* Genes in Granulosa Cells of Diminished Ovarian Reserve Patients: A Case-Control Study

Maryam Omrizadeh, M.Sc.[1, 2], Pegah Mokhtari, M.Sc.[2], Poopak Eftekhari-Yazdi , Ph.D.[3], Zahra Chekini, M.Sc.[4, 5], Anahita Mohseni Meybodi, Ph.D.[2, 6, 7]*

1. Department of Medical Genetics, School of Medicine, Shahid Beheshti University of Medical Sciences, Tehran, Iran
2. Department of Genetics, Reproductive Biomedicine Research Center, Royan Institute for Reproductive Biomedicine, ACECR, Tehran, Iran
3. Department of Embryology, Reproductive Biomedicine Research Center, Royan Institute for Reproductive Biomedicine, ACECR, Tehran, Iran
4. Department of Endocrinology and Female Infertility, Reproductive Biomedicine Research Center, Royan Institute for Reproductive Biomedicine, ACECR, Tehran, Iran
5. Department of Medical Genetics and Molecular Medicine, Faculty of Medicine, Mashhad University of Medical Sciences, Mashhad, Iran
6. Department of Pathology and Laboratory Medicine, Western University, London, Ontario, Canada
7. Molecular Genetics Laboratory, Molecular Diagnostics Division, London Health Sciences Centre, London, Ontario, Canada

**Corresponding Address: P.O.Box: 16635-148, Department of Genetics, Reproductive Biomedicine Research Center, Royan Institute for Reproductive Biomedicine, ACECR, Tehran, Iran*
Email: Anahita.MohseniMeybodi@lhsc.on.ca

Received: 23/May/2021, Accepted: 06/March/2022

Abstract

Objective: Diminished ovarian reserve (DOR) is a challenging issue encountered during assisted reproductive technology. Growth differentiation factor 9 (*GDF9*) and bone morphogenetic protein 15 (*BMP15*) belong to the transforming growth factor-beta (TGF-β) superfamily which are essential for folliculogenesis. We aimed to the evaluation of the *GDF9* and *BMP15* expression in the granulosa cells (GCs) of DOR patients.

Materials and Methods: This case-control study included 14 women with DOR and 12 controls, who were between 28-40 years of age undergoing controlled ovarian stimulation with a gonadotropin releasing hormone (GnRH) antagonist protocol. DOR patients were selected by the Bologna criteria. The GCs were extracted from the aspirated follicular fluids and RNA isolated from this. The fold change of gene expressions was assessed by real-time polymerase chain reaction (PCR).

Results: *GDF9* expression in patients was 0.23 times lower than the control group, which was significant (P<0.0001). *BMP15* expression in patients was 0.32 times lower than the control group, which was significant (P<0.0001). The number of archived oocytes, MII, and two pronuclei (PN) embryos was higher in the control group and these differences were statistically significant (P<0.05).

Conclusion: Given that *GDF9* and *BMP15* are specifically involved during follicular recruitmen., we expect expression of these two genes in DOR patients which is greatly reduced by reducing follicular reserve.

Keywords: Bone Morphogenetic Protein 15, Growth Differentiation Factor 9, Ovarian Reserve

Cell Journal(Yakhteh), Vol 24, No 9, September 2022, Pages: 540-545

Citation: Omrizadeh M, Mokhtari P, Eftekhari-Yazdi P, Chekini Z, Mohseni Meybodi A. Altered expression of GDF9 and BMP15 genes in granulosa cells of diminished ovarian reserve patients: a case-control study. Cell J. 2022; 24(9): 540-545. doi: 10.22074/cellj.2022.8077.

Introduction

Diminished ovarian reserve (DOR) is one of the causes of infertility in women. Subfertility is considered to be related to DOR in older women (1). Approximately 10% of women seeking fertility treatments have DOR (2).

DOR is manifest heterogeneous disorder with various etiology such as infertility, genetics, autoimmune, idiopathic, and iatrogenic. Iatrogenic causes include ovarian surgery, radiation, and chemotherapy (2, 3). DOR is associated with infertility and poor ovarian response following controlled ovarian hyperstimulation. Delays in childbearing have led to an increase in a significant number of couplesneeding assisted reproductive technology (ART) due to older age. DOR has adverse effects on ART outcomes such as decreased ovarian response to gonadotropins, and quality of oocytes and embryos, implantation rates, and live birth rates (4, 5). Sub-fertile women are regularly screened for DOR before starting therapy because of the relationship between DOR and poor *in vitro* fertilization (IVF) outcome (6). The Bologna Criteria, published in 2011, defines poor ovarian response as women having at least two of the following criteria: maternal age (≥39 years), poor ovarian reserve history (DOR; ≤3 oocytes), and abnormal ovarian reserve tests (antral follicle count [AFC] <5-7 follicles or anti-Müllerian hormone [AMH] <0.5-1.1 ng/ml) (7).

The functional unit of the ovary is the ovarian follicle (8). Development of the ovarian follicle requires coordination between somatic cell proliferation and differentiation with oocyte growth and its maturation (9). Granulosa cells (GCs) are one of the somatic cells of the follicular environment that are closely associated with the developing oocyte, ovulation, and fertilization (10). The ovarian function resulted from feedback of gonadotropins, follicle-stimulating hormone (FSH) and luteinizing hormone (LH), and local ovarian factors

(11). In addition, the transforming growth factor-beta (TGF-β) superfamily is comprised of >35 proteins that have similar common structural motivess. These proteins include activin/inhibin, growth and differentiation factor (*GDF),* bone morphogenetic protein (*BMP)* subfamilies, and *AMH* (12). Among these, *GDF9* and *BMP15* play a critical role in ovarian function.

GDF9 and *BMP15* are crucial for folliculogenesiswhich involved in primary, secondary, and antral follicles except primordial follicles. However, the mRNAs level of *GDF9* and *BMP15* detected in all stages of folliculogenesis (13). Spontaneous mutations of either *GDF9* or *BMP15* affect fertility in females (14).

As with other members of the *TGF-β* superfamily, both *GDF9* and *BMP15* exert their biological functions by forming heteromeric complexes with types 1 and 2 receptors on the cell surface (13, 15).

GDF9 derived from the oocyte, is necessary for folliculogenesis, cumulus expansion, and GCs proliferation (15). *GDF9* knockout mice were infertile because of disruptions to folliculogenesis, (16). *GDF9* motivates the expression of the FSH receptor (*FSHR*), decreases expression of the LH receptor (*LHR*), prevents follicle atresia, and affects the GCs to steroidogenesis (17).

BMP15 with *GDF9* plays a critical role in folliculogenesis and fertility. In contrast to *GDF9, BMP15* knockout mice had subfertility because of defects in ovulation and early-stage embryonic development (18). *BMP15,* during the initial and final stages of folliculogenesis, has a positive role in follicular development (17).

BMP15 and *GDF9,* like other TGFβ superfamily members, are translated as pre-proteins (19). *In vitro* studies show that both *BMP15* and *GDF9* can be expressed as linked homodimers or heterodimers (20, 21). Since studies about *GDF9* and *BMP15* focused on premature ovarian failure and comprehensive information in DOR is not available, we aimed to assess the fold of expression of *GDF9* and *BMP15* as important genes involved in folliculogenesis in the GCs of DOR patients.

Materials and Methods

This case-control study approved by the Reproductive Biomedicine Research Center Ethics Committee at Royan Institute (IR.ACECR.ROYAN.REC.1397.067). Participants were included patients admitted for infertility treatment at Royan Institute, Tehran, from 2017 to 2020. Twenty-six women (14 in the study and 12 in the control group),between 28-40 years of age undergoing IVF/intracytoplasmic sperm injection (ICSI) treatment were enrolled in this study. All patients gave their consent for collection and use of their discarded follicular fluid for research purposes.

Participants were divided into two groups, DOR and control (NOR). The Bologna criteria were used to select DOR patients. Patients were considered to have DOR if they had serum AMH levels <1.1 ng/ml and/or an AFC <5, in conjunction with serum FSH levels >10 IU/l. The NOR participants were women of normal ovarian reserves with male factor infertility cause. All women had normal karyotype and those with fragile X mental retardation 1 (*FMR1*) gene permutation, polycystic ovary syndrome (PCOS), endometriosis as well as autoimmune disorders were excluded.

Ovarian stimulation protocols

The antagonist protocol is increasingly used in the management of women with a DOR who undergo ARTs. All DOR patients and the control group underwent pituitary down-regulation with a gonadotropin realising hormon (GnRH) antagonist protocol. Patients received exogenous gonadotropins on the second or third day of menstruation while the leading follicle reached 13 mm in diameter, followed by a GnRH antagonist. Human chorionic gonadotropin (hCG) was prescribed when the follicles were dominant in terms of size. When follicles reached ≥ 18 mm diameters, follicles puncture was performed and GCs from follicular fluid were collected. Following follicles puncture oocytes number, quality, and embryos grading were assessed (22).

Purification of granulosa cells from follicular fluid

The aspirated follicular fluid was centrifuged at 2000 g for 10 min, then 4 ml of salt tayrod added to the pellet, and it was slowly layered on a 50% sill select gradient and centrifuged at 3000 g for 30 min. The GCs collected and removed using a sterile transfer pipette and placed into a 15 ml tube that contained 3 mL of cold DMEM/F-12 media supplemented with 1x penicillin/streptomycin and 10% fetal bovine serum, followed by centrifugation. Enzymatic digestion with hyaluronidase enzyme was performed to disperse the GCs (23).

Multinucleated giant cells were then washed in DMEM/F-12. The tube was centrifuged at 1500 rpm for 5 minutes at 21°C, and then 5 ml RBC lysing buffer (RLB) added to the pellets. The RLB solution consisted of ammonium chloride, potassium bicarbonate, and EDTA. The diluted solution was kept at room temperature for 2-5 minutes and centrifuged at 1500 rpm for 3 minutes at 21°C. Then, it was washed once with DMEM/F12. Cell counts and viability assessments were performed before the second centrifugation. The GCs were washed, centrifuged at 1500 rpm for 5 minutes, pelleted, and frozen at -80°C until RNA extraction (24, 25).

RNA extraction

RNeasy Mini-kit (Qiagen, Valencia, CA, USA, cat. no: 74004) was used according to the manufacturer's protocol to extract the RNA. The amount of RNA was measured by using a Nano Drop ND-1000 spectrophotometer (Thermo Scientific, Nano Drop spectrophotometer).

cDNA synthesis

For cDNA synthesis, we used 30 ng total RNA according to the manufacturer's instructions in the QuantiTect Whole Transcriptome Kit (Qiagen, cat. no: 207045).

Quantitative real-time polymerase chain reaction

Polymerase chain reaction (PCR) targets were created from the template RNA using the manufacturer's protocols. Gene-specific primers were designed by using Perl Primer software. Then, the primers examined by Primer-BLAST to ensure that they were not linked to non-specific sites of the genome. The Primers used for real-time PCR are shown in the Table 1.

Table 1: Primer sets used for real-time RT-PCR

Gene	Primer sequence (5´-3´)	Product size (bp)
GAPDH	F: AGAAGGCTGGGGCTCATTTG	228
	R: TGATGGCATGGACTGTGGT	
GDF9	F: AGAAGTCACCTCTACAACACTG	132
	R: AACGGTAGTAATGCGATCCA	
BMP15	F: TGTGAACTCGTGCTTTTCATG	102
	R: CTCAATCAGGGGCAAAGTAGG	

mRNA quantification was performed by quantitative reverse transcription polymerase chain reaction (qRT-PCR) using a Step-One RT-PCR system (Applied Biosystems, USA). Amplification of the genes of interest and *GAPDH* were performed in duplicate wells. *GAPDH* was used as the endogenous control for normalization.

Statistical analysis

Statistical calculations were performed using the IBM SPSS statistic 22 software (IBM, United states). The student's t test with a two-tailed distribution for equality of variances was used. $P<0.05$ indicated statistical significance. Gene expression data were analyzed using the $2^{-\Delta\Delta Ct}$ algorithm to calculate the *GDF9* and *BMP15* mRNAs level relative to the level of *GAPDH*.

Results

Clinical characteristics

Table 2 demonstrates the demographic data and clinical characteristics of DOR and the NOR at baseline. There was no significant difference between the two groups in age and age at menarche.

The result of IVF revealed achieved oocytes, MII, two PN were higher in the NOR group compared to DOR patients these differences were statistically significant ($P<0.05$, Table 2).

The expression profile for target genes in NOR and DOR groups granulosa cells

Quantitative expression of these genes in GCs of DOR patients and the control group was performed by RNA extraction and cDNA synthesis with primers designed for each gene. The *GAPDH* primer was used as the internal control for real-time PCR.

Table 2: Demographic characteristics, oocyte and embryo parameters between DOR and NOR groups

Criteria	Case (n=14)	Control (n=12)	P value*
Age (Y)	34.07 ± 3.91	34.25 ± 2.98	0.898
Age at menarche (Y)	13.71 ± 1.32	13.5 ± 0.797	0.63
Oocyte number	2.14 ± 0.66	7 ± 2.98	<0.00
MI	0.85 ± 0.37	1.62 ± 1.06	0.093
MII	1.42 ± 0.51	5.58 ± 2.46	<0.00
GV	1 ± 0	1.16 ± 0.408	0.51
2PN	1.41 ± 0.51	4.09 ± 2.73	0.003
Embryo quality			
Good (AB or B)	1.14 ± 0.37	3.82 ± 2.75	0.022
Fair (BC or C)	1.29 ± 0.48	1 ± 0	0.35
Poor (CD or D)	0	0	-

Data are presented as mean ± SD. *; Obtained by independent sample t test. Statistically significant level at 0.05. MI; Metaphase I, MII; Metaphase II, GV; Germinal vesicle, PN; Pronuclei, DOR; Diminished ovarian reserve, and NOR; Normal ovarian reserve.

The standard curve was used to evaluate the efficiency of primers and relative quantification. For normalization of the *GDF9* and *BMP15* genes and drawing a standard curve, was investigated in gene database sites such as NCBI and Gene Cards. The highest expression of these genes was found in testicular tissue. Therefore, standard curves were prepared by serial dilution to evaluate the efficiency of primers and real time PCR procedures.

GDF9 mRNA expressions in granulosa cells

All amplified RT-PCR products were at the expected size for *GDF9* and *GAPDH* (housekeeping) genes. *GDF9* expression in patients was 0.23 times lower than the control group,which was significant (P<0.0001, Fig.1).

BMP15 mRNA expression in granulosa cells

All amplified RT-PCR products were at the expected size for *BMP15* and *GAPDH* (housekeeping) genes. *BMP15* expression in patients was 0.32 times lower than the control group, which was significant (P<0.0001, Fig.1).

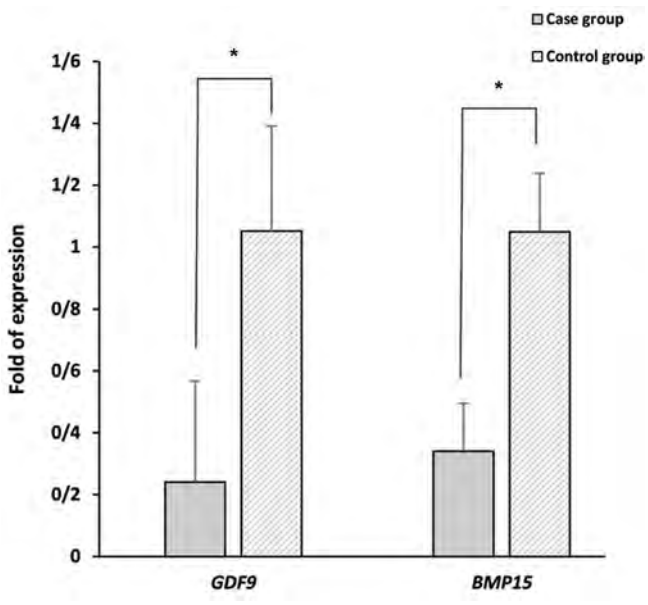

Fig.1: Comparison of GDF9 and BMP15 expressions between DOR and NOR groups. *; Statistical significant level at 0.05, DOR; Diminished ovarian reserve, and NOR; Normal ovarian reserve.

Comparison of elevated serum hormone levels

Although the serum level of AMH was significantly decreased in the case group, the mean serum level of FSH and LH on the third day of menstruation was significantly increased in cases in comparison with control participants (P<0.0001, Fig.2). The serum thyroid-stimulating hormone (TSH) level was not different between the two groups (P≥0.05, Fig.2).

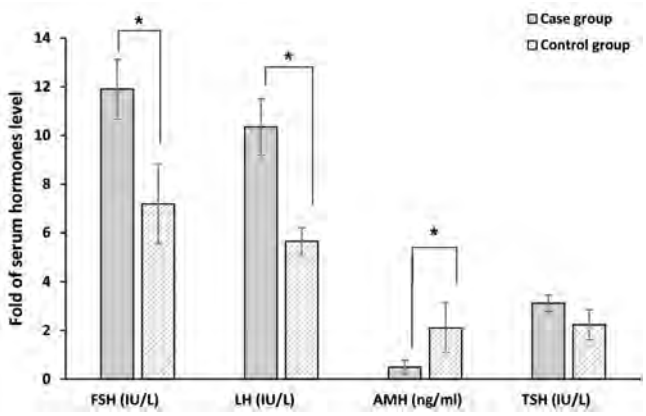

Fig.2: Mean serum hormones level between DOR and NOR groups. *; Statistical significant level at 0.05, FSH; Follicle-stimulating hormone, LH; Luteinizing hormone, AMH; Anti-Müllerian hormone, TSH; Thyroid-stimulating hormone, DOR; Diminished ovarian reserve, and NOR; Normal ovarian reserve.

Discussion

In our study, we assessed the expression of *GDF9* and *BMP15* in GCs of DOR patients with bologna criteria and 28-40 years old. In comparison with male factor patients as a control group, we observed that the mean relative expressions of *GDF9* and *BMP15* were significantly lower in GCs of the infertile DOR patients compared with the control group.

Recent studies of genetic mutations in sheep, goats, and mice highlight the importance of oocyte-secreted factors in regulating ovarian follicular development and ovulation (13, 19, 26). Although some genetic causes of DOR are established, little is known about definitive gene mutations associated with DOR (2).

During the procedure of folliculogenesis, interplays between the oocyte and the somatic cells that surround it (GCs) are recognized that are the enduring effects of this interaction on the potential for the stages after fertilization for embryonic development (23).

The TGF-β superfamily, in particular *GDF9* and *BMP15*, oocyte-secreted growth factors play a critical role in ovarian organization and fertility. These factors are essential for the growth, development, and function of GCs according to the results from studies carried out on animals.

Knockout mouse technology has been used over the past decade to define the essential role of ovarian gene expression and the discovery of genetic interactions.

The distribution of the *GDF9* , *BMP15* mRNA,proteins, and BMP receptor mRNA,were evaluated in goat and bovine ovaries (13, 27, 28) to determine if these TGF-β members may play an important role in follicular development in goats (13).

In humans, there is a lack of expression level of these genes in DOR and only polymorphisms and mutations of *GDF9* are associated with DOR. In a study of Chinese

women, 3 out of 139 (2.2%) women with DOR had a specific mutation (p.R146C), whereas this mutation was not present in the control group (n=159) (15). In another study, *GDF9* was associated with DOR. A study compared 103 Chinese women with DOR to 123 age-matched women with normal ovarian reserve. The women were analyzed for three single nucleotide polymorphisms (SNPs) of *GDF9*. A higher prevalence of the GA/AA genotype was found in those with poor ovarian response (32%) during IVF cycles compared with those with the control group (19.5%) (29).

Recently, Gong et al. (30) had evaluated *GDF9* and *BMP15* expression in GCs of poor patients according to bologna criteria. They subdivided patients via age including <35 years, 35-40 years, and >40 years. Also they observed the expression of these genes decreased with the age of poor patients especially after 40 years which related to lower oocyte quality and pregnancy outcome.

In the current study, the number of achieved oocytes, MII, and 2PN embryos were significantly lower in DOR patients. Since, these genes involved in folliculogenesis it seems lower expression of these genes involved in poor oocyte achievements in DOR patients. Because achieve oocyte from DOR patients is difficultanalysis was performed in limited sample size and further studies with more samples is essential.

BMP15 and *GDF9* are oocyte-secreted factors that we assessed expression of these genes in the targeted tissue (granolosa cells) because of limited number of oocyte. A better suggestion is to check their receptor or target genes in GCs. In future, we collect enough samples and are going to study these receptor or target genes.

Conclusion

In the current study, we observed the significant reductions of *GDF9* and *BMP15* gene expressions in GCs of DOR patients compared to the control group. The decreased oocyte numbers and 2PN embryos in the DOR group might be secondary to the decrease in the expressions of the above genes. Based on the above findings and the information we have regarding the function of these two genes, it seems that there is a role for these paracrine factors in the folliculogenesis process as well as the interaction of GCs with oocytes which further studies with larger sample size is essential for its confirmation.

Acknowledgments

We are grateful to Mrs. Z. Vahhabi from Royan Institute for the collection of follicle fluid samples and Mrs Forough Sayahpoor for their incredible supports. This study was conducted with the financial support of Royan Institute, Reproductive Biomedicine Research Center, Tehran, Iran. The authors declare no conflict of interest.

Authors' Contributions

M.O.; Conceived and carried out experiments, literature review, and manuscript drafting. A.M.M.; Administrative support, contributed to conception and design, and literature review. P.E.-Y.; Samples collection and draft revision. P.M., Z.Ch.; Contributed to the collection and assembly of data, draft revision. All authors read and approved the final version of the manuscript.

References

1. May-Panloup P, Ferré-L'Hôtellier V, Morinière C, Marcaillou C, Lemerle S, Malinge MC, et al. Molecular characterization of corona radiata cells from patients with diminished ovarian reserve using microarray and microfluidic-based gene expression profiling. Hum Reprod. 2012; 27(3): 829-843.
2. Greene AD, Patounakis G, Segars JH. Genetic associations with diminished ovarian reserve: a systematic review of the literature. J Assist Reprod Genet. 2014; 31(8): 935-946.
3. Fusco F, Paciolla M, Chen E, Li X, Genesio R, Conti A, et al. Genetic and molecular analysis of a new unbalanced X; 18 rearrangement: localization of the diminished ovarian reserve disease locus in the distal Xq POF1 region. Hum Reprod. 2011; 26(11): 3186-3196.
4. Jahromi BN, Sadeghi S, Alipour S, Parsanezhad ME, Alamdarloo SM. Effect of melatonin on the outcome of assisted reproductive technique cycles in women with diminished ovarian reserve: a double-blinded randomized clinical trial. Iran J Med Sci. 2017; 42(1): 73-78.
5. Sun W, Stegmann BJ, Henne M, Catherino WH, Segars JH. A new approach to ovarian reserve testing. Fertil Steril. 2008; 90(6): 2196-2202.
6. Levi AJ, Raynault MF, Bergh PA, Drews MR, Miller BT, Scott RT. Reproductive outcome in patients with diminished ovarian reserve. Fertil Steril. 2001; 76(4): 666-669.
7. Ferraretti A, La Marca A, Fauser B, Tarlatzis B, Nargund G, Gianaroli L, et al. ESHRE consensus on the definition of 'poor response'to ovarian stimulation for in vitro fertilization: the Bologna criteria. Hum Reprod. 2011; 26(7): 1616-1624.
8. de Castro FC, Cruz MHC, Leal CLV. Role of growth differentiation factor 9 and bone morphogenetic protein 15 in ovarian function and their importance in mammalian female fertility—a review. Asian-Australas J Anim Sci. 2016; 29(8): 1065-1074.
9. Thomas FH, Vanderhyden BC. Oocyte-granulosa cell interactions during mouse follicular development: regulation of kit ligand expression and its role in oocyte growth. Reprod Biol Endocrinol. 2006; 4(1): 19.
10. Ceko M, Hummitzsch K, Hatzirodos N, Bonner W, Aitken J, Russell D, et al. X-Ray fluorescence imaging and other analyses identify selenium and GPX1 as important in female reproductive function. Metallomics. 2014; 7(1): 71-82.
11. Chand AL, Ponnampalam AP, Harris SE, Winship IM, Shelling AN. Mutational analysis of BMP15 and GDF9 as candidate genes for premature ovarian failure. Fertil Steril. 2006; 86(4): 1009-1012.
12. Juengel J, McNatty K. The role of proteins of the transforming growth factor-β superfamily in the intraovarian regulation of follicular development. Hum Reprod Update. 2005; 11(2): 144-161.
13. Silva J, Van den Hurk R, Van Tol H, Roelen B, Figueiredo J. Expression of growth differentiation factor 9 (GDF9), bone morphogenetic protein 15 (BMP15), and BMP receptors in the ovaries of goats. Mol Reprod Dev. 2005; 70(1): 11-19.
14. Su YQ, Sugiura K, Wigglesworth K, O'Brien MJ, Affourtit JP, Pangas SA, et al. Oocyte regulation of metabolic cooperativity between mouse cumulus cells and oocytes: BMP15 and GDF9 control cholesterol biosynthesis in cumulus cells. Development. 2008; 135(1): 111-121.
15. Wang TT, Ke ZH, Song Y, Chen LT, Chen XJ, Feng C, et al. Identification of a mutation in GDF9 as a novel cause of diminished ovarian reserve in young women. Hum Reprod. 2013; 28(9): 2473-2481.
16. Dong J, Albertini DF, Nishimori K, Kumar TR, Lu N, Matzuk MM. Growth differentiation factor-9 is required during early ovarian folliculogenesis. Nature. 1996; 383(6600): 531-535.
17. Otsuka F, McTavish KJ, Shimasaki S. Integral role of GDF-9 and BMP-15 in ovarian function. Mol Reprod Dev. 2011; 78(1): 9-21.
18. McMahon HE, Hashimoto O, Mellon PL, Shimasaki S. Oocyte-specific overexpression of mouse bone morphogenetic protein-15

leads to accelerated folliculogenesis and an early onset of acyclicity in transgenic mice. Endocrinology. 2008; 149(6): 2807-2815.
19. McNatty KP, Moore L, Hudson NL, Quirke L, Lawrence SB, Reader K, et al. The oocyte and its role in regulating ovulation rate: a new paradigm in reproductive biology. Reproduction. 2004; 128(4): 379-386.
20. Shimasaki S, Moore RK, Otsuka F, Erickson GF. The bone morphogenetic protein system in mammalian reproduction. Endocr Rev. 2004; 25(1): 72-101.
21. Paulini F, Melo EO. The role of oocyte-secreted factors GDF9 and BMP15 in follicular development and oogenesis. Reprod Domest Anim. 2011; 46(2): 354-361.
22. Balaban B, Brison D, Calderon G, Catt J, Conaghan J, Cowan L, et al. Alpha scientists in reproductive medicine and ESHRE special interest group of embryology. The Istanbul consensus workshop on embryo assessment: proceedings of an expert meeting. Hum Reprod. 2011; 26(6): 1270-1283.
23. Greenseid K, Jindal S, Hurwitz J, Santoro N, Pal L. Differential granulosa cell gene expression in young women with diminished ovarian reserve. Reprod Sci. 2011; 18(9): 892-899.
24. Chilvers R, Bodenburg Y, Denner L, Urban R. Development of a novel protocol for isolation and purification of human granulosa cells. J Assist Reprod Genet. 2012; 29(6): 547-556.
25. Aghadavod E, Zarghami N, Farzadi L, Zare M, Barzegari A, Movassaghpour AA, et al. Isolation of granulosa cells from follicular fluid; applications in biomedical and molecular biology experiments. Adv Biomed Res. 2015; 4.
26. Thomas FH, Vanderhyden BC. Oocyte-granulosa cell interactions during mouse follicular development: regulation of kit ligand expression and its role in oocyte growth. Reprod Biol Endocrinology. 2006;4(1):1-8.
27. Sudiman J, Sutton-McDowall ML, Ritter LJ, White MA, Mottershead DG, Thompson JG, et al. Bone morphogenetic protein 15 in the pro-mature complex form enhances bovine oocyte developmental competence. PLoS One. 2014; 9(7): e103563.
28. Sugimura S, Ritter LJ, Sutton-McDowall ML, Mottershead DG, Thompson JG, Gilchrist RB. Amphiregulin co-operates with bone morphogenetic protein 15 to increase bovine oocyte developmental competence: effects on gap junction-mediated metabolite supply. Mol Hum Reprod. 2014; 20(6): 499-513.
29. Wang TT, Wu YT, Dong MY, Sheng JZ, Leung PC, Huang HF. G546A polymorphism of growth differentiation factor-9 contributes to the poor outcome of ovarian stimulation in women with diminished ovarian reserve. Fertil Steril. 2010; 94(6): 2490-2492.
30. Gong Y, Li-Ling J, Xiong D, Wei J, Zhong T, Tan H. Age-related decline in the expression of GDF9 and BMP15 genes in follicle fluid and granulosa cells derived from poor ovarian responders. J Ovarian Res. 2021; 14(1): 1-10.

Short Communication

Two New Variants in *FYCO1* Are Responsible for Autosomal Recessive Congenital Cataract in Iranian Population

Ebrahim Shirzadeh, M.D.[1*], Fahimeh Piryaei, Ph.D.[2], Hanieh Naddaf, M.Sc.[3], Zahra Barabadi, Ph.D.[4, 5*]

1. Department of Ophthalmology, School of Medicine, Sabzevar University of Medical Sciences, Sabzevar, Iran
2. Department of Molecular Medicine and Genetics, Research Center for Molecular Medicine, School of Medicine, Hamadan University of Medical Sciences, Hamadan, Iran
3. Core facility of Hamadan University of Medical Sciences, Hamadan, Iran
4. Department of Tissue Engineering, School of Medicine, Hamadan University of Medical Sciences, Hamadan, Iran
5. School of Medicine, Sabzevar University of Medical Sciences, Sabzevar, Iran

**Corresponding Addresses: P.O.Box: 9613873137, Department of Ophthalmology, School of Medicine, Sabzevar University of Medical Sciences, Sabzevar, Iran*
P.O.Box: 6517838696, Department of Tissue Engineering, School of Medicine, Hamadan University of Medical Sciences, Hamadan, Iran
Emails: dreshirzad@yahoo.com, z.barabadi@umsha.ac.ir

Received: 22/June/2021, Accepted: 16/October/2021

Abstract

The purpose of this experimental study was to investigate the genetic etiology of congenital cataract (CC) manifesting an autosomal recessive pattern of inheritance in four Iranian families. Affected individuals and their normal first-degree relatives in each family were included in the present study. The genomic DNA of the blood samples was extracted from all participants, and one affected member belonging to each family was subjected to Whole Exome Sequencing (WES). Using bidirectional Sanger sequencing, the identified variants were validated by co-segregation analysis. Two different mutations were detected in the *FYCO1* gene encoding FYVE and coiled-coil domain-containing protein. A previously reported missense mutation, c.265C>T (p.Arg89Cys), was found in one Iranian family for the first time, and a combination of two variants in a single codon, c.[265C>T;267C>A] (p.Arg89X), was identified in the three other families. On the other hand, accompanying the c.265C>T mutation, the presence of the c.267C>A polymorphism leads to a premature stop codon. In-Silico Analysis of FYCO1 protein demonstrated that RUN domain will be interrupted so that the large part of functional protein will be eliminated due to this novel variant. FYCO1 has been proved to be involved in human lens development and transparency. Its mutations, therefore, result in CC. Herein, we reported the first autosomal recessive CC patients with c.265C>T (p.Arg89Cys) or c.[265C>T;267C>A] variant in Iranian population for the *FYCO1* gene. *FYCO1* mutations could be tracked for preventive objectives or even be targeted as therapeutic candidates via treatment approaches in the future.

Keywords: Congenital Cataract, *FYCO1*, Mutation, Sanger Sequencing, Whole Exome Sequencing

Cell Journal(Yakhteh), Vol 24, No 9, September 2022, Pages: 546-551

Citation: **Shirzadeh E, Piryaei F, Naddaf H, Barabadi Z. Two new variants in FYCO1 are responsible for autosomal recessive congenital cataract in Iranian population. Cell J. 2022; 24(9): 546-551. doi: 10.22074/cellj.2022.8116.**

Cataract is defined as any opacity of the transparent lens of the eye, causing blindness and visual impairment (1, 2). Cataracts can occur either in association with a large number of genetic disorders (3, 4) or due to some environmental factors such as infectious agents like cytomegalovirus, toxoplasmosis, rubella, herpes, varicella, and syphilis, drug exposure during pregnancy (corticosteroids, vitamin A), and X-ray radiation. Congenital cataract (CC) is a clinically and phenotypically highly heterogeneous eye disorder (5, 6), which may lead to permanent blindness if remains undetected in childhood. CC refers to the cataract causing by various factors and affecting the development of the lens during the fetal period and it approximately accounts for about 10% of all childhood blindness (7, 8). Hereditary is the leading cause of at least one-third of all these cases. Autosomal dominance is the most frequent pattern of inheritance reported for this disorder, although it could be autosomal recessive or X-linked. More than 15 distinct loci on 14 unique chromosomal locations have been identified to be involved in this disorder (3, 4, 9-11). To date, several genes coding lens proteins, cytoskeletal proteins, transcription factors as well as membrane transport protein genes are known to be involved in this disorder (12). Considerably, 27 genes such as *CRYAA*, *CRYB1*, *CONNEXIN 46*, *PITX*, *EPHA2*, and *FOXE3, GJA8, FYCO1* have been identified to be linked in non-syndromic autosomal recessive CC (arCC) (1, 11, 13).

The incidence of CC in different populations is around 12-136 per 100000 children (9). Inherited cataracts account for about 8.3-25% of all CC cases (14). While the global prevalence of this disorder is 1 to 15 per 10,000 children (15), the overall risk for this disorder is 92.4 per 100,000 children, 107.9 and 76.2 for males and females, respectively (9). Since consanguineous marriage is of high frequency in Iran, it is not unexpected to observe a high incidence of this condition in the Iranian population.

Considering the meaningful prevalence of CC in

Soozandeh village in Iran, the purpose of this study was to identify the genetic basis of CC in this area using next-generation sequencing (NGS) and Sanger sequencing techniques and assessing risks for the next generation in this population.

This experimental study was initially approved by the Ethical Committee of Sabzevar University of Medical Sciences (IR.MEDSAB.REC.1395.120). Four Iranian families with history of CC were selected from the people of Soozandeh village in Iran. One affected individual of each family was recruited in a high throughput study. Additionally, all affected and unaffected siblings and living parents entered the experiment following the segregation study. The Family members' blood sample was collected after getting written informed consent of all participants. A family medical history was recorded and a pedigree for each family was constructed based on the acquired information. Two families were consanguineous.

The living family members underwent ocular examination by a cornea fellowship in Vasei Hospital, Sabzevar University of Medical Sciences. The assessment included: gross appearance, visual acuity measurement, intraocular pressure (IOP) measurement using (Haagsh, Tonometer, Switzerland), eye movements, evaluation of anterior segment consisting of the cornea, pupil, lens, and iris; as well as posterior segment including fundus, vitreous chamber, retina, optic disk, and macula, using a slit lamp (Topcon, Japan).

Whole blood as the source of genomic DNA was processed using a salting out procedure. The DNA concentration was determined by a Nano drop spectrophotometer (BIO INTELLECTICA Nano100, Canada). Two micrograms of DNA were used for whole Exome Sequencing (WES), using Illumina HiSeq 2500, Q30≥80% (Novogene, Beijing). WES using UCSC hg19 as a reference genome, included exome capture using Agilent SureSelect Human All Exon V6 Kit and sequencing depth of 50× through paired-end sequencing with a HiSeq 2500 Genome Analyzer (Illumina), which led to 150 bases sequences from each end of the fragments. SNV and InDels were identified using VarScan version 2.2.5, and MuTec and GATK Somatic Indel Detector, respectively. The prediction of probable effects due to identified variants was performed using Mutation Taster (16). The secondary structure of mutant FYCO1 protein was predicted by GORIV (17).

For extension of the mutated region, conventional polymerase chain reaction (PCR) was performed using Taq DNA Polymerase Master Mix RED (Ampliqon, Odense M DENMARK) and specific primer sequences of

F: 5′-TAAATGCCGGAATGAAGAGC-3′
R: 5′-GCTTTAAGCAGGCAAAAGG-3′ (product size 241 bp).

Primer designation was performed using Primer3 (http://bioinfo.ut.ee/primer3-0.4.0/). Amplification was performed using the parameters below: initial denaturation at 95°C for 2 minutes, 35 cycles of 95°C for 30 seconds, 54.9°C for 30 seconds and 72°C for 35 seconds, followed by final 5 minutes extension at 72°C. The cleanup PCR products using ExoSAP-IT® (USB, Cleveland, Ohio, USA) were bi-directionally sequenced using a 3730XL DNA analyzer (ABI, Foster City, CA, USA).

Four families affected by CC (IrCC1, IrCC2, IrCC3, and IrCC4) were included from Soozandeh village of Iran. Drawing the pedigrees demonstrated an autosomal recessive pattern of inheritance (Fig.1). Two families including IrCC1 and IrCC3 showed consanguineous marriage. The medical history of affected members was obtained in detail, and cataracts were validated via the patients' medical records and ocular examination. The individuals affected by CC had already undergone cataract-removal surgery; amongst, some had posterior chamber intraocular lens and some were aphakic. Intra-ocular pressure in both healthy and affected groups was in the normal range of 12-18 mmHg, without any significant difference.

WES was performed on the genomic DNA of one proband in each family. Regarding the consanguinity in two families under the study and the probability of autosomal recessive inheritance pattern in these families, we prioritized homozygous potentially functional variants residing within the runs of homozygosity (larger than 1 Mb). The genomic variants screening was performed through different population databases of gnomAD and GME, as well as Iranome, an in-house database for genetic variants in the Iranian population. For the filtering approach, synonymous variants, intronic variants (>5 bp from exon boundaries), and variants with >0.01% minor allele frequency were eliminated. Homozygous variants, as well as compound-heterozygous variants, were designated in consanguineous families. Intriguingly, in all four families, we found 2 different homozygous variants in the *FYCO1* gene. c.265C>T (p.Arg89Cys) (NM_024513.4; rs141476300), a previously known missense mutation, was identified in the proband of IrCC1. However, it is the first report of this variant in the Iranian population. Interestingly, c.[265C>T;267C>A] (p.Arg89X) in the same position was detected in the probands of families IrCC2, IrCC3, and IrCC4, resulting in a premature stop codon and subsequent protein truncation (Fig.2). The variants were investigated in affected and unaffected family members by Sanger sequencing (Fig.3). In the aforementioned three families, carriers were heterozygous for c.265C>T and homozygous for c.267C>A. c.267C>A is known to be a frequent allele in the Iranian population-based on Iranome. Table 1 represents the reported pathogenic mutations in the *FYCO1* gene with related amino acid changes in non-syndromic CC.

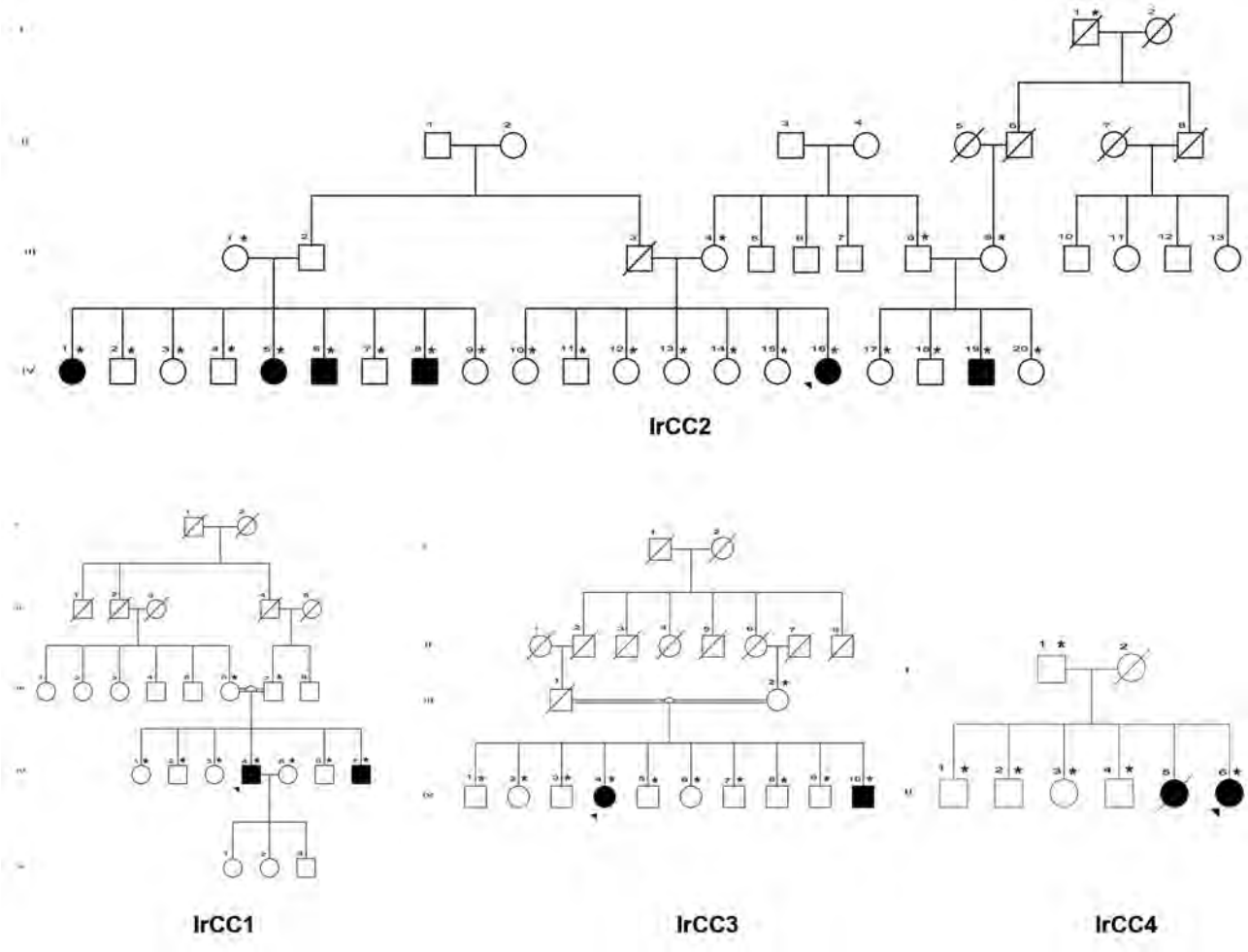

Fig.1: Four pedigrees of CC originated from Iran. One proband per family was selected for WES. The probands' parents of IrCC1 and IrCC3 families were first-degree cousins. Affected individuals have been depicted by filled symbols. Individuals marked with an asterisk were genotyped by Sanger sequencing for mutation screening. IrCC; Iranian family of congenital cataract, WES; Whole exome sequencing, and CC; Congenital cataract.

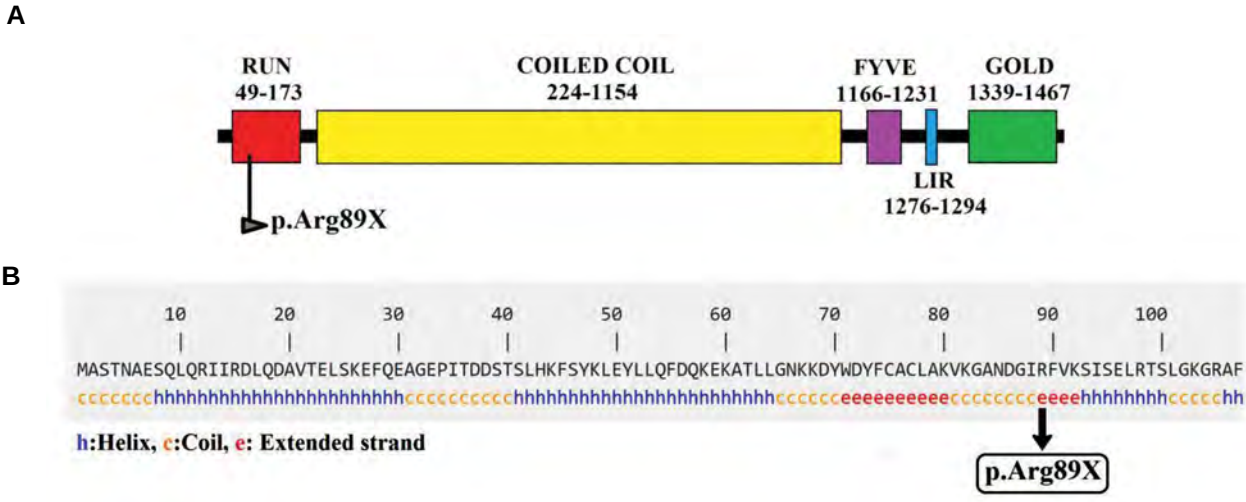

Fig.2: Position of c.267C>A variant in FYCO1 at protein level. **A.** p.Arg89X identified in our study in Run domain of FYCO1 protein in three Iranian families. **B.** Secondary structure prediction of mutant FYCO1 protein. In-silico analysis illustrates that the p.Arg89X mutation results in a truncated product.

In the present study, we investigated the genetic cause of CC which is very common over multiple generations in Soozandeh, a small village in Iran. To assess the exact etiology of CC in these populations, we performed gene analysis through WES. We identified c.265C>T (p.Arg89Cys) in the *FYCO1* gene in the non-consanguineous IrCC4 family. According to the in-house Iranome database, this missense mutation was detected for the first time, in the Iranian population. In the other three families, two of which were consanguineous, a combination of two variants in codon 89, as c.[265C>T;267C>A] (p.Arg89X), was detected in the *FYCO1* gene. Genotyping the affected and carrier members of these families revealed that carriers were heterozygous for c.265C>T and homozygous for c.267C>A (rs4682801). The allele frequency of c.267C>A in the Iranian population is 0.8931, being found in certain ethnicities including Kurd, Persian Gulf Islander, Turkmen, Lur, Arab, Persian, Azeri and Baloch. According to The Genome Aggregation Database (gnomAD), 1000 Genomes Project, and NHLBI Exome Sequencing Project (ESP) Exome Variant Server, the allele frequency of c.265C>T is 0.00041, 0.00040, and 0.00031, respectively.

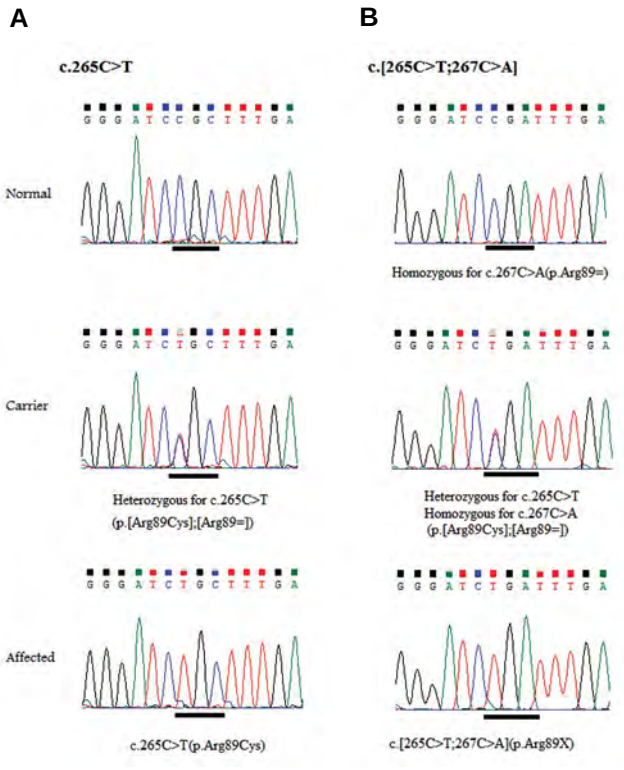

Fig.3: Sequencing chromatograms demonstrating two homozygous mutations in the *FYCO1* gene related to cataract 18. **A**. Forward sequence chromatograms related to c.265C>T (p.Arg89Cys) mutation in the normal, carrier, and affected individuals in family IrCC4. **B.** Forward sequence chromatograms of c.[265C>T;267C>A] (p.Arg89X) mutation in the normal, carrier, and affected individuals in families IrCC1, IrCC2, and IrCC3. Probands are homozygous and unaffected individuals are heterozygous. Black bars mark the variant position.

Cataracts are caused by alterations in either lens structure, intracellular proteins order, or development of lens fibers. *FYCO1,* located on 3p21.3, encodes a protein containing disparate domains and regions including a α-helical RUN domain, a FYVE-type zinc finger domain, a Golgi dynamics (GOLD) domain, four coiled-coil regions, and a LC3-interacting region (LIR) (18). FYVE and coiled-coil domain containing 1 (FYCO1) is a member of the phosphatidylinositol-3-phosphate (PI3P)-binding protein family which is expressed in eye tissue. FYCO1 functions in the transportation of microtubule plus-end-directed of autophagic vesicles through interactions with the small GTPase RAB7, PI3P, and the autophagosome marker LC3 (19). CC and dysmorphic lens development disorders may be caused by mutation of the *FYCO1* gene via disruption of autophagosomal transportation to lysosomes and resultant defective degradation of mitochondria and other organelles in lens fibroblasts (18, 20, 21).

Mutations in *FYCO1* were first reported by Pras et al. (22) as a cause of arCC-2 (CATC2, OMIM: 610019) or cataract 18 in consanguineous Arab families. Subsequently, various mutations have been identified in different loci of *FYCO1* in association with cataract 18 in different ethnicities. A large number of mutations in *FYCO1* occurs with higher frequency for frame-shift and nonsense mutations such as c.1045C>T (p.Gln349X), c.1546C>T (p.Gln516X), c.2206C>T (p.Gln736X), c.2761C>T (p.Arg921X), c.2830C>T (p.Arg944X), c.3755delC (p.Ala1252AspfsX71), c.3858_3862dupGGAAT (p.Leu1288TrpfsX37) (18, 23), and c.808C>T (p.Gln270X) (24). In the Iranian population, the first report of a homozygous mutation in *FYCO1 was* related to c.1056_1071delGGCCACACGGGACTCA (p.E352DfsX9) (25). In our study, the c.[265C>T;267C>A] (p.Arg89X) and c.265C>T (p.Arg89Cys) mutations are the first reports in the Iranian population. According to the bioinformatics analysis of our findings, c.[265C>T;267C>A] (p.Arg89X) mutation resulting in premature stop codon interrupts the RUN domain in the beginning portion of FYCO1 protein so that the large parts of the functional protein are eliminated (Fig.2). Due to this huge elimination, bioinformatics analysis on the three-dimensional structure of the truncated protein was not feasible. Nonetheless, premature stop codons mostly terminate in mRNA degradation via nonsense-mediated mRNA decay (NMD). The c.265C>T (p.Arg89Cys) mutation deleteriously affects the protein structure and function so that is considered damaging based on bioinformatics prediction tools including SIFT, Polyphen, PROVEAN, CADD (PHRED score for c.265C>T: 28.1) and Mutation Taster. In addition, this mutation has been recently established in ClinVar as a likely pathogenic variant.

By the time, 157 different variants in *FYCO1* have been established in Iranome found in different ptable arts of *FYCO1* including exons, introns, splice sites, and untranslated region (UTR); of which 42 variants change protein sequence. However, only c.3150+1G>T

has been reported to be likely pathogenic based on ClinVar. Other identified variants of Iranome have been known as benign or of uncertain significance since these variations have been found in a healthy population. Being detected in the Iranian population, following out the mutations of *FYCO1* might have prenatal or postnatal diagnostic values since a cataract as a visual problem can affect the quality of neonatal life. Early diagnosis could be helpful to families to manage their child's requirements at the right time.

In conclusion, we report two mutations of the *FYCO1* gene including c.265C>T (p.Arg89Cys) and c.[265C>T;267C>A] (p.Arg89X) in arCC in 4 originally Iranian families. Our study provides a new understanding of arCC pathogenesis in the Iranian population, and therefore it might be helpful to consider *FYCO1* mutations in genetic diagnostic methods in pediatric cataracts. Moreover, *FYCO1* mutations could be tracked for preventive objectives or even be targeted as therapeutic candidates for gene therapy approaches in the future.

Table 1: List of reported *FYCO1* gene mutations associated with non-syndromic CC

Exon/Intron	Nucleotide changes	Amino acid changes	Type	Reference(s)
Ex6	c.449T>C	p.I150T	Missense	(26)
Ex8	c.808C>T	p.Q270X	Compound heterozygous	(27)
Ex8	c.1045C>T	p.Q349X	Nonsense	(18)
Ex8	c.1546C>T	p.Q516X	Nonsense	(18)
Ex8	c. 2206C>T	p.Q736X	Nonsense	(18, 23)
Ex8	c.2345delA	p.Q782RfsX32	frame shift	(23)
Ex8	c.2345delA/ c.2714_2715delCA	p.Q782RfsX32/ p.T905SfsX2	Compound heterozygous	(28)
Ex8	c.2506delG	p.A836PfsX80		(29)
Ex8	c.2761C>T	p.R921X	frame shift	(18)
Ex8	c.2830C>T	p.R944X	Nonsense	(18)
Ex8	c.l056_1071delGGCCACACGGGACTCA	p.E352DfsX9	Nonsense	(25)
IVS9	c. 3150＋1G>T	splice variant	frame shift	(18)
IVS9	c.3151-2A>C	p.A1051DfsX27	splice variant	(23)
Ex10	c.3196delC	p.H1066IfsX10	frame shift	(13)
Ex13	c.3670C>T	p.R1224X	frame shift	(30)
Ex13	c.3755delC	p.A1252DfsX71	Nonsense	(18)
Ex14	c.3858_3862dupGGAAT	p.L1288WfsX37	frame shift	(18)
IVS14	c.3945-1G>C	splice variant	frame shift	(30)
Ex16	c.4127T>C	p.L1376P	splice variant	(13, 18)
Ex17	c.4270C>T	p.R1424X	Missense	(13)

Acknowledgments

This study has been funded by Sabzevar University of Medical Sciences. The authors kindly appreciate the Cellular and Molecular Research Center at Sabzevar University of Molecular Sciences for the financial support. We also would like to thank Mr. Abolfazl Rad and Dr. Maryam Najafi for their technical support, and also Miss Ozra Zarghi, the health worker of Soozandeh village, as well as the patients and their families for their contribution. The authors declare no conflict of interest in this study.

Authors' Contributions

E.Sh., Z.B.; Designed and supervised the study. E.Sh.; Funded the study, recruited the patients, and did the ocular examination. F.P., H.N.; Performed the molecular analysis, the bioinformatics analysis, and drafted the manuscript, which was revised by Z.B. All authors read and approved the final manuscript.

References

1. Messina-Baas O, Cuevas-Covarrubias SA. Inherited congenital cataract: a guide to suspect the genetic etiology in the cataract genesis. Mol Syndromol. 2017; 8(2): 58-78.
2. Shiels A, Hejtmancik JF. Genetic origins of cataract. Arch Ophthalmol. 2007; 125(2): 165-173.
3. Hejtmancik JF, Smaoui N. Molecular genetics of cataract. Dev Ophthalmol. 2003; 37: 67-82.
4. Shiels A, Hejtmancik JF. Molecular genetics of cataract. Prog Mol Biol Transl Sci. 2015; 134: 203-218.
5. Rajavi Z, Sabbaghi H. Congenital cataract screening. J Ophthalmic Vis Res. 2016; 11(3): 310-312.
6. Vanita V, Singh D, Robinson PN, Sperling K, Singh JR. A novel mutation in the DNA-binding domain of MAF at 16q23. 1 associated with autosomal dominant "cerulean cataract" in an Indian family. Am J Med Genet A. 2006; 140(6): 558-566.
7. Gilbert C, Foster A. Childhood blindness in the context of VISION 2020--the right to sight. Bull World Health Organ. 2001; 79(3): 227-232.
8. Sheeladevi S, Lawrenson JG, Fielder AR, Suttle CM. Global prevalence of childhood cataract: a systematic review. Eye (Lond). 2016; 30(9): 1160-1169.
9. Haargaard B, Wohlfahrt J, Fledelius HC, Rosenberg T, Melbye M. Incidence and cumulative risk of childhood cataract in a cohort of 2.6 million Danish children. Invest Ophthalmol Vis Sci. 2004; 45(5): 1316-1320.
10. Marner E, Rosenberg T, Eiberg H. Autosomal dominant congenital cataract. Morphology and genetic mapping. Acta Ophthalmol (Copenh). 1989; 67(2): 151-158.
11. Shiels A, Hejtmancik JF. Genetics of human cataract. Clin Genet. 2013; 84(2): 120-127.
12. Conley YP, Erturk D, Keverline A, Mah TS, Keravala A, Barnes LR, et al. A juvenile-onset, progressive cataract locus on chromosome 3q21-q22 is associated with a missense mutation in the beaded filament structural protein–2. Am J Hum Genet. 2000; 66(4): 1426-1431.
13. Iqbal H, Khan SY, Zhou L, Irum B, Ali M, Ahmed MR, et al. Mutations in FYCO1 identified in families with congenital cataracts. Mol Vis. 2020; 26: 334-344.
14. Haargaard B, Wohlfahrt J, Rosenberg T, Fledelius HC, Melbye M. Risk factors for idiopathic congenital/infantile cataract. Invest Ophthalmol Vis Sci. 2005; 46(9): 3067-3073.
15. Foster A, Gilbert C, Rahi J. Epidemiology of cataract in childhood: a global perspective. J Cataract Refract Surg. 1997; 23 Suppl 1: 601-604.
16. Schwarz JM, Cooper DN, Schuelke M, Seelow D. MutationTaster2: mutation prediction for the deep-sequencing age. Nat Methods. 2014; 11(4): 361-362.
17. Kouza M, Faraggi E, Kolinski A, Kloczkowski A. The GOR method of protein secondary structure prediction and its application as a protein aggregation prediction tool. Methods Mol Biol. 2017; 1484: 7-24.
18. Chen J, Ma Z, Jiao X, Fariss R, Kantorow WL, Kantorow M, et al. Mutations in FYCO1 cause autosomal-recessive congenital cataracts. Am J Hum Genet. 2011; 88(6): 827-838.
19. Raiborg C, Wenzel EM, Pedersen NM, Olsvik H, Schink KO, Schultz SW, et al. Repeated ER-endosome contacts promote endosome translocation and neurite outgrowth. Nature. 2015; 520(7546): 234-238.
20. Kiss H, Yang Y, Kiss C, Andersson K, Klein G, Imreh S, et al. The transcriptional map of the common eliminated region 1 (C3CER1) in 3p21.3. Eur J Hum Genet. 2002; 10(1): 52-61.
21. Olsvik HL, Lamark T, Takagi K, Larsen KB, Evjen G, Overvatn A, et al. FYCO1 contains a c-terminally extended, LC3A/B-preferring LC3-interacting region (LIR) motif required for efficient maturation of autophagosomes during basal autophagy. J Biol Chem. 2015; 290(49): 29361-29374.
22. Pras E, Pras E, Bakhan T, Levy-Nissenbaum E, Lahat H, Assia EI, et al. A gene causing autosomal recessive cataract maps to the short arm of chromosome 3. Isr Med Assoc J. 2001; 3(8): 559-562.
23. Chen J, Wang Q, Cabrera PE, Zhong Z, Sun W, Jiao X, et al. Molecular genetic analysis of Pakistani families with autosomal recessive congenital cataracts by homozygosity screening. Invest Ophthalmol Vis Sci. 2017; 58(4): 2207-2217.
24. Li J, Leng Y, Han S, Yan L, Lu C, Luo Y, et al. Clinical and genetic characteristics of Chinese patients with familial or sporadic pediatric cataract. Orphanet J Rare Dis. 2018; 13(1): 94.
25. Özkan EG. Genetics of inherited eye diseases in the Iranian population. Presented for the Ph.D., London. St George's, University of London. 2016.
26. Khan AO, Aldahmesh MA, Alkuraya FS. Phenotypes of recessive pediatric cataract in a cohort of children with identified homozygous gene mutations (An American Ophthalmological Society Thesis). Trans Am Ophthalmol Soc. 2015; 113: T7.
27. Li J, Leng Y, Han S, Yan L, Lu C, Luo Y, et al. Clinical and genetic characteristics of Chinese patients with familial or sporadic pediatric cataract. Orphanet J Rare Dis. 2018; 13(1): 94.
28. Patel N, Anand D, Monies D, Maddirevula S, Khan AO, Algoufi T, et al. Novel phenotypes and loci identified through clinical genomics approaches to pediatric cataract. Hum Genet. 2017; 136(2): 205-225.
29. Aldahmesh MA, Khan AO, Mohamed JY, Hijazi H, Al-Owain M, Alswaid A, et al. Genomic analysis of pediatric cataract in Saudi Arabia reveals novel candidate disease genes. Genet Med. 2012; 14(12): 955-962.
30. Gillespie RL, O'Sullivan J, Ashworth J, Bhaskar S, Williams S, Biswas S, et al. Personalized diagnosis and management of congenital cataract by next-generation sequencing. Ophthalmology. 2014; 121(11): 2124-2137.

Short Communication

A *Haspin* Promoter Element Induces Tissue-Specific Methylation of A Transcription Region, and Gene Expression in Superovulated Mouse Ova

Hiromitsu Tanaka, Ph.D.[1]*, Keizo Tokuhiro, Ph.D.[2]

1. Labaratory of Molecular Biology, Faculty of Pharmaceutical Sciences, Nagasaki International University, 2825-7 Huis Ten Bosch, Sasebo, Nagasaki, Japan
2. Department of Genome Editing, Institute of Biomedical Science, Kansai Medical University, Shin-machi, Hirakata City, Osaka, Japan

Corresponding Address: Labaratory of Molecular Biology, Faculty of Pharmaceutical Sciences, Nagasaki International University, Huis Ten Bosch, Sasebo, Nagasaki, Japan
Email: h-tanaka@niu.ac.jp

Received: 28/January/2022, Accepted: 18/April/2022

Abstract

HASPIN is a nuclear serine-threonine kinase originally identified in the mouse testis. Its 193 bp DNA promoter element (hereafter, 193PE) regulates bidirectional, synchronous gene expression in the germ cells of male mice. Recent studies have shown that *Haspin* is also expressed in trace amounts in somatic cells; HASPIN also functions in oocytes. *Haspin* expression is regulated by the tissue-specific methylation of *Haspin* genomic DNA regions, including somatic cells. This study investigated relationship between 193PE and DNA methylation by examining methylation status of transgenic mice carrying 193PE and a reporter gene. In somatic (liver) cells carrying the reporter gene, 193PE induced methylation as well as trace expression of the reporter gene. In the testis, 193PE induced hypomethylation and intense reporter gene expression. Expression of HASPIN in an egg was assessed using human chorionic gonadotrophin to induce ovulation in female transgenic mice. The results showed that 193PE induced tissue-specific methylation, which resulted in reporter gene expression in a mouse egg.

Keywords: Embryo, Haspin, Inner Cell Mass, Germ Cell, Oocyte

Cell Journal(Yakhteh), Vol 24, No 9, September 2022, Pages: 552-554

Citation: Tanaka H, Tokuhiro K. A Haspin promoter element induces tissue-specific methylation of a transcription region, and gene expression in superovulated mouse ova. Cell J. 2022; 24(9): 552-554. doi: 10.22074/cellj.2022.8444.

HASPIN is a nuclear serein/thyrosin (Ser/Thr) kinase, expression of which was originally identified in haploid germ cells (1). While intensely expressed in the testis, trace amounts have been detected in the other tissues (2). Because *Haspin* is conserved in many organisms, including plants and yeast, it is considered fundamental for cell survival (3, 4). Recently, in normal cells *in vivo*, its role in mitosis is functionally complemented by the other molecules, as no abnormality is observed in *Haspin*-disrupted mice (5). It was also reported that HASPIN played an important role in the growth of cancer cells, due to the blockage of HASPIN effect by the corresponding inhibitors (6-8). Analysis of HASPIN expression *in vivo* is an important because HASPIN phosphorylated histone H3 at threonine 3 during chromosomal partitioning and was a target for tumor suppression. The mechanism of *Haspin* gene expression has previously been reported. Transgenic mice were generated with a DNA fragment linking the element located in193 bp upstream from the transcription start site to EGFP and Ds-Red, as a reporter gene. The reporter assay in mice showed that element located in the 193 bp DNA fragment regulated *Haspin* expression in the testis (9). A tissue-differentially methylated region (T-DMR) was also identified, located 600 bp upstream (from –641 to –517) of the transcriptional start site of *Haspin* (10). The T-DMR of *Haspin* was hypomethylated in male germ cells, but hypermethylated in somatic tissues. These observations indicated that the 193 bp DNA promoter element (193PE) induced tissue-specific *Haspin* expression, mediated by the tissue-specific methylation of the genomic region around *Haspin*. Here we showed that 193PE induced methylation of a reporter gene in the genomic DNA of somatic cells and testis hypomethylation, mimicking specific expression in male germ cells. It has also been shown to induce reporter gene expression in the egg and blastocyst inner cell mass.

A pBiPRO2 reporter gene previously constructed in our lab was used to investigate methylation status of transgenes located in genomic DNA in the liver and testis of mice (Fig.1) (9). The transgenic mice were bred under specific-pathogen-free conditions in the animal room at Nagasaki International University (Japan). The animals were euthanized by cervical dislocation just before the experiments. All animal experiments conformed to the Guide for the Care and Use of Laboratory Animals and they were approved by the Institutional Committee of Laboratory Animal Experimentation and Ethics of Nagasaki International University (128). Genomic DNA isolated from the testis and liver was purified by phenol extraction (1) and its methylation status was determined by bisulfite genomic sequencing (CHEMICON International, USA). Figure 2 shows the results of bisulfite genomic sequencing. It has been reported that the region around the endogenous Haspin genomic region is differentially

methylated in tissues and the endogenous *Haspin* genomic region including T-DMR was hypomethylated in the testis (Upper bar in Fig.2) (10). The pBiPRO2 transgene was hypermethylated in the liver and hypomethylated in testis (lower part of Fig.2). These results indicated tissue-specific methylation of the genomic *Haspin* gene locus by the 193PE *Haspin* promoter element.

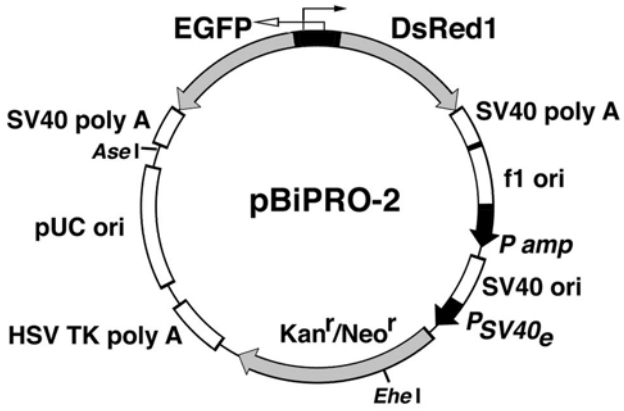

Fig.1: Construction of the reporter plasmid BiPRO-2 for transgenic mice. The 193 bp DNA promoter element (193PE) was inserted into the *EGFP* and *DsRed* reporter genes. Arrows indicate directions of *Haspin* (white arrow), and mADE (black arrow) is a non-coding mRNA transcript (11, 12). The *Ase*I-*Nhe*I DNA fragments containing the reporter genes were used as transgenes.

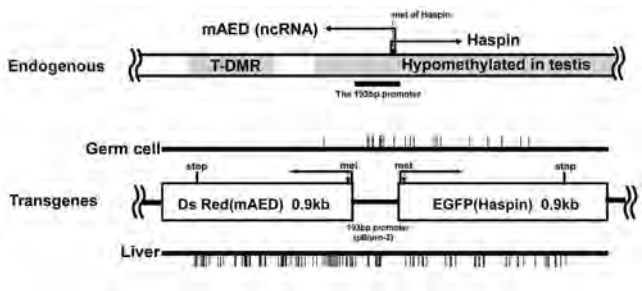

Fig.2: Schematic presentation of the methylation status on the locus of endogenous *Haspin* and transgenes region of the reporter genes. The top box shows genomic region of endogenous *Haspin* and differentially methylated region (shading) (10). The bottom box shows transgene region of the reporter gene in the genome. The bars indicate methylation status on the reporter genes in the testis and liver. The vertical bars represent location of methylated CpG. Region around the endogenous *Haspin* genomic region was differentially methylated between tissues, consistent with the activity of 193PE. Arrows indicated transcription of each gene and 'met' and 'stop' are the translation initiation and stop codons, respectively. mADE is a non-coding mRNA (12).

Because HASPIN has also been reported to function in meiosis in mouse oocytes (13), we investigated whether 193PE also regulated its expression. Oocytes, arrested in the first meiotic prophase of female transgenic mice, were grown with gonadotropins and expression of the reporter gene in the ovaries was observed. Expression of the reporter gene EGPF was examined by Western blotting of mouse ovarian tissues from transgenic mice with ovarian hyperstimulation and non-hyperstimulation; detection was achieved using anti-GFP monoclonal antibody as described previously (9). Briefly, superovulation was induced in transgenic female mice by an intraperitoneal injection of 5 IU of pregnant mare serum gonadotropin, followed 46-48 hours later by 5 IU of human chorionic gonadotropin. The mice were euthanized 14-16 hours later and their ovaries were collected. Gene expression was analyzed by Western blotting after sonicating the tissues in TBS-T (100 mmol/L Tris-HCl [pH=7.5], 150 mmol/L NaCl and 0.1 w/v% Tween 20) buffer. An EGFP signal, and thus gene expression in response to 193PE activity, was observed only in the hyperstimulated ovaries (Fig.3), but not detected in ovaries without hyperstimulation (11). These results suggested that expression of the gene from 193PE was induced when oocyte division arrest was released with hyperstimulation.

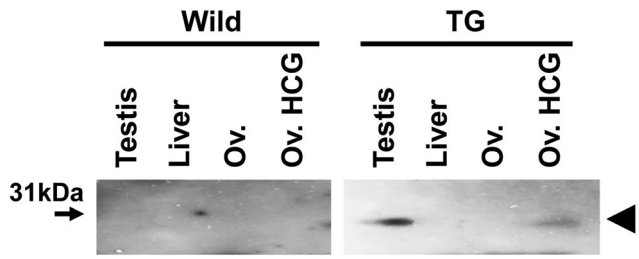

Fig.3: Analysis of EGFP reporter gene expression in the ovaries. EGPF expression was examined by Western blotting of mouse ovaries from transgenic mice with ovarian hyperstimulation and non-hyperstimulation. Signal detection was achieved using anti-EGFP monoclonal antibody. Ov and Ov HCG indicate non-hyperstimulated or hyperstimulated ovaries. The arrow indicates Mr 31k. The arrowhead indicates the position of the EGFP signals.

Next, cumulus-oocyte complexes collected from the ampullae of the uterine tubes were fertilized *in vitro* with wild type sperm in HTF medium. After 24 hours, the embryos were cultured in potassium simplex optimization medium (KSOM) and *Haspin* expression over the time was assessed by fluorescence microscope (Fig.4). In these post-ovulatory oocytes, 193PE induced expression of reporter genes and participated in post-fertilization embryonic development, although it was unclear whether the results were attributable to ovulation or to transcribed maternal mRNA. EGFP was expressed in morula cells, but thereafter a signal was observed only in the inner cell mass (ICM), not in trophectoderm cells. Although transcription and translation were maintained in the oocytes for several days during embryogenesis (14), these observations suggested that *Haspin* gene expression was specifically maintained in ICM of the blastocyst. HASPIN may be expressed and play a role in proliferating cells. Reason of no expression of HASPIN in trophoblasts is unclear, but it is linked to the epigenetic

changes and expression during the process of trophoblast and ICM differentiation.

In summary, 193PE from genomic *Haspin* induced tissue-specific methylation and specific gene expression in the surrounding genomic DNA region. In isolated mouse eggs, 193PE induced specific expression in the ICM of the blastocyst, confirming a role for this very small DNA fragment in tissue-specific methylation and gene expression in cells, other than germ cells of the testis. Further studies of the role of HASPIN and mechanism of tissue-specific methylation are needed. Use of transgenic mice carrying the EGFP reporter gene will aid in these investigations (15).

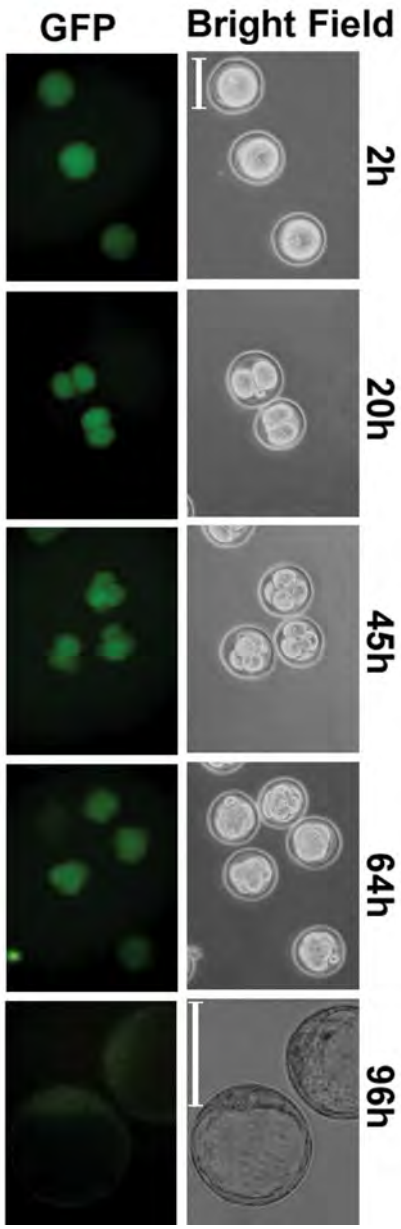

Fig.4: Fluorescence microscope images of the fertilized eggs of transgenic mice. The images were obtained at different times after *in vitro* insemination of the eggs. Green color indicates the EGFP expression. 2, 20, 45, 64 and 96 hours indicate time of the culture after insemination (scale bar: 100 mm).

Acknowledgements

None of the authors have competing financial interests to declare. There was no financial support for this study.

Authors' Contributions

H.T.; Contributed to the conception and design, experimental work, data and statistical analysis, data interpretation, and wrote the manuscript. K.T.; Contributed to experimental work, data analysis. Both authors read and approved the final version of the manuscript.

References

1. Tanaka H, Yoshimura Y, Nozaki M, Yomogida K, Tsuchida J, Tosaka Y, et al. Identification and characterization of a haploid germ cell-specific nuclear protein kinase (Haspin) in spermatid nuclei and its effects on somatic cells. J Biol Chem. 1999; 274(24): 17049-17057.
2. Dai J, Sultan S, Taylor SS, Higgins JM. The kinase haspin is required for mitotic histone H3 Thr 3 phosphorylation and normal metaphase chromosome alignment. Genes Dev. 2005; 19(4): 472-488.
3. Higgins JM. Haspin-like proteins: a new family of evolutionarily conserved putative eukaryotic protein kinases. Protein Sci. 2001; 10(8): 167716-167784.
4. Kurihara D, Matsunaga S, Omura T, Higashiyama T, Fukui K. Identification and characterization of plant Haspin kinase as a histone H3 threonine kinase. BMC Plant Biol. 2011; 11: 73.
5. Shimada M, Goshima T, Matsuo H, Johmura Y, Haruta M, Murata K, et al. Essential role of autoactivation circuitry on Aurora B-mediated H2AX-pS121 in mitosis. Nat Commun. 2016; 7: 12059.
6. Huertas D, Soler M, Moreto J, Villanueva A, Martinez A, Vidal A, et al. Antitumor activity of a small-molecule inhibitor of the histone kinase Haspin. Oncogene. 2012; 31(11): 1408-1418.
7. Tanaka H, Wada M, Park J HASPIN kinase inhibitor CHR-6494 suppresses intestinal polyp development, cachexia, and hypogonadism in Apcmin/+ mice. Eur J Cancer Prev. 2020; 29(6): 481-485.
8. Elie J, Feizbakhsh O, Desban N, Josselin B, Baratte B, Bescond A, et al. Design of new disubstituted imidazo[1,2-b]pyridazine derivatives as selective Haspin inhibitors. Synthesis, binding mode and anticancer biological evaluation. J Enzyme Inhib Med Chem. 2020; 35(1): 1840-1853.
9. Tokuhiro K, Miyagawa Y, Yamada S, Hirose M, Ohta H, Nishimune Y, et al. The 193-base pair Gsg2 (haspin) promoter region regulates germ cell-specific expression bidirectionally and synchronously. Biol Reprod. 2007; 76(3): 407-414.
10. Sato S, Maeda C, Hattori N, Yagi S, Tanaka S, Shiota K. DNA methylation-dependent modulator of Gsg2/Haspin gene expression. J Reprod Dev. 2011; 57(4): 526-533.
11. Higgins JM. Structure, function and evolution of haspin and haspin-related proteins, a distinctive group of eukaryotic protein kinases. Cell Mol Life Sci. 2003; 60(3): 446-462.
12. Higgins JM. The Haspin gene: location in an intron of the integrin alphaE gene, associated transcription of an integrin alphaE-derived RNA and expression in diploid as well as haploid cells. Gene. 2001; 267(1): 55-69.
13. Nguyen AL, Gentilello AS, Balboula AZ, Shrivastava V, Ohring J, Schindler K. Phosphorylation of threonine 3 on histone H3 by haspin kinase is required for meiosis I in mouse oocytes. J Cell Sci. 2014; 127(23): 5066-5078.
14. Winata CL, Korzh V. The translational regulation of maternal mRNAs in time and space. FEBS Lett. 2018; 592(17): 3007-3023.
15. Gohbara A, Katagiri K, Sato T, Kubota Y, Kagechika H, Araki Y, et al. In vitro murine spermatogenesis in an organ culture system. Biol Reprod. 2010; 83(2): 261-267.